ERIKA RAJACKAITĖ

MICROWAVE PLASMA-ENHANCED CHEMICAL VAPOUR DEPOSITION AND QUALITY STUDIES OF PLANAR AND VERTICAL GRAPHENE LAYERS

DOCTORAL DISSERTATION

Kaunas
2022

KAUNAS UNIVERSITY OF TECHNOLOGY

ERIKA RAJACKAITĖ

MICROWAVE PLASMA-ENHANCED CHEMICAL VAPOUR DEPOSITION AND QUALITY STUDIES OF PLANAR AND VERTICAL GRAPHENE LAYERS

Doctoral dissertation
Technological Sciences, Materials Engineering (T 008)

2022, Kaunas

This doctoral dissertation was prepared at Kaunas University of Technology, Institute of Materials Science during the period of 2016–2021. The studies were supported by the Research Council of Lithuania.

Scientific Supervisor

Prof. habil. Dr. Sigitas TAMULEVIČIUS (Kaunas University of Technology, Technological Sciences, Materials Engineering – T 008).

Doctoral dissertation has been published in:
http://ktu.edu

Editor:

Dr. Armandas Rumšas (Publishing House *Technologija*)

KAUNOTECHNOLOGIJOS UNIVERSITETAS

ERIKA RAJACKAITĖ

PLANARINIO IR VERTIKALAUS GRAFENO SLUOKSNIŲ MIKROBANGE PLAZMA AKTYVINAMAS CHEMINIS NUSODINIMAS IŠ GARŲ FAZĖS BEI KOKYBĖS TYRIMAI

Daktaro disertacija
Technologijos mokslai, medžiagų inžinerija (T 008)

2022, Kaunas

Disertacija rengta 2016–2021 metais Kauno technologijos universiteto Medžiagų mokslo institute. Mokslinius tyrimus rėmė Lietuvos mokslo taryba.

Mokslinis vadovas:

Prof. habil. dr. Sigitas TAMULEVIČIUS (Kauno technologijos universitetas, technologijos mokslai, medžiagų inžinerija – T 008).

Interneto svetainės, kurioje skelbiama disertacija, adresas:
http://ktu.edu

Redagavo:

Dr. Armandas Rumšas (leidykla „Technologija“)

TABLE OF CONTENTS

LIST OF FIGURES

LIST OF TABLES

LIST OF ABBREVIATIONS AND SYMBOLS

2D, 3D – two-, three-dimensional
A – absorbance, area
a – lattice parameter
AFM – atomic force microscope
B – magnetic field
Bphene – 4,7-diphenyl-1,10-phenanthroline
CB – conduction band
CB – valence band
CCD – charge-coupled device
CVC – current-voltage characteristics
CVD – chemical vapour deposition
DC – direct current
E – electric field
EC – electrochromic
ETL – electron transport layer
FE – field emission
FF – fill factor
fs-laser – femtosecond laser
FTMC – Centre for Physical Sciences and Technology
FWHM – full width at half maximum
I – current, intensity
ITIC – 3,9-bis(2-methylene-(3-(1,1-dicyanomethylene)-indanone))-5,5,11,11-tetrakis(4-hexylphenyl)-dithieno[2,3-d:2’,3’-d’]-s-indaceno[1,2-b:5,6-b’]dithiophene
ITO – Indium tin oxide
I-V – current-voltage
J_{SC} – open circuit voltage
J_{SC} – short circuit current density
J-V – current density-voltage
k – Boltzmann constant
K – Dirac point
L – channel length, thickness of the electrolyte
L_a – average crystallite size
L_D – average distance between nearest defects
L_T – transfer length beneath the contact
MR – magnetoresistance
MW PECVD – microwave plasma-enhanced chemical vapor deposition
N – number of cycles
n_D – defect density
NG – nanographitic
NIR – near infrared
NMR – negative magnetoresistance
OSC – organic solar cells
P – power

p – pressure
PB – Prussian Blue
PCE – power conversion efficiency
PCE12 – poly[(2,6-(4,8-bis(5-(2-ethylhexyl)thiophen-2-yl)-benzo[1,2-b:4,5-b']dithiophene))-alt-(5,5-(1',3'-di-2-thienyl-5',7'-bis(2-ethylhexyl)benzo[1',2'-c:4',5'-c']dithiophene-4,8-dione)]
PET – poly(ethylene terephthalate)
PMMA – poly(methyl methacrylate)
PMR – positive magnetoresistance
Pos – position
R – electrical resistance
R_a – arithmetic average roughness
R_C – contact resistance
R_q – root mean square roughness
R_S – sheet resistance
R_T – total resistance
SEM – scanning electron microscopy
T – temperature, transmittance
t – time
TAS – transient absorption spectroscopy
TE – transverse electric
TLM – transmission line model
TM – transverse magnetic
U – voltage
UV – ultraviolet
V – voltage
VB – valence band
VGN – vertical graphene nanosheet(s)
Vis – visible
W – contact width
XPS – X-ray photoelectron spectroscopy
XRD – X-ray diffraction
λ – wavelength
λ_L – excitation laser wavelength
ρ – density
σ – defect density
τ – delay time

I. INTRODUCTION

Worldwide research on graphene has been implemented for seventeen years with significant breakthroughs, and it is still being continued aiming for commercialisation at industrial scales [1–9]. At the moment, various routes of the production and synthesis of graphene, such as epitaxial deposition, mechanical exfoliation, reducing graphene oxide, chemical vapour deposition (CVD), etc. [10–14] are available with varying levels of success. The modification of CVD – microwave plasma-enhanced chemical vapour deposition (MW PECVD) that can be performed at relatively low temperatures – has been proven as an efficient method for the formation of planar and vertical graphene on catalytic and non-catalytic substrates having a range of morphology features and possessing diverse properties [15–20]. A lot of research is being devoted to direct graphene synthesis on widely applicable SiO_2, fused silica, Al_2O_3, and other dielectric substrates in order to avoid a transfer process of these layers by passing the possible mechanical damage as well as chemical contamination. On the other hand, the control of graphene growth on these substrates as well as the analysis of this kind of graphene defects is a fairly complicated task so far. Therefore, the development of graphene applications is a relatively slow process, and, probably, the main cause for this is the sub-optimal, and, actually, rather poor quality of the graphene produced by many companies in the world, which is a fact that is impossible to challenge [11]. As a consequence, large-area graphene films with high crystallinity, a large grain size, and high conductivity are still an aspiration. Therefore, it is very important to evolve and improve tools and methods for graphene quality exploration concerning the presence of defects and disorder.

The vertical graphene nanosheets (VGN) film is one of the popular 3D carbon structure materials possessing a large specific surface area, rich exposed sharp edges, non-stacking geometry, and good out-of-plane conductivity [21–23]. Despite intensive studies in this field, the detailed growth mechanisms of VGN are not fully understood and therefore need further insights [24]. It is assumed that fractional carbon-containing species and radicals generated in hydrocarbon plasma act as building blocks for the VGN growth, but the role of plasma in the vertical alignment of the sheets is still unknown [25,26]. Therefore, systematic studies of VGN formation starting from their nucleation to overgrowth into more complex carbon nanostructures, including their respective differences in structure and properties, the formation of the interfaces, as well as the kinetics of VGN growth are necessary for the further application of this carbonaceous nanomaterial [27,28] [A1].

Undoubtedly, it is also very important to develop and improve tools and methods for graphene quality analysis, or, in other words, the quality investigation that would lead to the creation of new synthesis standards. The insufficiency of standards has probably been stopping the development of graphene applications due to the unclear quality of the material on the market [11,29]. Currently, one of the most effective instruments to analyse the quality of graphene is the Raman scattering spectroscopy. It is non-destructive, fast, of high resolution, and, so far, yields a lot of structural and electronic information about graphene layers [30,31]. However, it

does not provide full structural information in the case of vertical graphene due to the intricacy of these layers.

As the detailed analysis of defects is such a relevant topic in graphene research, it is no wonder that additional methods of the study of defects are of interest to the scientific community. One of the perspective techniques that can be used for the analysis of defects is the transient absorption spectroscopy (TAS). TAS is a well-known technique that has been intensively used to investigate relaxation processes in various carbon-based materials: nanodiamonds, diamond-like carbon [32,33], graphite [34], multi-layer and single-layer graphene [35]. Also, there are reports on TAS microscopy that were used to study graphene defects associated with the grain boundaries, providing the accuracy comparable to the Raman scattering spectroscopy, but offering a much faster measuring time [36]. TAS gives information about hot electron relaxation dynamics; therefore, it provides data about the time-resolved process that the Raman scattering spectroscopy lacks [36]. It could lead to additional information about graphene layers that cannot be received by other methods [A2]. Moreover, the understanding of the ultrafast charge carrier dynamics of graphene is an important issue in optical and high-speed electronic applications [37]. In general, that might prompt the development of other various graphene applications.

Research objective

To synthesise planar and vertical graphene layers by the microwave plasma-enhanced chemical vapour deposition method, to explore the quality of these layers by using various analytical methods, and to apply them as flexible electrodes in organic devices.

Research tasks

1. To experimentally select the synthesis parameters as well as the mounting setup of a sample, and to deposit planar graphene and vertical graphene nanosheet layers on catalyst and catalyst free dielectric substrates employing the microwave plasma-enhanced chemical vapour deposition technique.
2. To investigate the morphological, structural, electrical, as well as optical, electro-optical properties of the formed graphene films and to examine the effects of the various deposition conditions.
3. To develop defect/quality studies of graphene layers focusing on the advanced transient absorption spectroscopy method in comparison with the conventional Raman scattering spectroscopy.
4. To apply planar graphene layers as transparent flexible electrodes in organic devices involving the graphene transfer process.

Scientific novelty

1. Ultrafast charge carrier dynamics of excited state relaxation of planar graphene and vertical graphene nanosheet films were investigated at the

atomic level in terms of defects employing transient absorption spectroscopy.
2. Correlation between the Raman scattering spectroscopy and the transient absorption spectroscopy obtained data analysing the quality of graphene layers was specified.
3. Planar graphene films were integrated into organic devices as transparent flexible electrodes including the graphene transfer process without using any additional support top-layers or plasma etching.

Key statements

1. The wet-chemical graphene transfer process can be optimised and accomplished successfully without using any additional supporting materials.
2. Adapted transient absorption spectroscopy can complement Raman scattering spectroscopy data and be a perspective tool for the quality/defect analysis of graphene layers.
3. Synthesised graphene layers have a high potential to be applied as flexible transparent electrodes.

Author's contribution

The experiments were planned, evaluated and prepared for the realisation under the guidance of scientific supervisor Prof. dr. habil. Sigitas Tamulevičius.

The author actively took part in microwave plasma-enhanced chemical vapour deposition experiments of planar graphene and vertically standing graphene nanosheets on catalyst and catalyst free dielectric substrates, systematic selection of synthesis process parameters under the direction of dr. Rimantas Gudaitis. E. Rajackaitė worked on the planar graphene transfer process from copper foil to a target substrate or a structure using different variations, while preserving a large undisrupted area of layers. It is a fundamental step for graphene applications in organic devices whose components cannot withstand high temperatures. The author performed atomic force microscopy, Raman scattering, UV-VIS spectroscopy, electric transmission line model measurements, obtained data processing, conducted the analysis of results and performed graphical visualisation. The author participated in transient absorption spectroscopy measurements performed by dr. Domantas Peckus and analysed the results of studies, and also performed analysis of the results of SEM and XPS measurements.

E. Rajackaitė was involved in the formation of organic solar cells using the full production cycle (graphene electrode preparation, spin-coating of electron transport and active layers, chemical vapour deposition of the hole transport layer and the metal electrode) during a three-month traineeship at MCI SDU and in preparing them for the device performance characterisation. Furthermore, she took part in the Project PP/174 *Bipolar Organic Materials for Flexible Electrochromic Devices* led by dr. A. Tamulevičienė at KTU, where she mostly worked on the graphene transfer for flexible electrode formation.

The scientific and technical team of KTU, SDU and Belarusian State University greatly contributed to the entire research process with training, implementation of specific technological processes, analytical measurements, discussions and interpretation of the obtained data.

II. LITERATURE REVIEW

2.1. Graphene properties

2.1.1. Planar graphene

Graphene is a two-dimensional (2D) system consisting of strong covalent sp^2-bonded carbon hexagonal networks [38]. The unit cell for single-layer or monolayer graphene (1-LG) consists of two carbon atoms (A and B), each forming a trident 2D network, but remoted from each other by a distance of 0.142 nm (**Figure 1 a**) [39]. Multilayer graphene (MLG) can be stacked layer by layer in a Bernal (AB) (**Figure 1 b**) or rhombohedral (ABC) arrangement way through van der Waals interaction [40]. The interlayer spacing is reported with values of 0.34–0.37 nm and graphene monolayer thickness of 0.335–0.345 nm [40,41]. In 2-LG with AB stacking, the unit cell contains four carbon atoms (A_1, A_2, B_1, and B_2) on the two-layer planes depicted in **Figure 1 b**. There is no stacking order between neighbouring graphene layers in turbostratic graphite, and the interlayer spacing (> 0.342 nm) is larger than that for crystalline graphite. Generally, the 2-LG films formed from the mechanical exfoliation of graphite demonstrate an AB stacking, while chemical vapour deposited graphene does not maintain this ordered AB stacking, and, therefore, the corresponding electronic coupling between different layers does not occur in all areas of the film [31]. The diminished interlayer interaction can be advantageous for some applications as MLG with weak interlayer coupling exhibits electronic properties more similar to those of a single-layer graphene.

The unit cell in a reciprocal space is shown in **Figure 1 c** for 1-LG, where some high symmetry points within the first Brillouin zone are given: the Γ point at the zone centre, the inequivalent K and K' points at the corners, and the M points in the middle of the sides of the hexagons [42].

Graphene possesses a linear electronic band dispersion (**Figure 1 c**), which leads to its high mobility and unique optical properties [43]. **Figure 1 e**–**h** displays the band structure of 1-LG, 2-LG, 3-LG, and 4-LG. The band structures from single to 4-layered graphene (AB-stacked) differ due to the van der Waals interlayer interactions and changes in symmetry [44]. The band structure of N-layered graphene alters the 2D mode profile of the respective Raman scattering spectra by double resonant Raman scattering. Thus, Raman spectroscopy can be utilised to probe the band structure and to determine the number of layers of graphene consisting of up to 3 layers [31,45].

The comprehension of the phonon dispersion of graphene is fundamental in our pursuit to explain the Raman scattering and TAS spectra of graphene. Whereas the unit cell of 1-LG consists of two carbon atoms, there are six phonon modes (lattice vibrations) (**Figure 2**): LO, iTO, oTO, LA, iTA, and oTA (where O – optic, A – acoustic, o – out-of-plane, i – in-plane, L – longitudinal, T – transverse) [31,46].

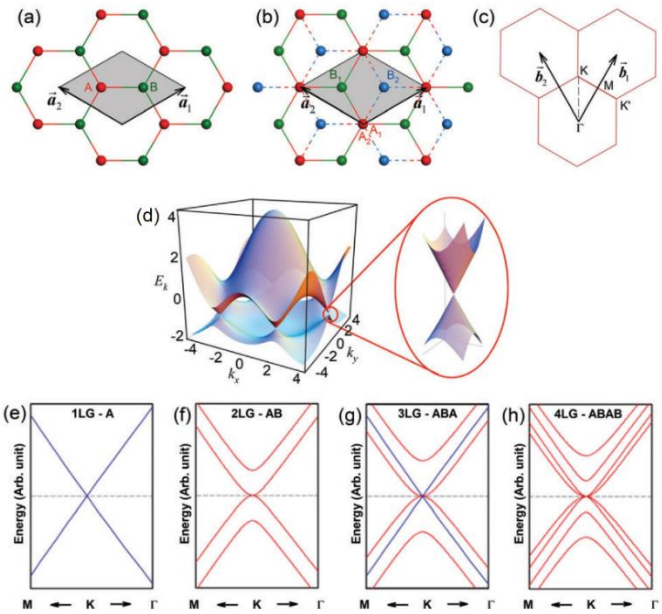

Figure 1. Unit cell of 1LG: inequivalent atoms A and B, unit vectors $\vec{a}_1$ and $\vec{a}_2$ (**a**); AB-stacked 2LG (**b**). The unit cell of 1LG in the reciprocal space – the first Brillouin zone with its primitive vectors, high symmetry points and axes: *M*, *Γ*, *K*, *K′* (**c**). Band structure of 1LG (**d**) [47]. Band structures of 1LG (**e**), AB-stacked 2LG (**f**), 3LG (**g**), and 4LG (**h**) in the vicinity of K point near Fermi level [48]

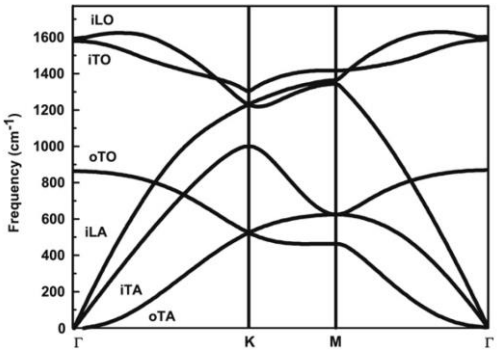

Figure 2. Phonon dispersion in graphene displaying the iLO, iTO, oTO, iLA, iTA and oTA phonon branches [49]

A number of unique properties are demonstrated by this material. Graphene is a gapless semi-metal material, therefore, charge carrier generation by light absorption over a very wide energy spectrum is possible. It is unmatched by any other material [1]. Other interesting properties of graphene are ultrafast carrier dynamics, wavelength-independent absorption, tuneable optical properties via electrostatic doping, low dissipation rates, high charge carrier mobility and the ability to confine electromagnetic energy to unprecedented small volumes [50] [A2].

2.1.2. Vertical graphene

Vertical graphene nanosheet (VGN) films are much more complex layers compared to planar graphene because they consist of a nanographitic (NG) base layer and vertically free-standing few-layered graphene nanoflakes grown on top which form a percolated network [51–54]. Some researchers also name this material as vertically stacked graphene networks, carbon nanowalls, edge-oriented graphene, free-standing subnanometer graphite sheets arrays, etc. VGN possess plenty of sharp, exposed, and vertically oriented edges where top atoms have special chemical reactivity providing sites to adsorb functional materials and dopants. The height of the sheets can range from a couple hundred of nanometers to several dozen of microns, but the average thickness of the sheets reaches a few nanometers. The shape can be straight or curved in various ways [41].

VGN have many unique properties, and fundamental ones inherent to graphene materials, such as the large specific surface area, chemically active exposed edges and defects, the highest ratio of edge atoms of any carbon derivative, as well as high electrical and thermal conductivity, and chemical stability [54,55]. What is more, graphene nanosheets serve as a path for the electric charges travelling from the top to the bottom.

All the above mentioned features make VGN an effective electric charge transferring and mechanical supporting structure.

2.2. Formation of planar and vertical graphene layers

There are a number of methods for the preparation of planar graphene and VGN including the surfactant-assisted pure shear milling method [56], the decomposition of ethanol in a dual-channel microwave plasma torch at atmospheric pressure [57], heating glucose and/or urea thin layers in a furnace [58], thermal graphitisation of SiC by silicon sublimation [59], mechanical exfoliation of graphite [31,60], reducing graphene oxide [61], epitaxial deposition [62], and chemical vapour deposition [63–68]. One of the variations of CVD – microwave plasma-enhanced chemical vapour deposition (MW PECVD) that can be carried out at relatively low temperatures – is an efficient method for the deposition of planar and VGN denoted by a wide range of morphology, structure features and possessing multifarious properties [15,69,70] [A1]. Due to the presence of energetic electrons, photons, free radicals, photons, and other active species in the plasma, MW PECVD provides the advantages of higher growth selectivity, and better control in nanostructure building. The MW PECVD technique was employed for the preparation of graphene samples of this research work. Other modifications of the CVD method are also applied for planar and VGN deposition [53,54,71,72] and are listed in **Figure 3**.

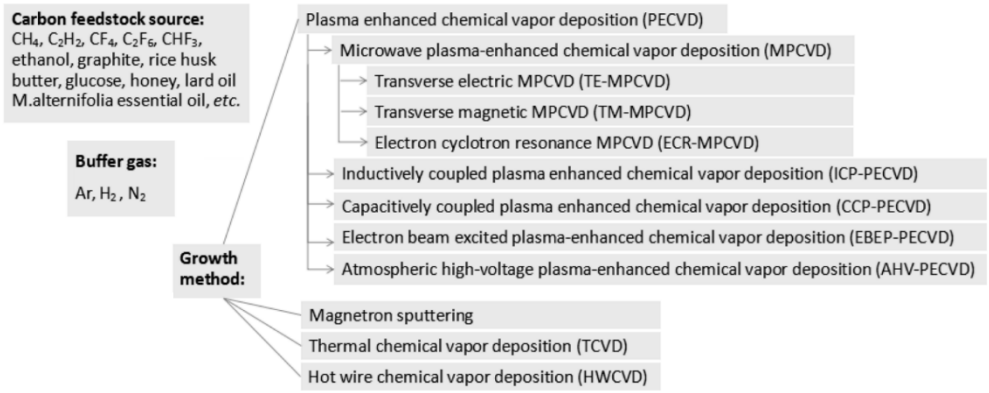

Figure 3. Various modifications of chemical vapour deposition technique [54]

Recently, CVD has become the most practical growth technique of planar graphene for various optoelectronic devices applications because of the synthesis of large-area graphene films with high crystallinity and the large grain size on metal substrates (e.g., copper, nickel) [73,74]. The graphene produced by this method is denoted by high quality, uniform single or several layers, and the capability to be transferred onto various substrates at a low cost [75–78]. Despite all the fabrication benefits of MW PECVD, the transfer process might induce mechanical damage as well as chemical contamination. Nevertheless, it is highly promising for applications to produce high-quality graphene films on a wide range of substrates directly without a metallic catalyst [27,73] [A2]. A lot of research is designated to the direct synthesis of vertical graphene nanosheets on semiconductor, dielectric (e.g., Si, SiO_2, fused silica, Al_2O_3) substrates. As these materials are catalytically inert [73], the control of graphene growth on these substrates is a fairly complicated task so far. Furthermore, the deposition process is strongly influenced by the plasma source and a series of operation parameters. It is worth noting that it is not easy to confine the MW power, and the spread of MW could lead to the reduction in growth efficiency and uniformity of the morphology and the structure of as-grown VGN [72].

The addition of Ar to carbon source produces a more stable plasma capable of providing electrons of promoted energy and the sufficient level of the ionisation rate, which would enhance the synthesis process. Another advantage of Ar addition is that it could enhance the formation of critical species for VGN growth. N_2 can serve as an effective a-C etchant for VGN growth. The usage of N_2 instead of H_2 in the removal of excess a-C can even be advantageous [79]. The substrate temperature is very significant to the synthesis process by MW PECVD as it strongly affects the surface reaction kinetics. A higher substrate temperature offers more species for nucleation and thus favours the VGN growth rate [80].

The thickness of the nanosheets as well as their length, surface density and good individualization of sheets could be tuned by modifying the pressure during the deposition process, or the flow rate of the main carrier gas. These synthesis parameters play a significant role as they control the duration of transport to the substrate, the incidence of collisions, the quantity and the state of species responsible for the deposition and nanostructuring of the growing material. The

thickness of nanosheets increases with the increase of the carrier flow, and the decrease of pressure [81]. Furthermore, the application of higher power and the concentration of the feeding gas, as well as the decrease of the distance between the substrate and the gas injection point also result in thicker nanosheets [82,83]. By changing these key parameters, nanosheets with a wall thickness from a few to dozens of nanometers can be obtained.

2.3. Quality studies of graphene films

The tools usually used for defects and structure analysis are scanning and transmission electron microscopy (SEM and TEM), atomic force microscopy (AFM), Raman scattering spectroscopy, elemental analysis by Energy dispersive X-ray analysis (EDX), or X-ray photoelectron spectrometry (XPS) [11,84–86]. SEM, TEM, AFM, EDX and XPS are relatively traditional techniques denoted by a wide range of applications, and, in the following section, on the more specific methods shall be concentrated, such as the Raman scattering spectroscopy and the transient absorption spectroscopy.

2.3.1. Raman scattering spectroscopy

One of the best-developed methods to characterise graphene films is the Raman scattering spectroscopy due to being non-destructive, fast, extremely sensitive and, so far, providing the maximum structural information about graphitic materials [31,87]. In addition to identifying the crystalline state, it is advantageous to investigate defects and disorder. It has also become a well-established and powerful technique for understanding the behaviour of electrons and phonons in graphene layers [88].

The typical Raman spectra of planar graphene and vertical graphene nanosheets are presented in **Figure 4**.

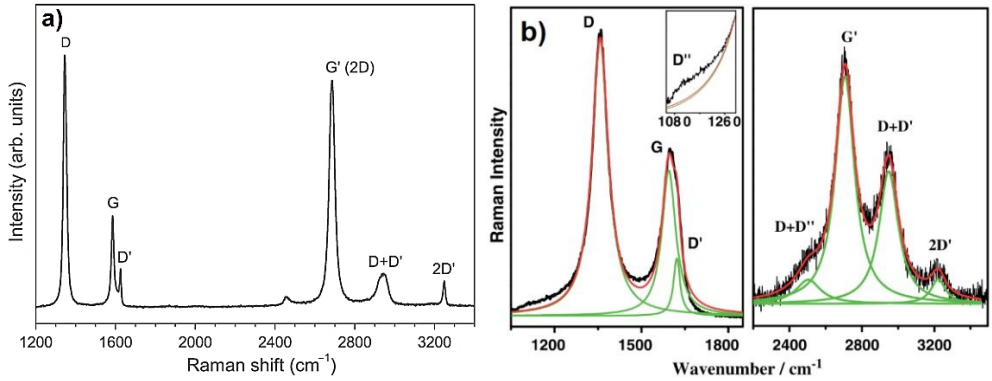

Figure 4. Typical Raman spectra of an ion-bombarded planar graphene (**a**) [89] and vertical graphene nanosheets grown on SiO_2/Si by ECR-CVD and its deconvolution with the Lorentzian line shape (**b**) [53]

The most prominent characteristics in the Raman spectra of graphene films are G and 2D bands verifying the crystalline structure. The G (~1590 cm^{-1}) band originates from a normal first order Raman scattering process in graphene and is

associated with the doubly degenerate (in-plane transverse optical (iTO) and longitudinal optical (LO)) phonon mode at the Brillouin zone centre (the Γ point) (**Figure 5 a**) [90]. The G band is an in-plane vibrational mode involving the sp^2 hybridised carbon atoms of graphene. The 2D band (~2700 cm^{-1}) comes from an intervalley second-order double resonance (DR) or triple resonance (TR) Raman scattering in the vicinity of two non-equivalent K and K' points (Dirac cones) involving two iTO phonons or one iTO and one LA phonon (**Figure 5 d**, **e**). All scattering events are inelastic and without defects getting involved [30,91] [A2].

The D band at ~1350 cm^{-1} (PosD) coming from the two intervalley DR scattering processes consists of one elastic scattering event by defects and one inelastic scattering event by emitting or absorbing an iTO phonon (**Figure 5 b**). The D′ (~1620 cm^{-1}) and 2D′ (~3225 cm^{-1}) bands originate from intravalley DR processes involving one LO phonon near the Γ point and one defect in the case of the D′ band and two LO phonons for the 2D′ band (**Figure 5 c**). The latter is the overtone of the D′ band which can also be activated by TR Raman scattering. The D+D″ band (~2475 cm^{-1}) is a combination of a D phonon and a phonon belonging to the LA branch near the K point at ~1200 cm^{-1} which is assigned to the weak and broad D″ band, [2,35,36]. These defect-related bands are the result of defects and disorder.

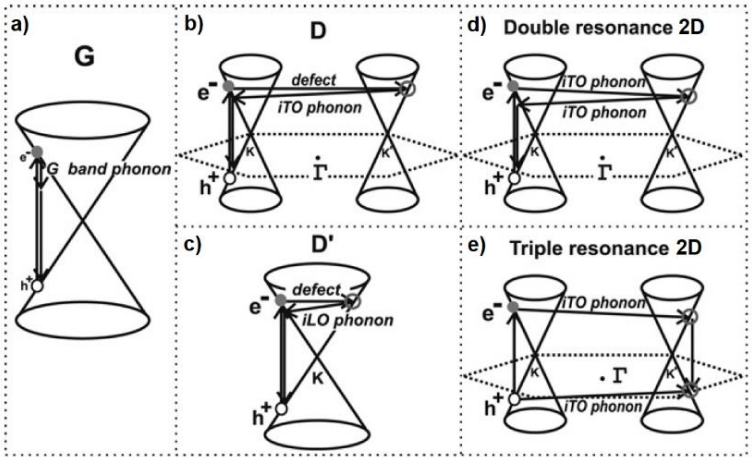

Figure 5. First-order G band process (**a**), one-phonon second-order DR intervalley process for the D band (**b**) and intravalley process for the D′ band (**c**), and two-phonon second-order processes for the double resonance 2D process (**d**) and for the triple resonance 2D band process (**e**) for monolayer graphene [31]. Resonance points are shown as open circles near the K and K′ points

In order to define what the peaks stand for in the Raman spectra is significant for the explanation and analysis of the defects and disorder of graphene. Raman scattering spectroscopy is considered to be the best method for defects of graphene analysis so far. Therefore, the clarification of Raman scattering spectra data is highly useful for the explanation about how the graphene defects influence the TAS results. The phonons that interact with hot electrons are usually shown in Raman scattering

spectra; therefore, for TAS data interpretation, the understanding of the Raman spectra of graphene is important.

As it was mentioned above, the D, D′, 2D′, D″, D+D′, and D+D″ bands are initiated only by defects and disorder and are strongly dispersive with excitation energy [42]. These peaks are absent in pristine (defect-free) graphene. What is more, the decrease of FWHM of G and 2D bands implies the reduction of defects and disorder in graphene along with the growth time. According to their origin, the defects can be specified as vacancies, implanted atoms, grain boundaries, edges, and disorder due to an alteration in carbon hybridization from sp^2 to sp^3 [92]. A few or more types of defects are typically present in graphene films.

It is known that the intensity ratio I_D/I_G provides a measure of defects in the disordered graphitic system. It was revealed that the behaviour of the I_D/I_G ratio is non-monotonic with the growth duration, and this can be explained by the presence of two defect-induced competing mechanisms conditioning the D peak intensity [53]. This variation of the I_D/I_G ratio can be explained in terms of the well-defined defects/disorder model offered by Ferrari and Robertson [93].

The conversion from highly crystalline (sp^2-bonded) graphite into highly disordered (sp^3-bonded) tetrahedral amorphous carbon (ta-C) takes place in three stages [53]:

1) graphite to nanocrystalline graphite (low disorder). I_D is directly proportional to the amount of defects;

2) nanocrystalline graphite to low sp^3 a-C (high disorder). I_D is inversely proportional to defects;

3) low sp^3 a-C to high sp^3 ta-C.

I_G is always proportional to the quantity of sp^2-bonded C atoms in the sample [94,95]. When the defect concentration is relatively large, it is more appropriate to take the intensity ratio I_D/I_G rather than the peak area ratio A_D/A_G. A_D/A_G is more accurate for the layers with a low defect density.

For the development of the specific properties of graphene, it is important to understand the relation between the kind of defects and its Raman scattering process as defects have a significant impact in determining the physical (e.g., optical, electronic, magnetic) and mechanical properties of graphitic structures [96]. A lot of research is designated to explore the nature and quantification of defects in graphene by creating a specific type of defects through fluorination, hydrogenation, mild oxidation, anodic bonding, plasma surface modification, Ar^+-bombardment [94,97–100]. The ratio of $I_D/I_{D'}$ depends on the physical origin of the defect but is independent from the defect concentration present in the material [92]. According to a systematic analysis of the relationship of all types of defects, if the ratio of $I_D/I_{D'}$ is:

- 13 – it corresponds to sp^3-type defects;
- 10.5 – it indicates the presence of hopping defects;
- 7 – it applies for vacancy-like defects;
- 3.5 – it refers to boundary-like defects;
- 1.3 – it represents the on-site defects in graphene [53,92,101].

The quantitative and qualitative characterisation of various defects in graphene-based materials by Raman spectroscopy is of intense research interest.

2.3.2. Transient absorption spectroscopy

Transient absorption spectroscopy (TAS) is a pump-probe spectroscopic technique used to record the photogenerated excited state relaxation absorption energies and the associated lifetimes of materials and devices.

The main principle of pump-probe spectroscopy (or TAS) is as follows: the test sample is excited by one 'strong' short laser pulse (pump), and the other 'weak' pulse (probe), coming after a certain time period from the first one, which inspects how the absorption of the sample has changed due to the first pulse impact. By varying the delay time of the second pulse compared to the first pulse, the dynamics over time of the absorption spectrum is obtained. TAS measures alterations in absorption caused by changes in both the excited state and in the ground state of the sample. Thus, the differential absorption can be expressed by Equation 1 [102]:

$$\Delta A \equiv A_{pumped}(t) - A_{unpumped}(0) = \lg \frac{I_{unpumped}}{I_{pumped}} \qquad \text{(Eq. 1)}$$

The possible types of signals obtained in a transient absorption experiment are shown in **Figure 6** [103,104]. When a sample is excited by a pump beam, some electrons jump into the excited state, and the concentration of electrons in the ground state decreases. Hence, at the wavelength where the electrons absorb, the absorption disappears, and the differential absorption signal acquires a negative value. This part of the signal is called *ground state bleach* (GSB). Another contribution to the TAS signal is related to the *stimulated emission* (SE). It occurs because the photons of the probing beam can force electrons being in the excited state to emit photons of the same polarisation, direction, and wavelength as the incoming photons of the probing beam which dropped electrons to the ground state. This signal will make a negative contribution to the differential absorption. The third part to the TAS signal is the *excited state absorption* (ESA) which appears when the electrons in the excited state absorb another photon from the probing beam and move to an even higher electronic state. This process can only take place in excited electrons; hence, when the sample is illuminated by the pump beam, additional absorption arises, i.e., this contribution to the ΔA signal is positive [102].

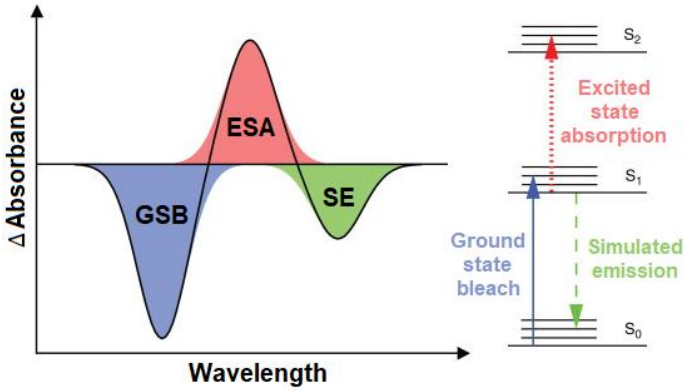

Figure 6. Possible types of signals obtained in a transient absorption experiment where the differential absorbance is plotted as a function of probe wavelength [103]

The processes that appear during the excited state relaxation dynamics of graphene could be summarised as follows:

- firstly, photoexcitation and electron-hole pair generation centred at a half of the excitation photon energy with respect to the Dirac point [105,106];
- secondly, electron heating through electron-electron (carrier-carrier) scattering, in competition with lattice heating (with the typical time interval of ~10–50 fs);
- thirdly, electron cooling by thermal equilibration with the lattice (electron-phonon scattering that is also called electron-optical phonon scattering [107]) (> 100 fs) [37,108].

There can also be slow relaxation dynamics that can be attributed to interfacial heat flow from graphene to substrate, i.e., phonon-phonon scattering (~2 ps) [36,37,108]. The electron-hole recombination is also possible. It results in luminescence with very low efficiency of 10^{-9} for high quality graphene [109].

Monitoring the TAS signal enables the direct measurements of the hot-electron relaxation in real time [35]. In other words, the TAS decay curves could be described as a hot-electron thermometer that records the cooling dynamics of hot electrons in graphene [36] [A2]. The cooling of hot electrons in graphene appears because of the electron-phonon interaction.

The optical phonons which have the largest influence on electron-optical phonon scattering are intravalley Γ-point E_{2g} optical phonons and intervalley $K(K')$-point A'_1 phonons [42,110]. Hot optical phonon decay times are about 2.5–3 ps [110]. These optical phonons Γ-point E_{2g} and $K(K')$-point A'_1 can be clearly seen in Raman scattering spectra and correspond to their G and 2D (in some papers referred to as G′ [31]) peaks, respectively. These phonons are responsible for the electron-phonon coupling process; therefore, their influence is directly observed on the excited state relaxation dynamics with TAS.

Most studies based on the transient absorption spectroscopy (TAS) of graphene layers were done in near-IR or MID-IR region and were largely obtained by using single wavelength TAS. It was only recently that some studies in the UV region were performed [37]. In this work, the planar and vertical graphene samples were excited, and their TAS properties were measured under excitation and probing in the UV and VIS region.

It was demonstrated that the charge relaxation dynamics of high-quality graphene consist of fast (electron-phonon scattering) and longer-lasting (phonon-phonon scattering) components [36]. It is known that the relaxation decay times measured with TAS are longer for pristine graphene in comparison with graphene containing various defects [36]. Furthermore, phonon-phonon scattering was registered with TAS only in high-quality pristine-like graphene samples [36] suggesting the relative amplitude of the longer-lasting TAS relaxation component being an indicator of the quality factor. Therefore, the analysis of this particular longer-lasting TAS signal decay component achievable with < 300 fs pulse length TAS systems could become the evaluation standard of the graphene quality. Aiming to elucidate the influence of planar graphene and VGN defects on their ultrafast

relaxation dynamics, samples with different known defects should be investigated [A1].

The application of TAS in the studies of defects and disorder is a promising subject of intense research, mainly because of the capability of measuring ultrafast relaxation dynamics of the excited state of graphene and providing additional information about ultrafast processes that Raman scattering spectroscopy lacks [36].

In this work, transient absorption spectroscopy (TAS) was successfully implemented for the determination of the quality of planar and vertical graphene nanosheets [A2].

2.4. Applications of graphene layers

In recent years, graphene has been shown to be a promising material for various electro-optical applications, such as photodetectors [50], photovoltaics [111,112], solar energy conversion [111,113,114], photocatalysis [115,116], detection of optical and X-ray photons [117], transistors [118,119], ultrafast lasers [106,120], electrodes [50,121], light-emitting devices [122], touch screens [123,124], biomedicine [125–127] and other applications in the fields of photonics, plasmonics and optoelectronics [75,128,129]. For some applications, the presence of a bandgap in graphene is necessary. Fortunately, the formation of a bandgap is a relatively simple process based on doping or the formation of defects [130–133]. Despite some negative connotations, understanding the influence of such defects on the charge carrier dynamics and relaxation pathways is key to the modification of the optoelectronic properties of graphene-based devices [130] [A2].

Particularly, vertically oriented graphene – two-dimensional (2D) graphene nanosheets arranged perpendicularly to the substrate (also known as carbon nanowalls or *vertical graphene nanosheets* – VGN) – has attracted the interest of many researchers [25,134]. This kind of graphene possesses many unique electrical, chemical, and mechanical properties compared with its planar counterpart. Due to the sharp, dense, upwards-exposing edges, abundant active sites, high porosity and the developed spatial morphology, VGN can be directly integrated into functional devices, such as Li-ion batteries [135], field-emission cold cathodes [58], biochemical sensors [136], microenergy conversion and storage devices, supercapacitors [137,138], flexible electronics and wearable devices [139,140], optoelectronics or catalysts [25,134,141]. For instance, in [142], it was demonstrated, that a gas sensor employing a layer of vertical graphene nano-petals exhibits superior sensitivity due to the extremely high specific surface area, and down to the parts-per-trillion (ppt) level of NH_3 detection capabilities was reported. VGN nanomaterials are expected to become even more popular in the near future [54] [A1].

III. WORK METHODOLOGY

3.1. Microwave plasma-enhanced chemical vapour deposition of graphene layers

By employing the *microwave plasma-enhanced chemical vapour deposition* (MW PECVD) technique (IPLAS Innovative Plasma Systems GmbH) [143], large area graphene layers were deposited in two ways resulting in structural differences – on the metallic catalyst (Cu foil) for the production of continuous films possessing an intrinsic planar structure, and directly on insulating substrates (fused silica), thus initiating the formation of vertical graphene nanosheets (VGN) [A1, A2].

An MW PACVD system's *CYRANNUS I-6"* (**Figure 7**) (plasma source (2.45 GHz)) reactor consists of a cylindrical stainless steel chamber and a sample holder with a heater which enables to control the substrate temperature independently of microwave power.

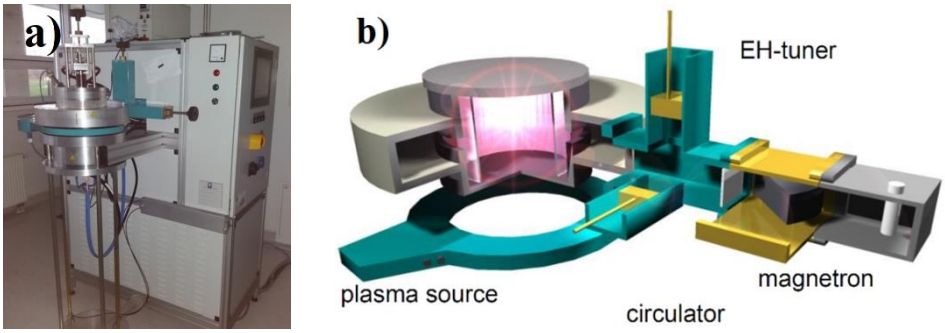

Figure 7. MW PECVD device *CYRANNUS I-6* (**a**) cylindrical resonator with annular slots (**b**) [144]

3.1.1. Planar graphene synthesis on a catalyst – copper substrate

In the case of the synthesis of planar graphene, commercial Cu foil of 45 μm thickness and 19 mm × 19 mm dimensions was placed on a special metal pad with a hole in the centre to lift foil up from the sample holder and thus reduce the temperature losses during the synthesis process (**Figure 8**). To begin with, Cu foil was pre-cleaned by hydrogen plasma at 1.3 kW microwave (MW) power and heated up to 550ºC temperature (with no use of an additional heater) naturally by MW induction and plasma species collisions. In such a way, the Cu (111) surface can be obtained with good lattice matching to graphene [145]. After 30 min, the growth process was started by injecting CH_4 as a carbon source with a 25 sccm flow rate while using MW power of 1.1 kW, whereas other parameters were kept unchanged: H_2 flow rate of 200 sccm, 30 mbar discharge pressure, and constant 550ºC temperature. After maintaining the growth stage of 10 min, the plasma was shut off, the samples were cooled down to room temperature and taken out for the transfer process and further characterisation.

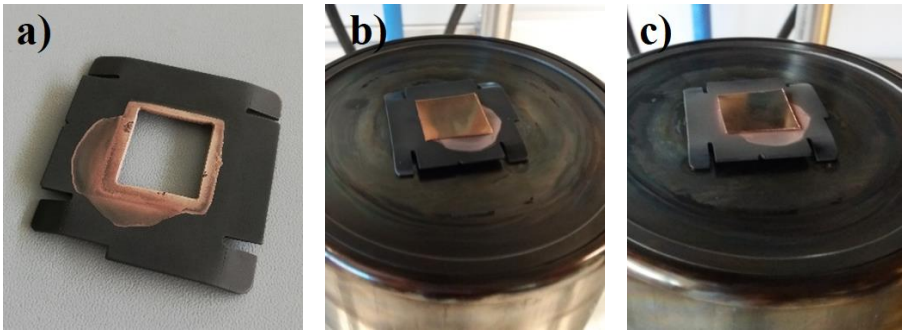

Figure 8. Copper foil (19 mm × 19 mm) on the sample holder of *CYRANNUS I-6* system with a special metal pad (40 mm × 40 mm) (**a**) before (**b**) and after deposition of graphene (**c**)

3.1.2. Catalyst-free synthesis of vertical graphene nanosheets on dielectric substrates by using special enclosures

Before VGN synthesis on fused silica, the substrates were chemically cleaned in acetone (10 min), C_3H_8O (10 min), and deionised water (10 min) by using an ultrasonic bath and were dried by N_2 flow.

The MW PECVD system is designed in the way of the so-called direct plasma treatment as the substrates are treated within the area of plasma generation. In order to set up the deposition conditions specifically suitable for the synthesis of vertical graphene nanosheets layers, additional custom-built protective enclosures were used (**Figure 9**) [146]. These metal enclosures of a particular design served as a shielding cover on the sample to keep the plasma remote from the substrate surface. Different numbers and sizes of holes and open side walls within these enclosures ensure the controllable distribution of the electric field and the access of the active species in the vicinity of the sample.

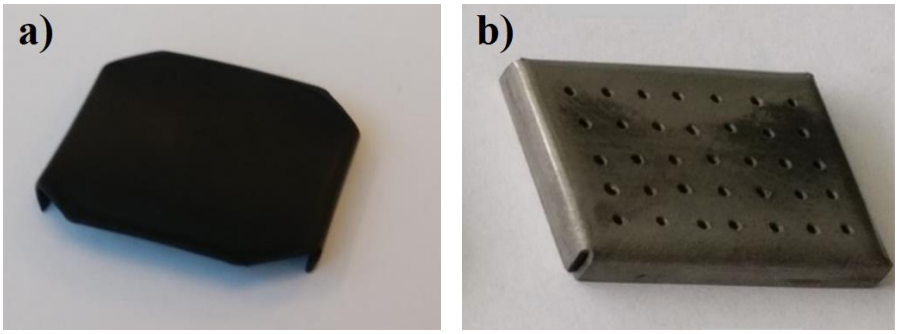

Figure 9. Special metal protective enclosures: the first with two open side walls and no holes (**a**), and the second with closed walls and 35 holes on top (**b**)

Vertical graphene nanosheet (VGN) layers possessing a structure of a vertically aligned graphene nanosheet network on a continuous initial base layer composed of nanographitic domains (a detailed explanation of the formation and structure of VGN layers is given in Section 4.1.2.) were deposited directly on 15 mm × 15 mm insulating fused silica substrates of 0.5 mm thickness. For this, a

catalyst-free deposition two-step synthesis process was used. For the first set of VGN samples (as discussed in Section 4.1.) preparation, firstly, the substrates were pre-treated in hydrogen plasma under a flow rate of 200 sccm at 26 mbar pressure and 1.2 kW microwave power in order to remove any organic residues, oxides and activate the growth sites. The substrate temperature was increased up to 850ºC (by using a substrate heater and remote plasma) and kept constant afterwards. After 15 min of the preheating process, methane gas was introduced into the reactor chamber at 50 sccm flow rate for 20 and 40 min, and, subsequently, H_2 gas flow was reduced to 150 sccm. The operating pressure was kept the same at 26 mbar during both preheating and the growth process. VGN samples prepared by introducing methane gas into the reactor chamber for 20 min and 40 min further shall further be called *VGN 20 min* and *VGN 40 min*, respectively.

For the formation of the second set of VGN samples (as discussed in Section 4.2.), the annealing stage parameters were selected as follows: H_2 flow rate of 200 sccm, 22 mbar pressure, 1.2 kW microwave power, whereas the temperature was increased to 800ºC and kept constant for 10 min. The growth stage parameters were set as follows: the hydrogen gas flow was reduced to 150 sccm, the methane gas flow rate was 50 sccm while maintaining 22 mbar pressure, 1.2 kW microwave power, and stable 800ºC temperature. The growth durations were chosen to be 20, 40, 60, 80, 100, and 140 min thus aiming to disclose the evolution of VGN growth.

The feedstock CH_4/H_2 gas ratio of 1:3 was selected after a set of preliminary experiments leading to a 'somewhat optimal' process enabling the best crystallinity of VGN. The CH_4 concentration was kept high enough to ensure intense nucleation and the consequently increased VGN density [72].

3.1.3. Commercial planar graphene

For the comparative analysis, commercial planar monolayer graphene produced by the chemical vapour deposition method was purchased from the *Graphenea* (Spain) company. It had already been transferred on a fused silica substrate of 0.5 mm thickness by a wet transfer process and possessed the following properties [147]:

- Number of graphene layers: 1;
- Grain size: up to 20 μm;
- Transparency: > 97%;
- AFM thickness (air @RT): < 1 nm;
- Raman scattering spectroscopy parameters: $I_G/I_{2D} < 0.7$; $I_D/I_G < 0.1$;

Sheet resistance on fused silica: 360±50 Ohms/sq. (1 cm × 1 cm).

3.2. Graphene transfer

In order to obtain all synthesized graphene samples on fused silica substrates for further characterisation, the transfer process of graphene deposited on the metallic catalyst was performed. Graphene was released from the copper substrate after the wet etching of Cu foil in an etchant. Three different etchants were used:

a) copper etchant ($FeCl_3$: 30–50%, HCl: 1–5%, *Sigma-Aldrich*).

b) chromium etchant ($CeH_8N_8O_{18}$: 20–25%, HNO_3: 5–10%, *Sigma-Aldrich*); also applicable for copper dissolution.

c) $FeCl_3 \cdot 6H_2O$ (*Eurochemicals*) aqueous solution prepared by dissolving $FeCl_3 \cdot 6H_2O$ powder in deionised water.

After the complete dissolution of Cu foil at room temperature, a floating graphene film was subsequently placed on deionised water surface for 24-hour cleaning. Cleaning was repeated for several cycles by replacing deionised water with a new substituent. The floating graphene film was then transferred onto the target substrate – fused silica – and finally left to dry in atmospheric air. The graphene transfer process was successfully accomplished without using poly(methyl methacrylate) (PMMA) as a support top-layer [148,149] so that to avoid the introduction of additional contamination and defects into the graphene film, even though it was more complicated to preserve large area graphene in the non-disintegrated state [A2].

3.3. Analytical methods

3.3.1. Scanning electron microscopy

Our surface imaging studies were carried out by using a scanning electron microscope (SEM) *Quanta 200 FEG* (*ThermoFisher Scientific*, USA) comprising a Schottky type field emission electron gun ensuring 1.2 nm resolution under the high vacuum mode and 30 kV accelerating voltage. The samples were tilted by 45° or 90° during the SEM inspection thereby aiming for the three-dimensional impression of the VGN network and the actual height of the nanostructures, respectively.

Cross-section SEM images were taken by using a dual-beam system *Helios Nanolab 650* (FEI, NLD) with a Schottky type field emission electron (FE) gun and a gallium ion gun (FIB): 30 kV accelerating voltage, resolution of 0.8 nm (2–30 kV) for the structural investigation of the VGN layers and the thickness estimation while additionally utilizing the *ImageJ 1.52a* program. Before breaking, the Cr layers were deposited on the samples by magnetron sputtering while employing a *Quorum Q150T* ES coater (Ar plasma, U – 2 kW, I – 100 mA, p – 10 mBar Ar, t – 15 s, the target-sample distance – 6 cm) [A1, A2].

3.3.2. Atomic force microscopy

Quantitative surface morphology examinations in terms of roughness were performed in a cleanroom (ISO 5 class) by using the atomic force microscopy (AFM) system *NanoWizard* 3 (*JPK*, *Bruker*, GER) and the data processing software *Gwyddion-2.49.win64*. An I-shaped silicon cantilever (*ACTA-AppNano*, USA) operating in the contact and dynamic modes in the resonant frequency of 300 kHz with a spring constant of 13–77 N/m and a 10.0 nm curvature radius tip was used in the measurements [A1, A2].

3.3.3. Raman scattering spectroscopy

Raman spectroscopy, known as a non-destructive, well established and highly sensitive technique, which has already been widely used to ascertain the structure, electronic, optical, and phonon properties in the family of carbon materials [42], was

used to investigate the quality, defects and disorder of MW PECVD-grown graphene layers.

A Raman scattering spectrometer *inVia* (*Renishaw*, UK) equipped with a 532 nm wavelength diode-pumped solid state laser, a grating containing 2400 grooves/mm, a thermoelectrically cooled CCD camera of 1024 pixels ensuring the spectral resolution not worse than 1 cm^{-1} was employed to determine the characteristic G, D and 2D bands directly related to the quality of the investigated graphene nanostructures. The laser power level at the sample was 2.25 mW, the integration time was 10 s, and the diameter of the laser beam was 4 μm. Raman spectra were taken by using a confocal microscope *Leica* with a 50× magnification 0.75 NA objective lens. Raman data were analysed by using the *OMNIC32v7.2.0.616* software, and the peaks were fitted with Lorentzian functions [A1, A2].

3.3.4. X-ray photoelectron spectroscopy

X-ray photoelectron spectroscopy (XPS) analysis, which is widely employed in the graphene research community for the characterisation of the chemical composition as well as the bonding structure of the surface, was performed by using a *Thermo Scientific ESCALAB 250Xi* spectrometer with monochromatic Al Kα radiation (hv = 1486.6 eV) as the excitation source. The energy scale of the system was calibrated with respect to Au $4f_{7/2}$, Ag $3d_{5/2}$ and Cu $2p_{3/2}$ peak positions. For the peak deconvolution and calculation of atomic concentration, original *Thermo Scientific Advantage* software (v5.979) was used. For the peak fitting procedure, the Shirley background and a sum of Lorentzian-Gaussian (70:30) functions for the asymmetric graphitic carbon peak and (30:70) for the rest of the peaks was applied [A2].

3.3.5. Electrical measurements

Current-voltage measurements applying the transmission line model (TLM) pattern [150] were carried out in air at room temperature by using two probes employing a *6487* picoammeter (*Keithley*, USA). The TLM structures with fixed contact lengths of 0.25 mm and a width (W) of 3.0 mm and a varying channel length (L) from 0.3 mm to 1.5 mm (following nL, n = 1, 2, 3, 4, 5; tendency) were used for the measurements (**Figure 10 a**). Copper was deposited as ohmic contacts of ~250 nm thickness on top of the VGN films by e-beam evaporation through a femtosecond laser cut copper stencil mask of 45 μm thickness. The explanatory plot of the total resistance R_T vs. the channel length L for the determination of sheet resistance R_S from the slope of the fitted line is given in **Figure 10 b** (where W is the contact width, R_C is the contact resistance, L_T is the transfer length beneath the contact) [A1, A2].

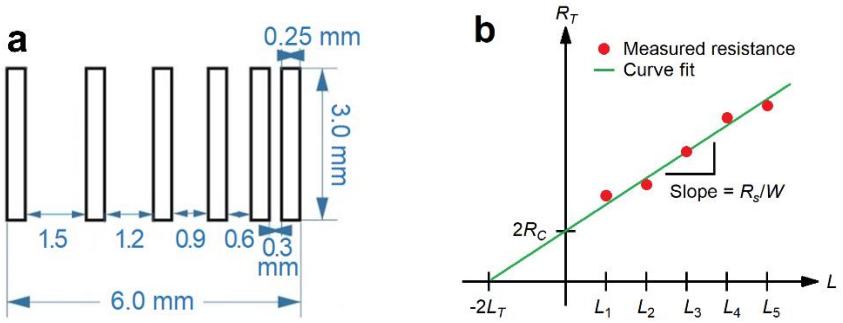

Figure 10. Electrical contact geometry (**a**), the principal plot of total resistance R_T vs. channel length L (where W – contact width, R_C – contact resistance, L_T – transfer length beneath the contact) (**b**)

The electrical resistance R and I-V characteristics as a function of temperature T and magnetic field B were evaluated by using a cryogenic measuring system (*CCRS, Cryogenics Ltd*., UK) based on a closed-cycle refrigerator in the temperature range of 2 K < T < 300 K and magnetic fields with induction B up to 8 T. The current passing through the sample was set and measured by employing a *Keithley 6430* instrument (*Keithley Instruments*, USA) which allowed to estimate the electrical resistance of VGN layers in the range from 100 μΩ to 10 GΩ with an accuracy no worse than 0.1%. The temperature of the samples was controlled by thermal diodes (*Lake Shore Cryotronics*, USA) calibrated with an accuracy of 0.005 K and having a reproducibility of at least 0.001 K by using a *LakeShore 331* measuring controller. The resistance measurements were carried out by using a 4-probe technique where two current and two voltage contacts were applied with an ultrasonic soldering iron (**Figure 11 a**).

Magnetic field B was applied either normally to the substrate surface or in parallel to it, but, normally, to the electric field being applied. The relative magnetoresistance is defined as:

$$MR = \frac{R(B)-R(0)}{R(0)} \cdot 100\%; \qquad \text{(Eq. 2)}$$

where $R(B)$ is the resistance in the applied field with induction B. The measured samples were arranged on the contact pad (**Figure 11 b**) by using 4 indium (In) supersonically soldered electric contacts with soldered 50 μm diameter copper wires. The measurement cell with a sample on the contact pad was placed in a special measuring probe that included *LakeShore* thermometers and magnetic field sensors, heaters, heated thermal shields, all in He gas atmosphere under low pressure. The probe was inserted into a channel of a superconducting solenoid inside the cryostat in *CCRS*.

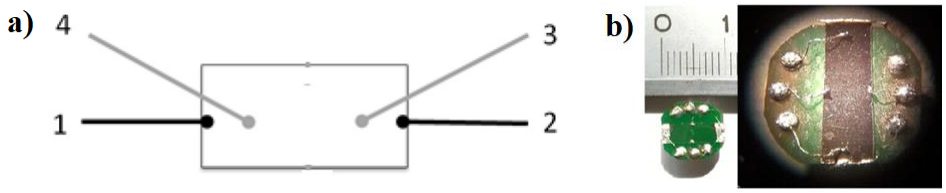

Figure 11. Scheme of the arrangement of electric probes where 1, 2 are current contacts; 3, 4 are potential contacts (**a**). View of the sample on contact pad (**b**)

3.3.6. Ultraviolet-visible-near infrared spectroscopy

The absorbance of VGN layers was analysed with a UV-VIS-NIR steady-state absorption spectrometer *AvaSpec-2048* and an *AvaLight-DHc* light source (*Avantes*, NED) covering the 200–1100 nm spectral range with 1.4 nm spectral resolution.

3.3.7. Transient absorption spectroscopy

Ultrafast relaxation processes in planar graphene and VGN were investigated by employing a transient absorption spectrometer (*HARPIA* spectrometer (*Light Conversion*, LT)). A typical operating principal scheme is shown in **Figure 12**, where the laser coming from the *PHAROS* is split, thus sending about 90% of the power into a parametric amplifier *ORPHEUS* whose outgoing laser is used as a pump beam to excite the sample. The rest of laser beam (about 10% of the power) is injected into the probe input of *HARPIA* and used to generate the white light supercontinuum that is later used as a probe beam to measure the sample transmittance. The difference of the sample absorbance signal in the presence and in the absence of the pump pulse may then be measured as a function of the probe wavelength and the delay between the pump and the probe pulses.

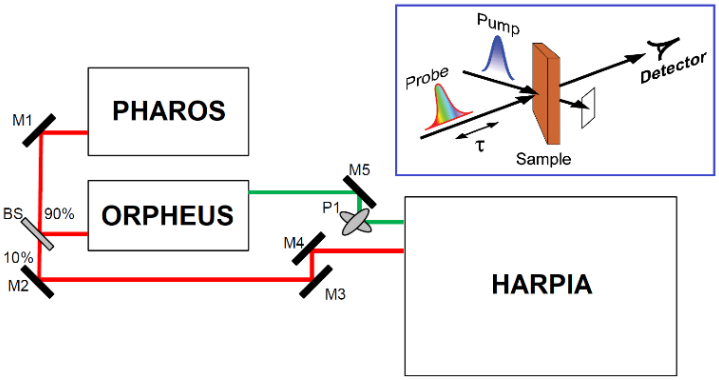

Figure 12. Standard scheme of the pump-probe system: M – mirror, BS – beam splitter, P – modulator [151]

The pump pulse and the white light supercontinuum probe are focused and aligned to intersect in the sample (**Figure 12**). The pump beam is sequentially blocked and unblocked by a mechanical chopper. The pump state is recorded by a photodiode, and the measured data points are ranked to ‘pump-on’ and ‘pump-off’, respectively. Before the actual measurement of the data, the probe beam is blocked

by the shutter, and the dark signal corresponding to both the open and the closed states of the chopper is measured. In the subsequent measurements, the values of the dark signal are subtracted from all the measured probe signals. During the actual transient absorption measurement, the spectrometer records white light supercontinuum spectra with the pump light being blocked and unblocked. The absorbance is calculated as follows:

$$\Delta OD(t,\lambda) = \lg \frac{I_{unpumped}(\lambda) - I_{dark,unpumped}(\lambda)}{I_{pumped}(t,\lambda) - I_{dark,pumped}(\lambda)} \quad \text{(Eq. 3)}$$

The separate measurements for pumped and unpumped dark spectra are necessary to account for the scattered pump light which may reach the detector. Since the measured signals are usually of the order of 0.001, the signals in the software are multiplied by a factor of 1000, i.e., they are expressed in mOD.

By measuring the difference of the absorption signals at different delays between the pump and the probe pulses, the entire pump probe dynamics of the sample may be explored. These delays are realised by delaying the probe pulse in an optical delay line consisting of a retroreflector on a motorised translation stage. The experiment parameters, the measurement sequence, the data storage and other important aspects are controlled, and the data are stored by the *HARPIA* software.

The system was excited by using an ultrafast 290 fs pulse length and a 1030 nm wavelength Yb:KGW laser *Pharos* (*Light Conversion*, LT) with a regenerative amplifier at a 66.7 kHz repetition rate. The pump beam wavelength was tuned to 350, 400 and 700 nm with a collinear optical parametric generator *Orpheus* and a harmonic generator *Lyra* (*Light Conversion*, LT), and an energy density of 17 μJ/cm^2, 19 μJ/cm^2, 24 μJ/cm^2 and 54 μJ/cm^2 was used to excite the samples. Then, the samples were probed with a white light supercontinuum generated by using a 2 mm thickness sapphire plate excited with a fundamental laser wavelength (1030 nm). The spectral range of the supercontinuum probe as well as the detection range of the TAS dynamics spanned wavelengths from 367 to 674 nm and from 491 to 794 nm. The excitation beam was focused on the approximately 700 μm diameter spot, while the diameter of the supercontinuum probe was approximately 500 μm [A1, A2].

3.3.8. Fluorescence measurements

The steady-state fluorescence spectra of planar graphene and vertical graphene nanosheets were recorded with an *Edinburgh Instruments FLS980* spectrometer at room temperature. The samples were excited by a Xenon lamp using an excitation wavelength λ_{ex} = 350 nm [A2].

3.4. Formation of the electrochromic device with graphene electrodes

Electrochromic devices or cells basically consist of two conductive electrodes between which an electrolyte characterised by ionic conductivity is placed. These devices are mainly used for optical applications; therefore, the electrodes are usually selected to be transparent to visible light. In these studies, polyethylene terephthalate (PET) substrates with conductive coatings of indium tin oxide (ITO) and transferred graphene were used as the electrodes in an electrochromic device with Prussian blue

as the active material. The research was implemented during the interdisciplinary project PP/174 at KTU and the Joint Lithuanian-Latvian-Chinese (Taiwanese) Tripartite Cooperation Programme project Grant No. S-LLT-18-2.

3.4.1. Graphene films for electrode formation

Graphene films were formed by the microwave plasma-enhanced chemical vapour deposition system *CYRANNUS I-6* which enables the synthesis of large area high quality graphene. Due to the sufficiently high growth process temperature (510°C), the synthesis of graphene could not be carried out directly on elastic polymer substrates (polyethylene terephthalate (PET)); consequently, a double layer commercial copper foil (catalyst) was used instead. After the 30 min annealing stage, 1.1 kW microwave power was used to maintain plasma of a mixture of hydrogen (flow rate 200 sccm) and methane (flow rate 25 sccm) gases, while the pressure in the chamber was 30 mbar during the growth stage which lasted 10 minutes.

In order to inspect the electrochromic material combined with elastic graphene electrodes, a wet-chemical room temperature transfer process of graphene onto foreign PET substrates without the use of a PMMA support was applied when the copper foil was completely dissolved in chromium etchant ($CeH_8N_8O_{18}$: 20–25%, HNO_3: 5–10%; *Sigma-Aldrich*) for 4 h for ensuring effective transferring results. Before the transfer, PET substrates were cleaned in plasma (temperature: 600°C, pressure: 1 Torr, N: 0.3 W/cm^3, O_2 (99.99%), duration: 40 s).

The control of successful graphene layer synthesis and the transfer was implemented by registering the structure by Raman scattering spectroscopy (*inVia*, 532 nm, *Renishaw*, UK). The ultrafast excited state relaxation dynamics of graphene on the PET substrate was investigated by the means of transient absorption spectroscopy (TAS). The samples were excited with laser pulses of 350 nm, 20.8 μJ/cm^2, 200/3 kHz.

3.4.2. Electrochromic material formation and electrochromic device testing

Electrochromic (EC) Prussian Blue (PB, $Fe_4[Fe(CN)_6]_3$) layers on top of the graphene/PET transparent electrodes were electrochemically deposited by using an aqueous solution of 0.05 M hydrochloric acid (HCl), 0.05 M potassium hexacyanoferrate (III) ($K_3[Fe(CN)_6]$), and 0.05 M iron (III) chloride ($FeCl_3$) at 1:2:2 ratio. Application of an external field between the graphene/PET electrode and the graphite counter electrode, both immersed into the solution, resulted in the homogeneous deposition of the PB layer onto the graphene/PET electrode (PB/graphene/PET).

The optical property modulation of the deposited PB layers was tested by the redox process using 1 M KCl aqueous solution as an electrolyte as depicted in **Figure 13**.

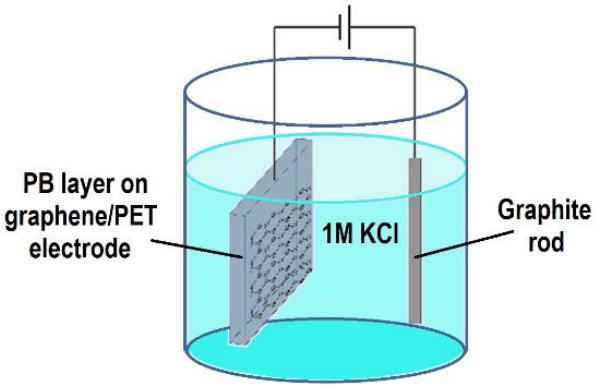

Figure 13. Testing setup of optical property modulation of the deposited PB layers on graphene/PET electrode by the redox process

The changes of the layers' transmittance under the impact of the applied voltage were registered by using UV/VIS *Avantes* spectrophotometer *AvaSpec-2048* with a deuterium and halogen light source; the spectral region – 172–1100 nm, resolution – 1.4 nm.

3.5. Formation of organic solar cells with graphene electrodes

Planar graphene layers were integrated into organic solar cells (OSC) as transparent flexible electrically conductive electrodes instead of brittle and expensive ITO electrodes. These experiments were done during the 3-month traineeship of the author at *Mads Clausen Institute* in Denmark.

3.5.1. Formation of graphene electrodes

Graphene electrodes were formed on polyethylene terephthalate (PET) substrates; therefore, initially, graphene films were deposited by the MW PECVD system *CYRANNUS I-6* on single copper foils due to the elevated synthesis temperature of 550°C. After the 30 min duration annealing stage, hydrogen plasma (P = 1.3 kW, p = 30 mbar, 200 sccm H_2 flow rate), the growth process of 10 min was initiated while using hydrogen (200 sccm) and methane (25 sccm) gas mixture (P = 1.2 kW, p = 34 mbar).

Afterwards, a wet-chemical transfer process of graphene onto DC argon plasma cleaned PET foils (*Melinex ST505*, *DuPont Teijin Films*) and fused silica substrates was implemented, during which, the copper foil was etched in a filtered (pore diameter of filter – 0.25 μm) $FeCl_3 \cdot 6H_2O$ aqueous solution (5 g powders and 50 g deionized water for each sample; *Eurochemicals*) for at least 5 h. PET substrates with graphene layers were trimmed into 15 mm × 15 mm squares as shown in **Figure 14**.

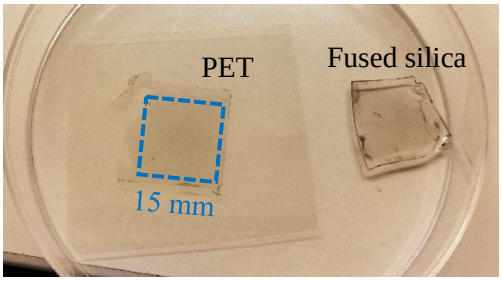

Figure 14. Transferred graphene on PET and fused silica substrates

3.5.2. Organic solar cell formation

OSC of various configurations with graphene electrodes were formed in parallel with the identical ones with ITO electrodes.

Formation of the OSC functional layers:

a) Electron transport layer (ETL). Commercial ZnO NP (H-SZ01034, *Genes'ink*) were filtered with a 0.2 μm RC filter (*Whatman*). ETL was spin-coated.

b) Active layer. The solution of PCE12 and ITIC (*Brillant Matters*) was prepared in a ratio 1:1 (PCE12:ITIC) at a total concentration of 10 mg/1.2 ml in chlorobenzene with 0.5% v/v of diiodooctane (CB:5%DIO) and stirred for 6 hours at 80°C in ambient conditions. Active layers based on the polymer/nonfullerene system were formed by spin-coating.

c) Hole transport layer (HTL). Commercial MoO_x (x = ~3) powder (99.99%, *Sigma Aldrich*) was thermally evaporated in the device cluster tool under ultra-high vacuum (10–9 mbar). The thickness of the MoO_3 films was ~10 nm estimated by the quartz crystal microbalance.

d) Electrodes. Silver contacts of ~100 nm thickness through the shadow mask defining a small-scale cell unit area of 5.4 mm² as shown in **Figure 15 a** were deposited by using DC magnetron sputtering (sputter power 150 W, sputter pressure $6 \cdot 10^{-3}$ mbar, sputter time 170 s). Thus, each sample contained four cells. For the inverted device configuration as the bottom electrode, a Bphene layer of 20 nm was formed.

All OSC samples were fabricated in a nitrogen glovebox connected to a cluster deposition tool for the overall device production.

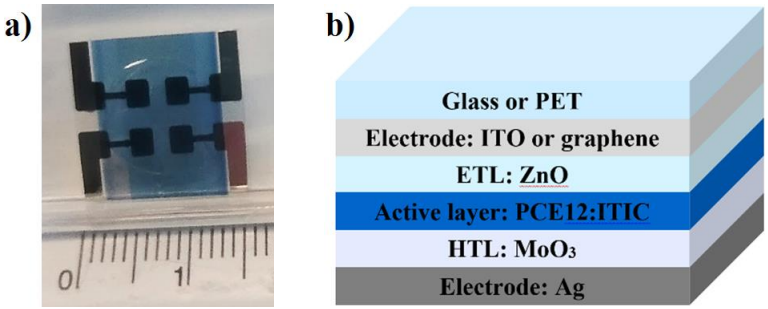

Figure 15. Organic solar cell sample (**a**), basic structure of the organic solar cell (**b**)

Device configurations used in the experiments:

a) Glass/ITO/ZnO/PCE12:ITIC/MoO_3 (10 nm)/Ag (Reference) (Inverted)
   PET/Gr/ZnO/PCE12:ITIC/MoO_3 (10 nm)/Ag (Inverted);
b) PET/Gr/MoO_3 (10 nm)/PCE12:ITIC/Bphene (20 nm)/Ag;
c) PET/Gr/*Ag evaporated (3 nm)*/ZnO/PCE12:ITIC/MoO_3 (10 nm)/Ag (Inverted);
d) PET/Gr/*Ag evaporated (3 nm)*/MoO_3 (10 nm)/PCE12:ITIC/Bphene (20 nm)/Ag;
e) Glass/ITO/*ZnO+77 nm Ag@TiO_2 NP*/PCE12:ITIC/MoO_3 (10 nm)/Ag (Inverted);
   PET/Gr/*ZnO+77 nm Ag@TiO_2 NP*/PCE12:ITIC/MoO_3 (10 nm)/Ag (Inverted);
f) Glass/ITO/*20 nm Ag NP*/ZnO/PCE12:ITIC/MoO_3 (10 nm)/Ag (Inverted)
   PET/Gr/*20 nm Ag NP*/ZnO/PCE12:ITIC/MoO_3 (10 nm)/Ag (Inverted);
g) Glass/ITO/*20 nm Ag NP*/MoO_3/PCE12:ITIC/Bphene (20 nm)/Ag
   PET/Gr/*20 nm Ag NP*/MoO_3/PCE12:ITIC/Bphene (20 nm)/Ag.

In order to enhance the performance of OSC, additional materials (marked in bold) were introduced. Silver nanocubes with the TiO_2 shell (Ag@TiO_2) were mixed with ZnO solution. More data on Ag@TiO_2 is given in [152]. The thin silver layer of 3 nm thickness was evaporated on the graphene surface by magnetron sputtering according to quartz crystal sensor readings. The dispersion of silver nanosphere of 20 nm diameter (*Sigma-Aldrich*) was spin-coated on a graphene layer.

3.5.3. Characterisation of organic solar cells

For the organic solar cells testing and evaluation, the conventional current density-voltage (*J-V*) characteristics investigation was performed under 1 sun illumination (AM1.5G light of 100 mW/cm^2) while employing a 300 class *AAA* solar simulator (*Abet Technologies Inc*.) and a *Keithley 2400* source-meter (*Keithley Instruments Inc*.). The small-scale cell units were characterised 8 by 8 by utilizing the USB eight Channel Relay controller-*RS232* serial controlled-12V with a GPIB-USB-HS IEEE488 (*National Instruments*) operated with a homemade Matlab code.

IV. RESULTS AND DISCUSSION

4.1. Studies of planar graphene and vertical graphene nanosheets layers

In this Section, detailed analysis of the properties of planar graphene (deposited by using a catalytic copper substrate and transferred on fused silica) and vertical graphene nanosheets (VGN) prepared by applying the plasma-enhanced chemical vapour deposition technique (deposited directly on fused silica substrates) is presented in the context of employing common methods (scanning electron microscopy, atomic force microscopy, X-ray photoelectron spectroscopy, and Raman scattering spectroscopy). The ultrafast transient absorption spectroscopy (TAS) technique with various excitation wavelengths (at 350, 400 and 700 nm) was used in order to investigate the excited state relaxation dynamics in various types of graphene. The morphological, structural and optical properties of graphene prepared directly on fused silica and transferred on it were analysed and related to the TAS relaxation dynamics. The results presented in this Section 4.1. were published in [A2], and the data presented in Subsection 4.1.5. were published in [A3].

4.1.1. Graphene transfer optimisation

Systematic studies on determining the conditions for the efficient transfer process of synthesised planar graphene from copper foil (45 μm thickness, 19 mm × 19 mm size) onto a target substrate were performed. For a successful graphene transfer, it is required to select the optimal concentrations of the copper etchant solutions, the etching duration and the technical implementation of the transfer itself so as not to damage the graphene film.

Three types of prepared etchants of 25 ml were used:

I) copper etchant ($FeCl_3$: 30–50%, HCl: 1–5%). Cu substrate etching time: 30 min.

II) chromium etchant ($CeH_8N_8O_{18}$: 20–25%, HNO_3: 5–10%). Etching time: 12 h.

III) $FeCl_3$ aqueous solution prepared by dissolving $FeCl_3 \cdot 6H_2O$ powder in deionised water in a ratio of 1:10. Etching time: 5 h.

The steps of the etching process are shown in **Figure 16**. The experiments with all the used solvents showed that the copper foil was fastest etched when using the copper etchant, but the film was broken. The best graphene coating quality was obtained when using the chromium etchant. Although, in this case, the etching process takes time, it is easier to control. The third $FeCl_3$ aqueous solution is also highly suitable for the effective etching process as the concentration can be easily changed, and, consequently, so can the etching duration, while preserving the non-cracked graphene film. The determined optimal etching time is about 5 hours.

The darker zones mostly on the sides of films consist of a graphene layer (on top) and an additional carbon layer (the lower one) which grows on the bottom side of the Cu foil during the synthesis. Most of the undesirable lower layer detaches during the transfer process. Accordingly, the plasma etching process of this layer can be avoided. In this way, the transferred graphene layers of about 15 mm × 15 mm dimensions can be obtained.

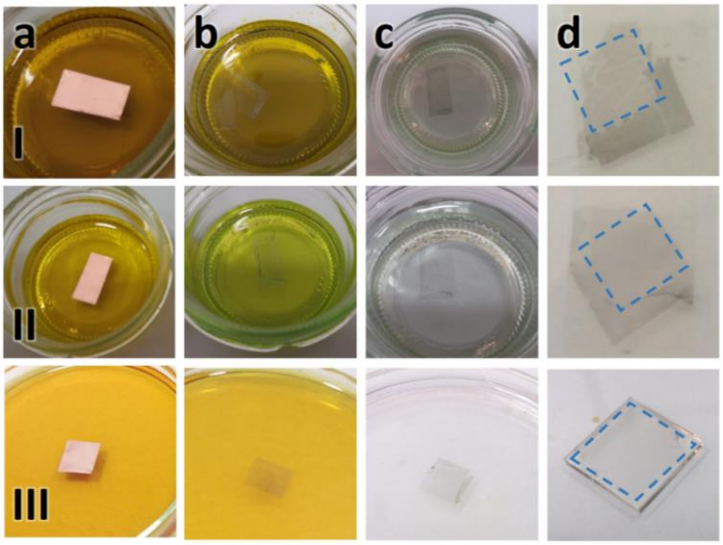

Figure 16. Graphene layer transfer process: start of copper foil etching (**a**), end of the etching: I – after 30 min, II – after 12 h, III – after 5 h (**b**), graphene film on the surface of deionised water (after replacing the solution with deionised water) (**c**), graphene layers transferred on substrates (**d**)

Other technical details of the transfer process are given in Section 3.2.

4.1.2. Morphology analysis

The surface morphology of the transferred planar graphene and VGN grown directly on fused silica substrates was characterised by SEM and AFM and is depicted in **Figure 17 a**, **b**, **c**, **Figure 19** (SEM) and **Figure 17 d**, **e**, **f** (AFM). A discernible variation in the surface morphology is observed for all the samples.

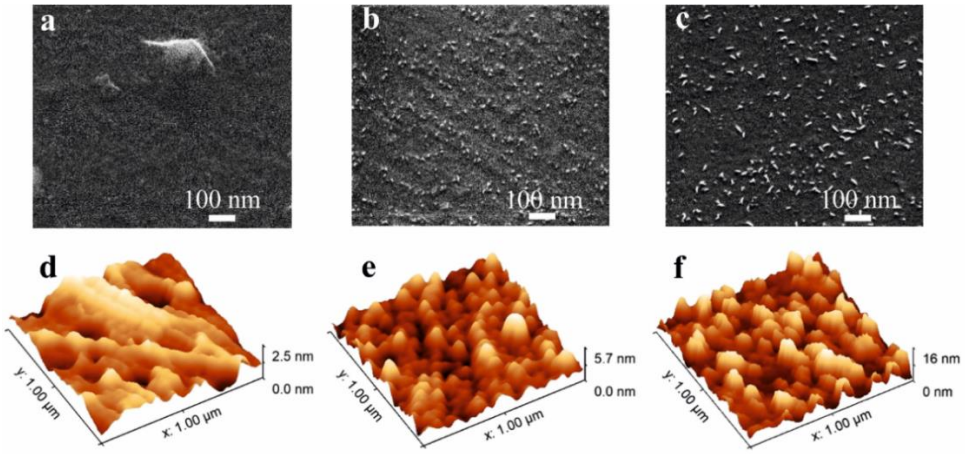

Figure 17. Top view SEM (samples were tilted by 0°) (**a**, **b**, **c**), AFM (**d**, **e**, **f**) images of transferred planar graphene (**a**, **d**), VGN grown for 20 min (**b**, **e**) and VGN grown for 40 min (**c**, **f**) on fused silica substrate [A2]

In general, for the favoured formation of graphene monolayers, the copper as a catalyst substrate is considered as a superior surface [145]. Even though the metal substrate is polycrystalline, during the growth, graphene bridges across the gaps between the metal grain boundaries. The separate areas of graphene with various lattice orientations are covalently grown together at their boundaries thereby bringing defects into the planar graphene structure which is composed of periodic chains of pentagonal and heptagonal carbon rings [153]. The synthesis via MW PECVD yields graphene in the form of a continuous horizontal film of single- and few-layers over the entire substrate surface. The SEM micrograph in **Figure 17 a** depicts the sustained graphene transferred onto a fused silica substrate with some defects and contamination coming from the transfer process, as well as the quality level of the etcher and the Cu foil [73]. The roughness arithmetic average (R_a) and the root mean square roughness (R_q) of the surface obtained when analysing AFM measurements (**Figure 17 d**) is 0.422 nm and 0.533 nm, respectively, which indicates the smoothness of the surface (**Table 1**).

Table 1. Roughness arithmetic average (R_a) and root mean square roughness (R_q) of graphene samples

	Transferred	**VGN 20 min**	**VGN 40 min**
R_a	0.422 nm	0.926 nm	2.717 nm
R_q	0.533 nm	1.176 nm	3.375 nm

What concerns the fabrication of VGN on a non-conductive substrate (fused silica), the mechanism of growth differs, and one can see (**Figure 17 b**, **c**) that this leads to structural alterations compared to planar graphene grown on metal foil. Initially, when CH_4 is inserted into the reactor, various free carbon and hydro-carbon species are generated via CH_4 easy conversion to CH_x (x = 1–3) radicals and C_2 dimers production through radical recombination and the subsequent dissociation. The reactive carbon dimers (C_2) are believed to play an important role, especially for the formation of the critical nuclei, and, later, in the VGN growth [154,155]. These active species are adsorbed onto energetically most favourable regions on the substrate surface starting the nucleation of nanographitic (NG) domains [156]. As these domains grow, they coalesce and form a particularly defective continuous interfacial nanographitic base layer containing a-C, carbon onions, pentagon and heptagon rings, as well as other defects. Then, the secondary nucleation starts, and, hereafter, the growth of vertically aligned graphene flake-like nanostructures, generally, at the defected sites of the NG base layer, such as the grain boundaries after the stress release caused by coalescence, the surface carbon onions of the NG layer [156,157]. The evolution of growth is strongly affected by the electric field as well as by a relatively high temperature and chemical potential gradients alongside the substrate surface [28,53,156]. After 20 min of growth, the film was composed of a large amount of small-size graphene sheets over the NG layer as seen in the SEM micrograph of **Figure 17 b**.

During the synthesis, H atoms simultaneously act as an effective etchant rapidly removing the undesirable amorphous phases, weaker sp^3 hybridised carbon bonds, and equally extracting bonding atoms from the gas-phase radicals, thus

acting as a co-catalyst in the formation of bonds between the surface and the carbon species, promoting the crystalline graphitic structure and the sharp edges in the layers [158]. The adsorbed carbon atoms form strong C–C covalent bonds at the edges of VGN and weak van der Waals bonds between the graphene layers which are constantly bombarded off by atomic H [53]. An illustration of the growth mechanism of VGN layers is presented in **Figure 18**. As a consequence, the length and height of the VGN increase, as can be seen in **Figure 17 c**, when the growth time increases up to 40 min. The roughness parameters R_a and R_q shoot up from 0.926 nm and 1.176 nm (for VGN grown for 20 min) to 2.717 nm and 3.375 nm (for VGN grown for 40 min) (**Table 1**). Meanwhile, the average height of the surface unevenness increased from 5.7 nm up to 16 nm for VGN 20 min and VGN 40 min, respectively (**Figure 17 e**, **f**). The surface morphology of the samples obtained by SEM and AFM differs to some extent mainly because of the samples being not tilted during SEM measurements, and, therefore, the topography is not expressed well enouth.

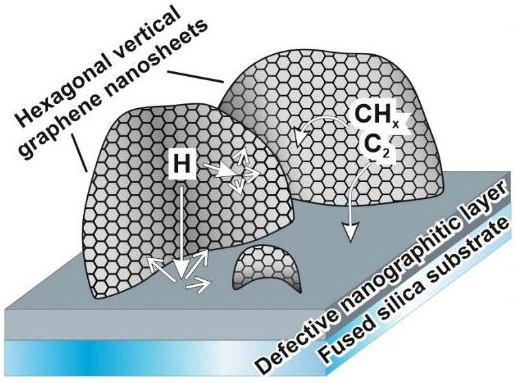

Figure 18. Illustration of the growth mechanism of VGN layers [A1]

The thickness determination of the obtained layers is more complicated. The techniques that can be applied for the planar graphene film are not always suitable for VGN samples. The thickness of planar graphene and VGN bears a completely different meaning. While the thickness in planar graphene is the thickness of a graphene film composed of one or more layers, the thickness of a VGN film is the height of graphene sheets together with the nanographitic base layer. AFM can be used for the estimation of the height of vertically aligned graphene sheets which are grown on a horizontal base layer, but not of the whole film, because there is no VGN-free area on the substrate of fused silica for the step measurements.

Cross-section SEM measurements were used for the thickness analysis of the nanographitic base layer and graphene nanosheets of VGN films. Unfortunately, the resolution of SEM was not high enough to measure the thickness of planar graphene. That is why this method was applied for the thickness analysis of VGN samples only. The received SEM data are shown in **Figure 19 a**, **b**. By using the *ImageJ* software, the thickness of VGN 20 min and VGN 40 min was calculated in 26 locations – the average values were determined to be 20.31±2.09 nm and 35.35±4.91 nm, respectively. Also, it is important to keep in mind that a thin layer of Cr was

deposited by magnetron sputtering on the scanned area before SEM measurements. The SEM measurements indicate that graphene nanosheets in the VGN 40 min sample are denoted by larger dimensions in comparison to VGN 20 min.

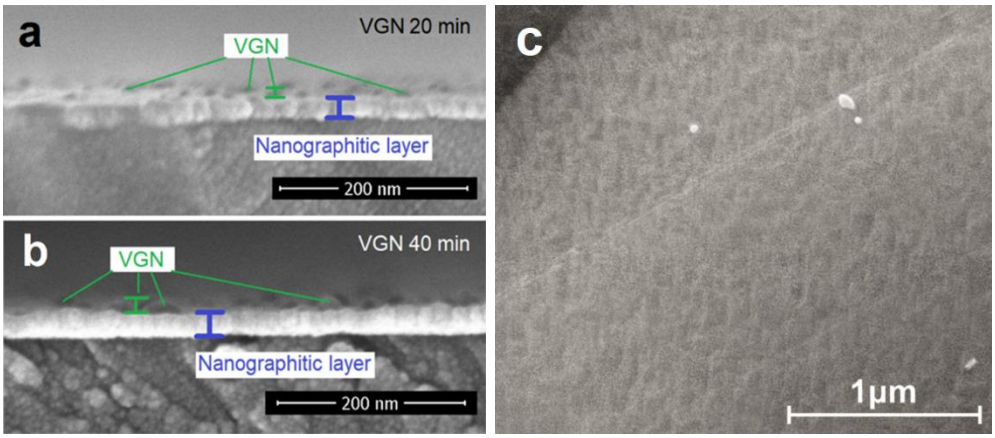

Figure 19. Cross-section SEM image of VGN 20 min (**a**) and VGN 40 min (**b**). The thickness of VGN 20 min calculated with the *ImageJ* program was 20.31±2.09 nm and 35.35±4.91 nm for VGN 40 min. Low magnification SEM image of as-grown planar graphene on Cu foil (sample was tilted by 45°) (**c**)

The low magnification SEM image of the graphene film as-grown on a Cu foil supports the planar structure of graphene all over the surface fairly well (**Figure 19 c**). The thickness of the transferred planar graphene film can be evaluated in detail by using Raman scattering spectroscopy. These results are presented below in Section 4.1.3.

4.1.3. XPS analysis

High resolution XPS spectra were scanned and deconvoluted for the calculation of surface atomic concentrations (**Table 2**) and the detection of possible carbon chemical bonds. **Figure 20 a**, **b**, **c** shows the high resolution carbon C 1s XPS spectra of the planar graphene, as well as VGN 20 and 40 min films on fused silica substrates.

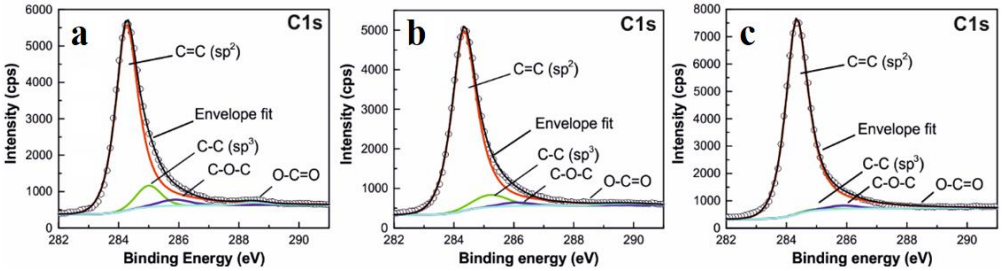

Figure 20. XPS spectra of transferred planar graphene (**a**), VGN grown for 20 min (**b**) and VGN grown for 40 min (**c**) on fused silica substrate. The black circles represent the acquired XPS data, the black line denotes the envelope fit, the red line stands for C=C (sp^2), the green line depicts C–C (sp^3), the blue line indicates C–O–C, the cyan line shows O–C=O [A2]

Table 2. Calculated surface atomic concentrations from XPS analysis for planar graphene and VGN films on fused silica substrates

Peak name	Transferred	VGN 20 min	VGN 40 min
	Atomic %	Atomic %	Atomic %
O 1s	20.92	23.91	11.48
C 1s	72.45	57.42	78.62
Si 2p	6.63	18.67	9.9
C=C (sp^2)	87	91	97

From the deconvoluted carbon C 1s spectra (**Figure 20 a**, **b**, **c**), one can see that the asymmetric peak at 284.3 eV dominates in all spectra. This peak is attributed to graphitic C=C carbon bonds (sp^2 configuration) [159–161], which means that the majority of the carbon atoms are arranged into a honeycomb lattice. The binding energy of low intensity peaks at 285 eV, 286 eV and 288.5 eV are similar to those reported in the literature [159–161] for C–C (sp^3), C–O–C and O=C–O bonds, respectively. The bonds including oxygen could originate from atmospheric contaminants [161]. The two former peaks showed almost negligible intensity for both VGN samples (**Figure 20 a**, **b**, **c**), and they are more noticeable for planar graphene as it previously underwent a transfer process which usually leads to additional sources of impurities along with mechanical damage. The defect structure arising from the sp^3 bonded carbon structure is confirmed by Raman scattering spectroscopy results and is discussed further in the thesis. Moreover, in terms of VGN, XPS C 1s spectrum of a sample grown for 40 min (**Figure 20 c**) represents a relatively more intense peak designating an sp^2 bonded graphitic structure and a less intense peak denoting sp^3 bonding compared to the spectrum of VGN grown for 20 min, which specifies the presence of higher areal density of ordered graphitic VGN over the defected nanographite base film as seen in the morphology measurements results (**Figure 20 c**). The XPS spectra of planar graphene show relatively clear C–C (sp^3), C–O–C and O=C–O bonds. Similar XPS spectra representing such bonds and fluorescence spectra were also obtained by other researchers for graphene featuring a bandgap [130]. This indicates that planar graphene might have a bandgap too. The measurements of fluorescence of graphene samples presented in this thesis prove that planar graphene has more defects compared to vertical graphene nanosheets in VGN 20 or 40 min samples (**Figure 29**). The XPS spectrum of VGN 40 min presents the closest results to the pristine graphene spectra [162]. This signifies that the XPS data were measured mostly from the vertical graphene nanowalls, as there is no meaningful amount of sp^3 bonds that the nanographitic layer should contain (**Figure 20 c**) [53]. VGN 20 min yielded some sp^3 signal in the XPS spectra apparently because of a lower amount of VGN in comparison to the VGN 40 min sample (**Figure 20 b**).

4.1.4. Raman scattering spectroscopy analysis

In this section, the defects of the graphene samples were studied when the different types and amount of defects were formed during the synthesis and transfer processes. The typical Raman spectra of transferred graphene as well as graphene

directly deposited on fused silica substrates are presented in **Figure 21**. It is clearly seen that there are significant differences in the band positions, intensities and band shapes as listed in **Table 3**.

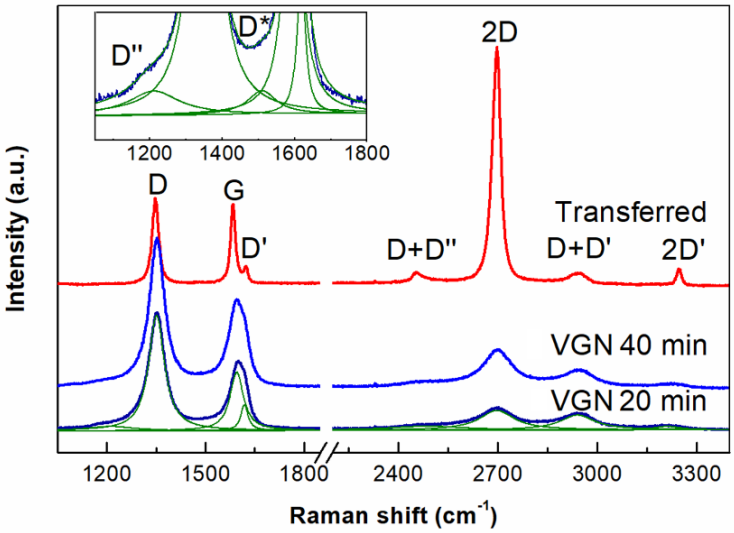

Figure 21. Raman spectra of planar graphene transferred onto fused silica substrate (Transferred) and vertical graphene nanosheets (VGN) directly grown on fused silica for 20 (VGN 20 min) and 40 min (VGN 40 min) by MW PECVD. The inset is the extended region of VGN grown for 20 min and its deconvolution with Lorentzian line shape [A2]

Table 3. Parameters of Raman spectra of transferred graphene and directly grown VGN for 20 and 40 min on fused silica [A2]

	Transferred (planar)	**VGN 40 min**	**VGN 20 min**
Pos_D (cm^{-1})	1347.9	1352.5	1351.7
$FWHM_D$ (cm^{-1})	22.9	55.2	58.0
Pos_G (cm^{-1})	1584.0	1591.6	1595.4
$FWHM_G$ (cm^{-1})	19.0	51.6	49.3
Pos_{2D} (cm^{-1})	2696.2	2699.3	2696.9
$FWHM_{2D}$ (cm^{-1})	29.1	108.0	128.2
I_D/I_G	1.13	1.92	1.97
$I_D/I_{D'}$	6.69	4.38	4.43

The spectra consist of two clearly apparent bands – G (~1590 cm^{-1}) (Pos_G) and 2D (~2700 cm^{-1}) (Pos_{2D}) which confirm the graphitic structure. Furthermore, all the Raman spectra comprise one-phonon second-order Raman scattering processes – D, D′ and D″ bands, and two-phonon second-order lattice vibrational processes, such as 2D′, D+D′ and D+D″ bands, which are activated by defects and disorder due to a high density of edges, grain boundaries, sp^3 hybridised carbon atoms, point defects, ion-induced defects, and are strongly dispersive with excitation energy [101,163]. As it can be seen in the inset of **Figure 21**, there is a very weak mode underlying the upshifted valley between the D and G bands of VGN samples. This peak at about

1500 cm^{-1} is assigned as D* band, which is attributed to the presence of interstitial or out-of-plane defects, pentagon-heptagon, fullerene-like structures [156]. The other D″ band at about 1200 cm^{-1} could arise due to the existence of a large number of edge states, the bond stretching mode of sp^3 hydrogenated carbon and pentagon rings. Such defects come from a highly defective interfacial NG base layer [53,156].

The obtained parameters of Raman spectra demonstrate structural differences of the transferred planar graphene and directly grown VGN on fused silica as given in **Table 3**. Considering the VGN samples, the intensity of the D, G, and 2D bands increases, and the full width at half maximum (FWHM) of the D and 2D bands decreases with the growth time. Also, the intensity ratio I_{2D}/I_G increases in terms of the growth time. What is more, along with the growth time, the G band position (Pos_G) shifts from 1595.4 to 1591.6 cm^{-1} for the VGN specifying the enhancement in crystallinity. On the other hand, the FWHM of D, G and 2D bands of VGN is higher than that for planar graphene, thus indicating a more disordered structure. Meanwhile, the Pos_G of planar graphene is even more downshifted, and it equals 1584.0 cm^{-1}. Such a variation in the G band position could be due to the different levels of strain in VGN directly grown on a fused silica substrate and the transferred graphene, which could be induced by the lattice mismatch between the substrate and the interfacial NG base layer or the presence of defects [157]. Compared to the Raman spectrum of the transferred graphene, the G and D′ bands almost overlap for VGN, which also indicates a higher amount of defects (**Figure 21**) [48].

The Raman scattering technique is capable of determining the layer thickness at the atomic layer resolution for graphene layer thicknesses of less than four layers [31]. In this case, the intensity ratio of 2D and G bands I_{2D}/I_G of the planar graphene Raman spectrum is equal to 3.19, which indicates one layer of carbon atoms (**Figure 21**, **Table 3**). Moreover, the Raman scattering measurements of different areas (not shown here) also suggest a notably lower I_{2D}/I_G ratio (~1) and show a Raman 2D band with a single Lorentzian profile (as seen in **Figure 21**), just as in the monolayer graphene but with a larger linewidth (for single-layer graphene, FWHM is found to equal ~24 cm^{-1} [31]). This demonstrates that planar graphene consists of small regions of multilayers with the rotationally random stacking with respect to one another. This specifies the digression from the ordered stacking, and, consequently, the corresponding electronic coupling between graphene layers does not take place in all parts of the film. This is a peculiarity for graphene films prepared by the CVD method [31].

The Raman mapping data of 19 μm × 19 μm area of planar graphene have confirmed the thickness analysis and shown that the thickness of the graphene layer is not homogeneous over the scanned area (**Figure 22**). In the colour bar of **Figure 22**, the aspect ratio of I_{2D}/I_G is shown. One can see that it varies from 3 till below 0.5. In the case of an aspect ratio of 3, it is monolayer graphene, while, in the case of an aspect ratio below 2, it is multilayer graphene. The film consists of domains of graphene monolayers and multilayer graphene.

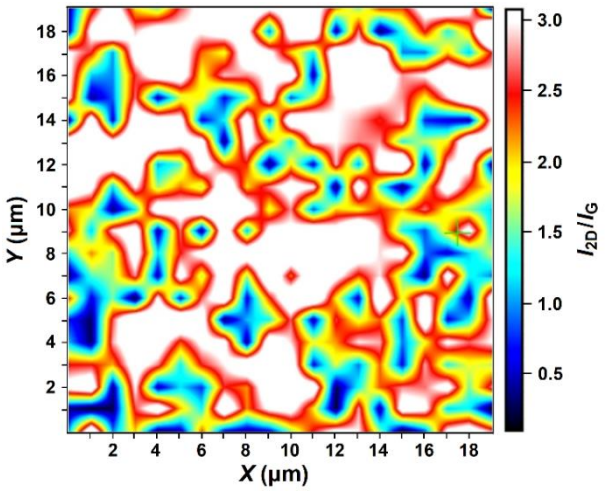

Figure 22. Analysis of the ratio between 2D and G peaks (I_{2D}/I_G) in Raman spectra of planar graphene

Raman scattering spectroscopy allows us to investigate the nature of defects and its quantification on graphene. The intensity ratio I_D/I_G serves as a measure of defects in a disordered graphitic material. This ratio of planar graphene is notably smaller than those of VGN samples (**Table 3**). The intensity of defect bands D and D′ depends not only on the number of defects but also on their kind [53]. The $I_D/I_{D'}$ ratio is found to be 4.4 and 6.7 for VGN and planar graphene, respectively (**Table 3**). The ratios indicate the existence of boundary-like defects for VGN directly grown on fused silica and vacancy-like defects for the transferred planar graphene [164].

It is known that there are two typical sets of defects in graphene: point and line defects [48]. Point defects are characterised by the average distance between the nearest defects (L_D) or by the defect density ($\sigma=1/L_D^2$), whereas line defects are characterised by their average crystallite size (L_a) or by the crystallite area (L_a^2) [48].

The calculation of the density of line defects is still fairly complicated at the moment, while the point defect density can be estimated from I_D/I_G [48,95,165,166]. Sometimes, instead of I_D/I_G, it is more reliable to use $(A_D/A_G)E_L^4$ [48,95,165], where E_L is the excitation energy, and A_D, A_G denote the area of the D and G peaks. However, for a large disorder, it is far more informative to decouple the information from FWHM of the G peak. Because of the quantum confinement effect, the FWHM of the G peak increases with the increasing defect density [48,95].

In the case of a low defect density regime ($L_D \geq 10$ nm), L_D can be calculated by using the formula given in Equation 4 [53,95,167]:

$$L_D^2(nm^2) = (1.8 \pm 0.5) \times 10^{-9} \lambda_L^4 \left(\frac{I_D}{I_G}\right)^{-1}; \quad \text{(Eq. 4)}$$

while the defect density (n_D) can be calculated as:

$$n_D(cm^{-2}) = \frac{(1.8 \pm 0.5) \times 10^{22}}{\lambda_L^4} \left(\frac{I_D}{I_G}\right); \quad \text{(Eq. 5)}$$

where I_D and I_G represent Raman spectra D and G peak intensities, λ_L is the excitation laser wavelength; in this particular case, it is 532 nm. The I_D/I_G values

used in the calculations are taken from **Table 3**, and the calculation results are shown in **Table 4.**

According to the computation results, the average distance between point defects is the largest (or the density of point defects is the lowest) for planar graphene as XPS and TAS measurements show different results.

The crystalline sizes (L_a) of VGN along with the nanographitic layer can be evaluated by using the Tuinstra-Koenig relation [156,168,169]:

$$L_a = C(\lambda)(\frac{I_D}{I_G})^{-1}; \quad \text{(Eq. 6)}$$

where C (λ = 514.5 nm) = 4.4 nm. In these measurements, the 532 nm wavelength laser light was employed for excitation (that is relatively close to 514.5 nm). In order to note this small difference, in these notations, the sign '~' in front of L_a was used. As linear defects are characterised by L_a, this value was inserted in **Table 4** as well. The largest estimated L_a was found for planar graphene.

Table 4. Density of point defects: average distance between nearest defects (L_D), L_D^2, defect density (n_D) and average crystallite size (L_a) for two types of graphene [A2]

Graphene	L_D **(nm)**	L_D^2 **(nm^2)**	n_D **(cm^{-2})**	L_a **(nm)**
Planar	11.30±5.90	127.60±35.40	78370±21770	~3.89
VGN 40 min	8.66±4.57	75.10±20.86	133156±36990	~2.29
VGN 20 min	8.56±4.51	73.19±20.33	136612±37950	~2.23

Despite the fact that the calculated defect density defined from the Raman scattering data was found to be lower in planar graphene in comparison to VGN, one should still keep in mind that VGN films have lots of edges and a defected NG base, which increases the intensity of the D band leading to a larger calculated defect density. The XPS and TAS measurements support this idea.

It was found that there are significant blue shifts in the Raman scattering spectra for VGN 20 min and VGN 40 min samples as compared to pristine graphene (**Table 5**) [170,171]. It is known that the shifts of Raman scattering spectra can appear due to doping or strain effects. As the VGN samples were not doped during the deposition (and this was confirmed by XPS measurements), the strain influence on the Raman spectra is more reliable. According to the blue shift of the Raman scattering spectra of VGN in comparison to pristine graphene, some compressive strains in VGN are present (**Table 5**) [172,173]. One can assume that compressive strains are one of the factors defining the vertical configuration of graphene nanosheets.

Table 5. Positions of G and 2D bands in Raman scattering spectra of our graphene samples and pristine graphene

Graphene	**Pos$_G$ (cm^{-1})**	**Pos$_{2D}$ (cm^{-1})**
Pristine graphene	1580 [171]	2680 [171]
Planar graphene	1584	2696
VGN 40 min	1592	2699
VGN 20 min	1595	2697

A small blue shift in the Raman spectra was detected for planar graphene as well, and it is believed that some p-type doping is a more reliable explanation of this blue shift [174], while the compressive strains should not be the main reason. It is known that such metals as Pt, Au, Fe, Cu cause n-type doping [175–178], and oxygen can give rise to p-doping [171]. It is assumed that the detected oxygen (**Figure 20 a**) can be the reason for p-doping and for the Raman spectrum blue shift in planar graphene. It should be noted that the amount of oxygen in the VGN samples looks much lower (**Figure 20 b** and **Figure 20 c**) in comparison to planar graphene (**Figure 20 a**); therefore, compressive strains are, most likely, a dominant reason for the blue shift of the Raman scattering spectra in the samples of VGN, although the oxygen influence cannot be eliminated completely.

4.1.5. Electrical properties

A different structure and morphology of graphene leads to different sheet resistances (R_S) (**Figure 23**). The planar graphene layer exhibited R_S of 3.62 kΩ/sq. Due to the structural defects and disorder discussed above, the R_S value is notably higher than that reported in the literature: for the CVD planar graphene films of 3 nm average thickness whose Raman spectra exhibit a low intensity disorder-induced D band ($0.05 < I_D/I_G < 0.3$), the sheet resistances were 770–1000 Ω/sq [179]. What concerns VGN, after 20 min of growth, the film was already electrically conductive with a sheet resistance of 4.79 kΩ/sq, thus verifying the formation of a continuous nanographite layer aligned along the substrate surface with high conductive few-layered vertically standing graphene sheets, which closely matches the research reported in [53]. The R_S of planar graphene is relatively close to VGN probably because of its high amount of defects, which corresponds to the XPS measurements (**Figure 20 a**, **b**, **c**).

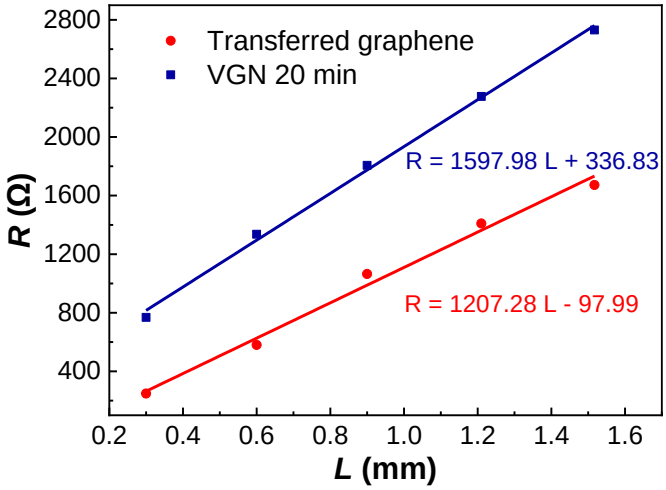

Figure 23. Measured resistance values versus contact spacing (by TLM method) for transferred graphene and VGN 20 min film on fused silica substrates. *R* – measured resistance of the film, *L* – channel length between electrodes

Before starting measurements of the electrical resistance dependences on the temperature of the VGN 20 and 40 min samples, their longitudinal current-voltage characteristics (CVC) were evaluated at temperatures $T \approx 2$ K (inset in **Figure 24 a**) and $T \approx 300$ K (inset in **Figure 24 b**). For both samples, the I–V characteristics were linear, which indicates the ohmic nature of the electrical contacts in use. The higher resistance of VGN 20 min, in comparison with VGN 40 min, is most likely due to the smaller thickness of the conducting nanographite baselayer and to the vertical graphene nanostructures being at the initial stage of growth.

It is worth noting the essential features of the behaviour of the electrical resistance of the samples under study. It turned out that, when stored in air, the resistance of both samples remained nearly unchanged over time. However, an increase in resistance was noticed upon repeated sequential cooling and heating of the samples (thermal cycling) in the temperature range 2–300 K either in gaseous helium, or upon removal of the samples after heating to air atmosphere. In **Figure 24**, the dependences of the resistance R of VGN 20 and 40 min samples on the number of cycles N (four cooling-heating cycles in helium and one helium-air-helium cycle (cycle $N = 3$ in **Figure 24 a**)) are presented. As it can be seen, with the increasing N, a consistent increase in resistance is observed with a tendency to saturation. The thermal cycling has the greatest impact on VGN 20 min, where R increases by more than 20% for $N = 5$ (**Figure 24 a**).

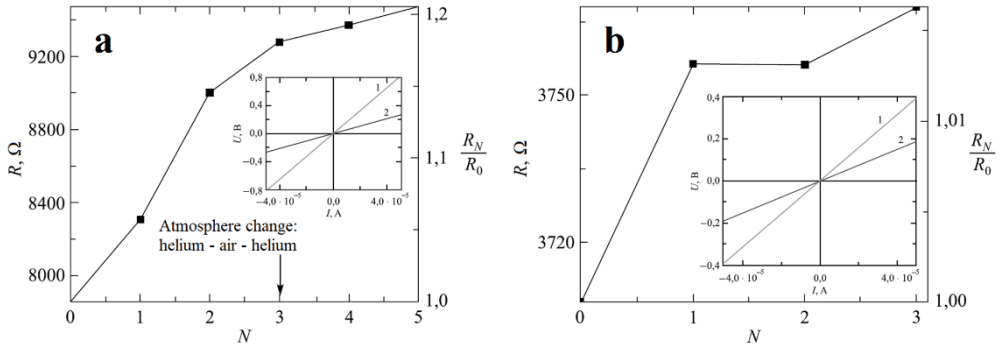

Figure 24. Dependences of electrical resistance R (the left axis) and normalised electrical resistance R_N/R_0 at 300 K (the right axis) for VGN 20 min (**a**) and VGN 40 min (**b**) on the number of thermal cycles N. Thermal cycling corresponds to the cooling-heating process (300 K → 2 K → 300 K), except for the cycle $N = 3$ (**a**) where the atmosphere changed (helium-air-helium) since the sample was taken out into the air (insets: current-voltage characteristics of samples VGN 20 min (1) and VGN 40 min (2) measured at temperatures of 2 K (**a**) and 300 K (**b**)) [A3]

This way of behaviour can be explained by the rearrangement of defects within the samples caused by the peculiarities of their formation. As mentioned above, at the beginning of the MW PECVD process, there is rapid nucleation of highly defective (practically amorphous) nanographite islands [156,157] which grow with an increase in the deposition time and conjoin together. Various types of defects (amorphous carbon, carbon onions and point defects, as well as ring-shaped defects) are formed at the boundaries of the formed grains, which create internal

stresses in the nanographitic (NG) baselayer. This can be indirectly indicated by the reaction of the VGN samples to a change in the atmosphere. Thus, the removal of the sample from helium to air and its return back to gaseous helium (cycle $N = 3$ in **Figure 24 a**) induced an increase in resistance by about 3%. The described behaviour of the $R(N)$ curves and their normalised analogues can also be associated, for example, with the formation of open (dangling) carbon bonds, along which the charge transfer can occur in inert helium. When placed in the air, such bonds are passivated by oxygen and nitrogen. These stresses, apparently, can also lead to discontinuities in the VGN structure.

The role of defects in the sensitivity of electrical resistivity to ambient conditions is supported by the fact that VGN 40 min synthesised with a longer deposition time turned out to be noticeably less sensitive to thermal cycling than VGN 20 min. Thus, in three cooling-heating cycles, the increase in resistance was only 1.6% (**Figure 24 b**), which is possibly because of a decrease in stresses at the grain boundaries of the NG baselayer due to the disappearance of part of defects during the growth of the vertical graphene components, which originates in the most defective NG baselayer zones [53,156,157]. An alternative, yet less probable, explanation may be that VGN 40 min features a thicker NG baselayer, which makes it difficult to form breaks at the cooling stage.

The ideas expressed above are confirmed by the experiments on measuring the temperature dependences of the electrical resistance of VGN 20 min and VGN 40 min for different values of N. **Figure 25**, which shows the curves $R(T)/R_2$ normalised to resistance at temperature $T = 2$ K, specifies the semiconducting character of both samples with a changing temperature. Furthermore, as follows from **Figure 25 a**, the shape of the curves $R(T)/R_2$ progression from 2 K up to 300 K significantly depends on the number of thermal cycles. Thus, upon the first cooling of VGN 20 min, the $R(T)/R_2$ curve exhibits clearly expressed jumps, which, apparently, reflect the defect rearrangement described above and possible discontinuities in the VGN structure. During the fifth cycle of cooling-heating (curve 2), the number of jumps highly decreases, and the curve $R(T)/R_2$ becomes smoother. The disappearance of such jumps with an increasing N in **Figure 25 a** correlates with the saturation of the curve in **Figure 24 a**.

In the case of VGN 40 min, the normalised dependences $R(T)/R_2$ at different N are indistinguishable (they are smaller than the measurement error), which gives evidence to a greater stability of this sample, in comparison with VGN 20 min, to a change in temperature during thermal cycling. In general, the similarity of the $R(T)/R_2$ curves at different N may indicate the retention of the main mechanisms of the conductivity of both samples after thermal cycling.

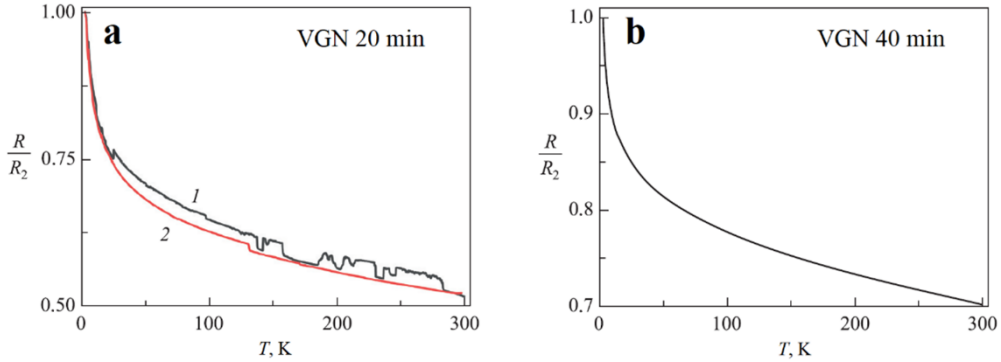

Figure 25. Temperature dependences of the normalised resistance $R(T)/R_2$ (R_2 – resistance at temperature T = 2 K) for VGN 20 min (**a**) and VGN 40 min (**b**). Curve 1 corresponds to the measurement during the first cooling-heating cycle (N = 1); curve 2 corresponds to the measurement during the fifth cooling-heating cycle (N = 5). The curve in (**b**) for VGN 40 min sample corresponds to $0 \leq N \leq 3$ [A3]

The investigation of the magnetoresistivity of VGN 20 min was carried out in more detail. The dependencies of magnetoresistance MR = $[R(B) - R(0)]/R(0)$ on the induction of magnetic field B (**Figure 26**) of the sample VGN 20 min reveal the domination of the negative magnetoresistance (NMR) both at perpendicular (**Figure 26 a**, **b**) and in-plane (**Figure 26 c**, **d**) orientations of magnetic field B with respect to the sample's plane. It is seen that, at T = 2 K, the effect of magnetoresistance is two times higher at perpendicular geometry with respect to the in-plane one (**Figure 26 e**).

It is worth mentioning that, in the in-plane geometry, only NMR is detected, while, at the perpendicular geometry, at higher B values, the positive effect (PMR) is observed as well.

Figure 26 e shows a comparison between the MR effect measured at T = 2 K in the perpendicular and the in-plane orientations of magnetic field B. It is seen that the difference is not only in the values but also in the shape of the MR curves. Such a difference is quite typical for graphene.

The in-plane geometry, when field B_{in} lies in parallel with the sample's surface but perpendicular to the electric field, changes the direction of the Lorentz force as compared to the case of the perpendicular orientation of magnetic field B_{out}. The deviation of the charge carrier's trajectory under the effect of the B_{in} field is directed along the normal to the sample's surface, which is impossible in very thin layers. The thickness of the nanographitic layer in the sample VGN 20 min is probably too small for the Lorentz force to appear.

The observed behaviour of magnetoresistance for the VGN 20 min sample is relatively similar to that of the single-layered graphene. This indirectly confirms the SEM data evidencing a small amount of the vertical graphene and the domination of the amorphous graphitic layer in the VGN 20 min sample.

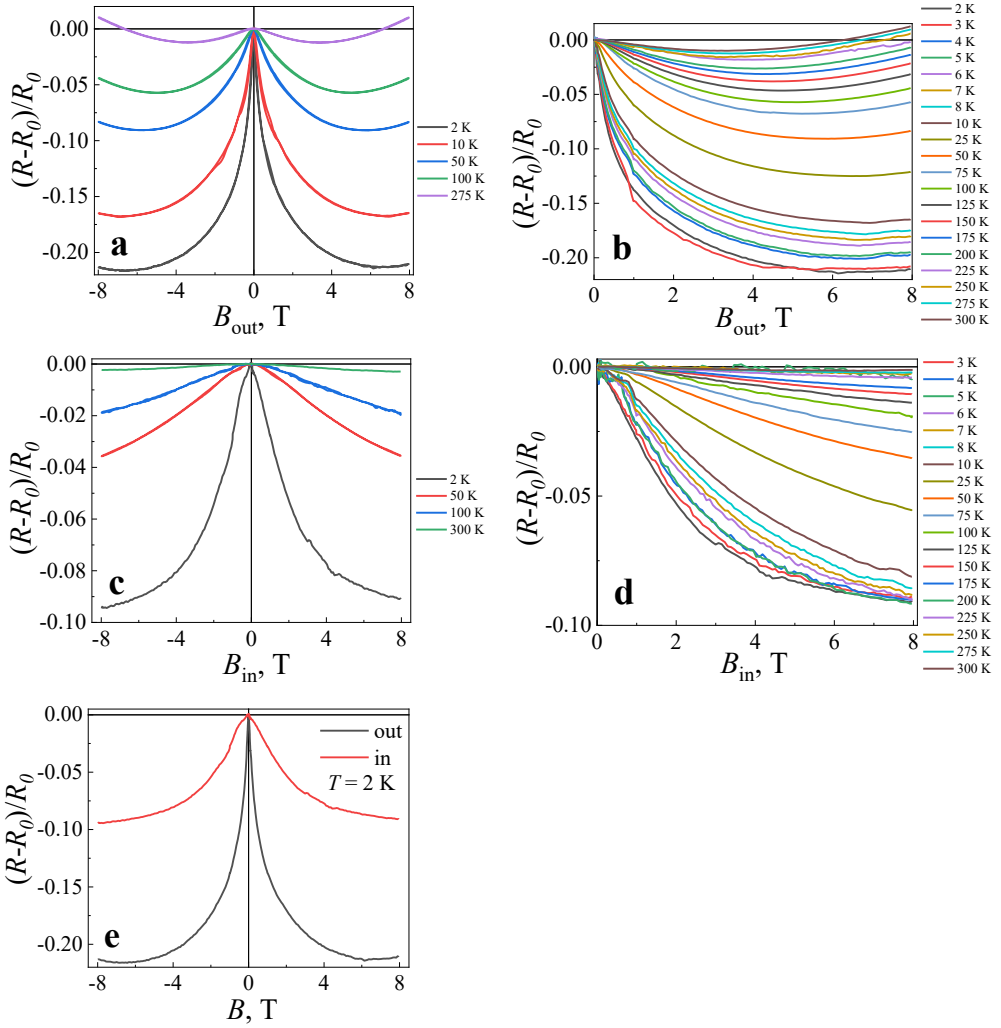

Figure 26. Typical dependencies of MR = [$R(B)$ - $R(0)$]/$R(0)$ on B at perpendicular (**a**) and in-plane orientation (**c**) of the magnetic field with induction B and more specified dependencies (**b** and **d**) in the temperature T range of 2–300 K, respectively, for the sample VNG 20 min. Dependencies of MR on B at perpendicular (the black curve) and in-plane (the red curve) orientation of B with respect to the samples' surface at T = 2 K for the sample VNG 20 min (**e**)

4.1.6. Analysis of optical properties

Figure 27 depicts the steady-state absorption spectra of planar graphene transferred onto fused silica and a bare fused silica substrate (**a**), as well as graphene prepared directly by the MW PECVD method (vertical) thin VGN 20 min and thicker VGN 40 min (**b**). The absorption spectra of graphene transferred onto fused silica (planar) are very broad compared to VGN (**Figure 27 b**). This might indicate the existence of various additional species/defects in planar graphene as compared to VGN. It is also observed that planar graphene absorption is relatively large in terms

of VGN. The domains of graphene multilayers along with unavoidable remaining contaminations after the transfer process increase the intensity of the absorption of planar graphene, and therefore it is larger than the high quality commercial graphene and is compatible with or even larger than VGN.

The absorption peak of planar graphene is at about 245 nm; it is shifted to shorter wavelengths in terms of the peak of VGNs samples, which is at 270 nm. Despite having a clear absorption peak of graphene, VGN samples (especially VGN 40 min) are denoted by strong absorption at the spectral area within the 400–800 nm range, which is relatively much stronger than planar graphene. Here, the influence of the NG base layer in VGN samples might underlie in comparison to planar graphene.

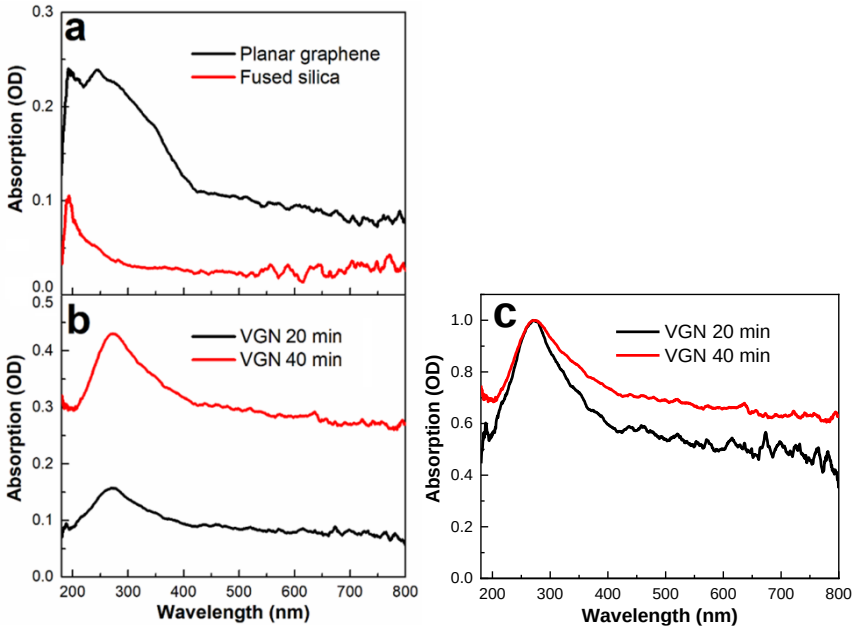

Figure 27. Steady-state absorption spectra of planar graphene transferred onto fused silica and bare fused silica substrate (**a**), and graphene prepared directly by MW PECVD method: (vertical) thin VGN 20 min and thicker VGN 40 min (**b**), and their normalised steady-state absorption spectra (**c**) [A2]

The absorption peak of graphene prepared directly by MW PECVD (vertical graphene nanosheets) can be associated with the *M*-point in the graphene band structure which is characterised by the appearance of the so-called Fano resonance peaking at around 270 nm (**Figure 27 b**) [37]. Fano resonance occurs when a discrete state couples to a continuum of states [180]. The *M*-point corresponds to interband transition at the saddle-point (the *M*-point) in the Brillouin zone of graphene [10]. It is known that an increase of the thickness of graphene (the number of layers) causes the redshift of the *M*-point spectral position [37]. The normalised absorption spectra of VGN 20 and 40 min demonstrate a similar peak position in VGN 40 min and VGN 20 min (**Figure 27 c**). Nevertheless, VGN 40 min exhibits relatively more intense absorption in the spectral area of longer wavelengths.

Usually, the absorption peak of high quality planar graphene investigated by other researchers is located at about 270 nm [37]. That is similar to the measured VGN (**Figure 27 b**), but, on the other hand, it has been specified that planar graphene suffers from a high number of defects. These facts are in correspondence with the results of XPS (**Figure 20 a**), but still somewhat contradict the Raman scattering spectroscopy (**Figure 21**) results. As it has already been mentioned, I_D/I_G defined from the Raman scattering spectroscopy spectra is higher for VGN samples than that for planar graphene (**Table 3**). It yields evidence that Raman scattering spectroscopy does not provide enough information for the comparison of defects and disorder in a different type of graphene, i.e., in the planar graphene and VGN samples. Additional materials analysis methods are necessary to clarify the situation. In the present research, transient absorption spectroscopy was used.

4.1.7. Analysis of dynamic optical properties

Fused silica was selected as the substrate for the VGN and planar graphene samples for optical measurements because it only induces negligible artefacts in the transient absorption experiments [35]. Fused silica does not generate the TAS signal under excitation of 350 nm (**Figure 27 b**).

It should be noted that TAS spectra and traces can give information about such processes as electron-electron scattering, electron-optical phonon scattering, and phonon-phonon scattering [37,108]. Unfortunately, the first process is too fast for this setup, while the other two processes can be explored in detail.

It should be noted that TAS spectra of planar graphene are more complex if compared with the ones for VGN. They consist of a positive component at 370–480 nm and a negative component at 550–670 nm during the first 0.5 ps (**Figure 28**). After that time, all TAS spectra become positive. It is visible that the TAS signal decreases below 400 nm – most likely, the signal becomes negative below 370 nm (**Figure 28 a**, **b**, **c**). The positive signal of TAS of planar graphene was associated with additional energy levels created by defects. According to the Raman scattering spectroscopy measurements (ratio of $I_D/I_{D'}$), most of the defects in planar graphene develop because of vacancies (**Figure 21**, **Table 3**). This ratio value was found to be 6.69, and it can be linked to the above mentioned type of defects [53].

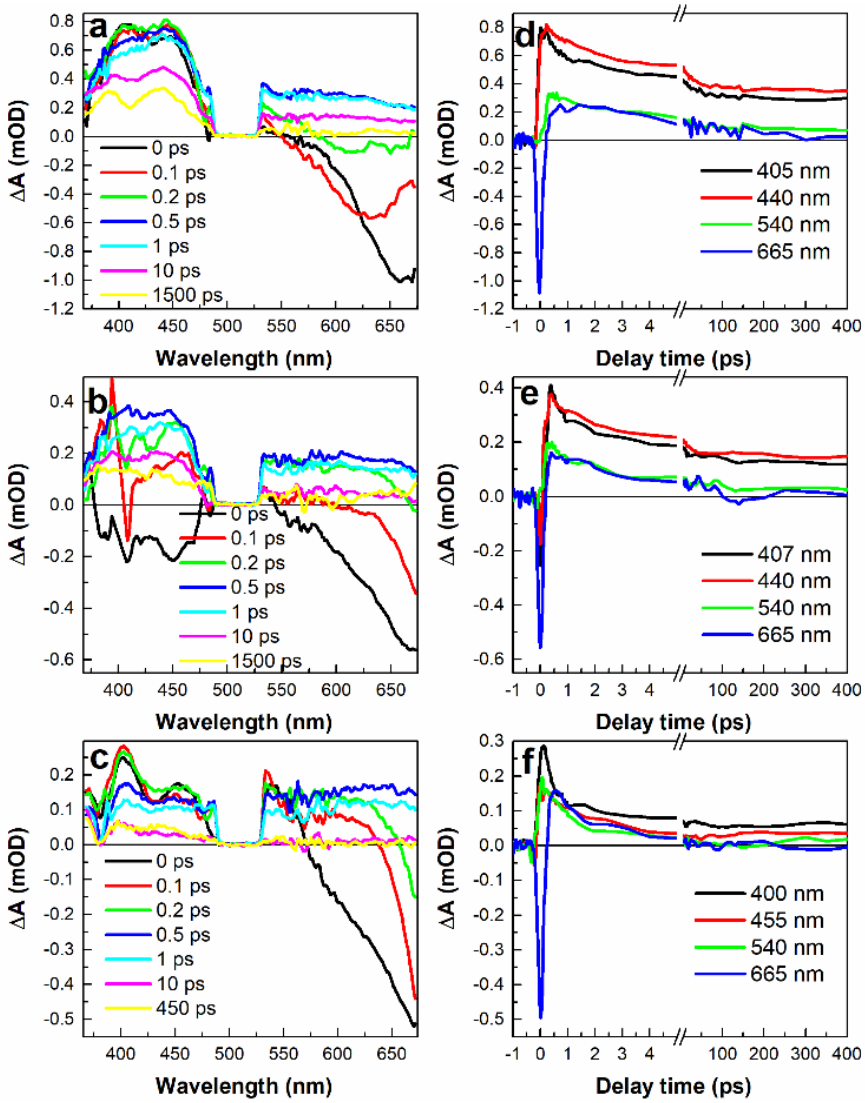

Figure 28. TAS spectra (**a**, **b**, **c**) and traces (**d**, **e**, **f**) of graphene transferred onto fused silica. Graphene was excited at 350 (**a**, **d**), 400 (**b**, **e**) and 700 nm (**c**, **f**). Excitation intensity was 24 μJ/cm^2, 19 μJ/cm^2 and 54 μJ/cm^2. (TAS data in spectral region 470–540 nm do not have scientific accuracy due to the probe beam quality at this region) [A2]

In the studies of graphene employing the TAS method conducted by other researchers, in many cases, no positive TAS signal was recorded at all during the measurements of high quality graphene [37,181]. According to the Raman scattering spectroscopy and XPS measurements, planar graphene contains some defects (**Figure 20 a**, **Figure 21**); therefore, one can attribute the registered TAS positive signal to the defects. The lattice heating effect [181] should probably be excluded from the factors contributing to the positive signal as it was not clearly observed in high quality graphene, either [37].

A comparison of the normalized TAS spectra of planar graphene recorded under excitations of 350, 400 and 700 nm at a delay time of 0 ps is presented in **Figure 30 a**. The peak maximum of the negative signal part of TAS normalised to one for TAS spectra is presented so that to illustrate the differences more clearly. This kind of normalisation allows us to attribute the negative TAS signal to the pristine graphene excited state relaxation (bleaching because of the Pauli blocking principle) [35], while a positive TAS signal can be attributed to the defects.

The results indicate that the relatively largest positive value in the TAS signal is recorded during excitation with the wavelength of 350 nm, while the smallest one is observed during excitation with the 700 nm wavelength. This fact reveals that the defects exert a greater influence on the graphene relaxation dynamics when graphene is being excited at higher power/shorter wavelength laser pulses (**Figure 30 a**). According to the figure, in planar graphene, there is a higher density of deep energy levels as compared with the shallow ones. This idea is supported by the optical fluorescence measurements, where the fluorescence signal was found to be the strongest in the region of short wavelengths (**Figure 29**).

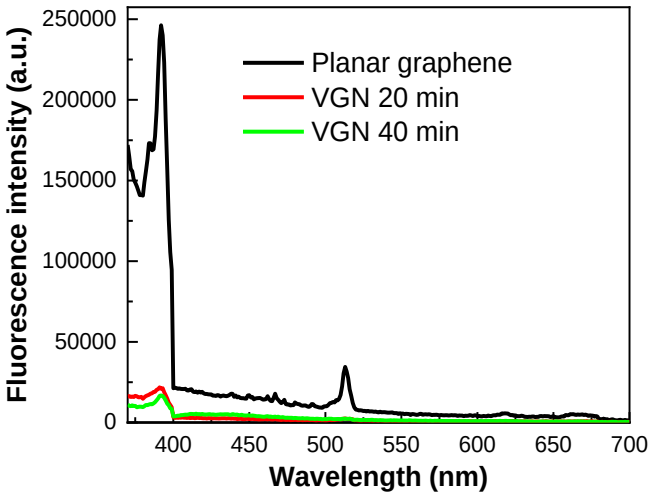

Figure 29. Fluorescence spectra of graphene transferred onto fused silica (planar graphene) and vertical graphene nanosheets (VGN) grown for 20 and 40 min. Excitation at 350 nm with Xenon lamp

Comparing the normalised TAS data for the negative signal peak for planar graphene (**Figure 30 a**) with the normalised TAS spectra at a delay time of 0 ps of VGN 40 min (**Figure 30 b**), one can see that for VGN 40 min TAS spectra do not depend on the excitation wavelength. At the same time, the samples of planar graphene and VGN 40 min have a different structure and structural defects causing differences in TAS dynamics and their dependence on the excitation wavelength. It seems that the edges and boundaries in both graphene layers do not influence the TAS spectra as much as vacancies (**Figure 30 a**, **b**).

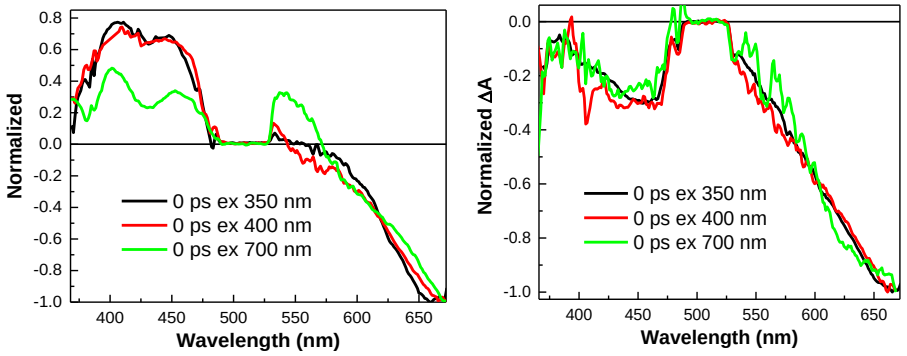

Figure 30. TAS spectra of graphene transferred onto fused silica (**a**) and TAS spectra of VGN 40 min (**b**) at a delay time of 0 ps under excitations at 350, 400 and 700 nm normalised at a negative peak

Analysis of the relaxation dynamics of planar graphene suggests that the long lasting positive TAS signal can be ascribed to the defects of graphene (**Figure 28**, **Figure 31**, **Table 6)**, i.e., the excited state relaxation might be attributed to the energy transfer between the energy states that appear because of the defects. Surprisingly, such a process is not clearly observed in VGN. One can conclude that graphene nanowalls in VGN 20 and 40 min samples are of a much better quality, and/or its defects do not influence the formation of the bandgap. The XPS results also show that VGN can be considered as better quality graphene than planar graphene (**Figure 20 a**, **b**, **c**, **Table 2**) in terms of defects.

The TAS traces depicted in **Figure 31** have been fitted by the exponential decay function. In some cases, the traces were best fitted (R^2 close to 1) with two or one decay exponents. The most reliable fit data are shown in **Table 6**. The fits of traces were analysed at around 400, 440 and 665 nm under excitation of 350, 400 and 700 nm (same like in the case of VGN). The traces at 400 and 440 nm yield positive TAS values, while the trace at 650 nm has a negative value. The negative TAS signal can be attributed to the pristine graphene signal, and it has a similar physical meaning to those of VGN 20 min and VGN 40 min. This negative signal decay was fitted with one exponential function till 0.3 ps because it changed into a positive TAS signal after this decay. Unfortunately, the relaxation of the positive signal of planar graphene (**Figure 31 c**) was too noisy to receive reliable clear results and the corresponding dependencies.

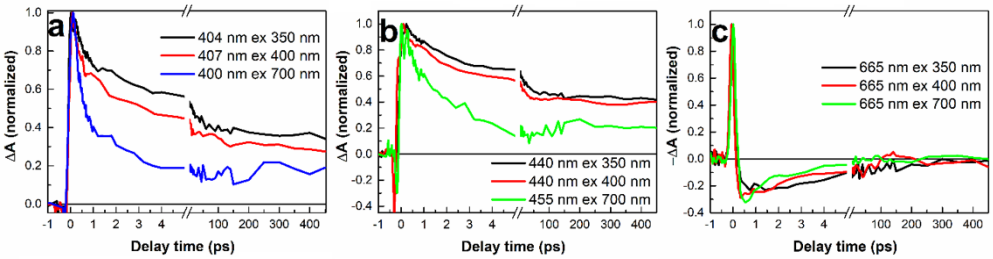

Figure 31. TAS traces of graphene transferred onto fused silica at 400 (**a**), 440 (**b**) and 665 nm (**c**) under excitation at 350, 400 and 700 nm (different photon energy) [A2]

Table 6. TAS relaxation decay times (τ) of planar graphene measured at a probe wavelength of 400–407, 440–455, 665 nm with pump wavelengths of 350, 400 and 700 nm. Traces were fitted with the biexponential or exponential decay function [A2]

TAS traces/ex	τ_1 (ps)	A_1	τ_2 (ps)	A_2
404 nm ex 350 nm	0.82±0.06	0.42±0.02	24.4±2.8	0.24±0.01
407 nm ex 400 nm	0.50±0.05	0.46±0.02	9.4±1.1	0.27±0.02
400 nm ex 700 nm	0.30±0.03	0.86±0.03	2.3±0.4	0.31±0.04
440 nm ex 350 nm	1.95±0.11	0.40±0.01	58.7±5.8	0.20±0.01
440 nm ex 400 nm	1.86±0.13	0.43±0.01	52.8±9.1	0.16±0.01
455 nm ex 700 nm	1.64±0.09	0.77±0.02	-	-
665 nm ex 350 nm	0.15±0.01	1.09±0.02	-	-
665 nm ex 400 nm	0.15±0.01	1.11±0.04	-	-
665 nm ex 700 nm	0.18±0.01	1.72±0.04	-	-

One can also observe that the relaxation dynamics of the positive signal (traces 400 and 440 nm) is far more complex than for the negative one (**Table 6**). The relaxation of the positive signal is the slowest under excitation at a short wavelength (350 nm) and the fastest under excitation of a long wavelength (700 nm) (**Table 6**). Apparently, it is because of the different energy levels of defects that were excited with laser pulses of a different wavelength. It seems that the relaxation dynamics throughout the defects with higher energy levels is slower.

The samples of VGN 20 min and VGN 40 min were excited at 350, 400 and 700 nm, thereby enabling studies of photon energy influence on the excited state relaxation dynamics in graphene. In order to evaluate the relaxation times, the TAS traces were fitted by the exponential decay function. The traces were fitted at probe wavelengths of 420, 460, 600, 665 nm. The TAS results are shown in **Figure 32**, **Figure 33** and **Table 7**. It is evident that different excitation wavelengths cause different relaxation times. The higher is the photon energy, the longer is the relaxation time of the excited states (**Table 7**) for VGN 40 min, while the sample VGN 20 min does not show any clear dependence on the excitation wavelength (**Table 7**). This different behaviour probably stems from the high signal/noise ratio for VGN 20 min. VGN shows a TAS signal that is similar to the one for high quality planar graphene, thus indicating that vertical graphene nanosheets with the nanographitic layer have a small number of defects and are denoted by a relatively high quality graphene structure [37]. This also corresponds to the XPS results and the detailed analysis of steady-state absorption. On the other hand, the analysis of D, G and 2D peaks in the Raman scattering spectra (**Figure 21**) shows a comparatively low quality of graphene as well as abundant defects. This fact indicates that Raman scattering spectroscopy, commonly known for being the best technique used so far for the graphene quality evaluation [30], according to presented results, is not sufficient for the detailed graphene quality estimation in the case of VGN configuration. Due to their structure, VGN films have many more boundaries and edges in comparison to planar graphene, which could increase the D band

dramatically. Complete characterisation of such graphene layers should include optical methods, such as TAS, or other measurements, like XPS.

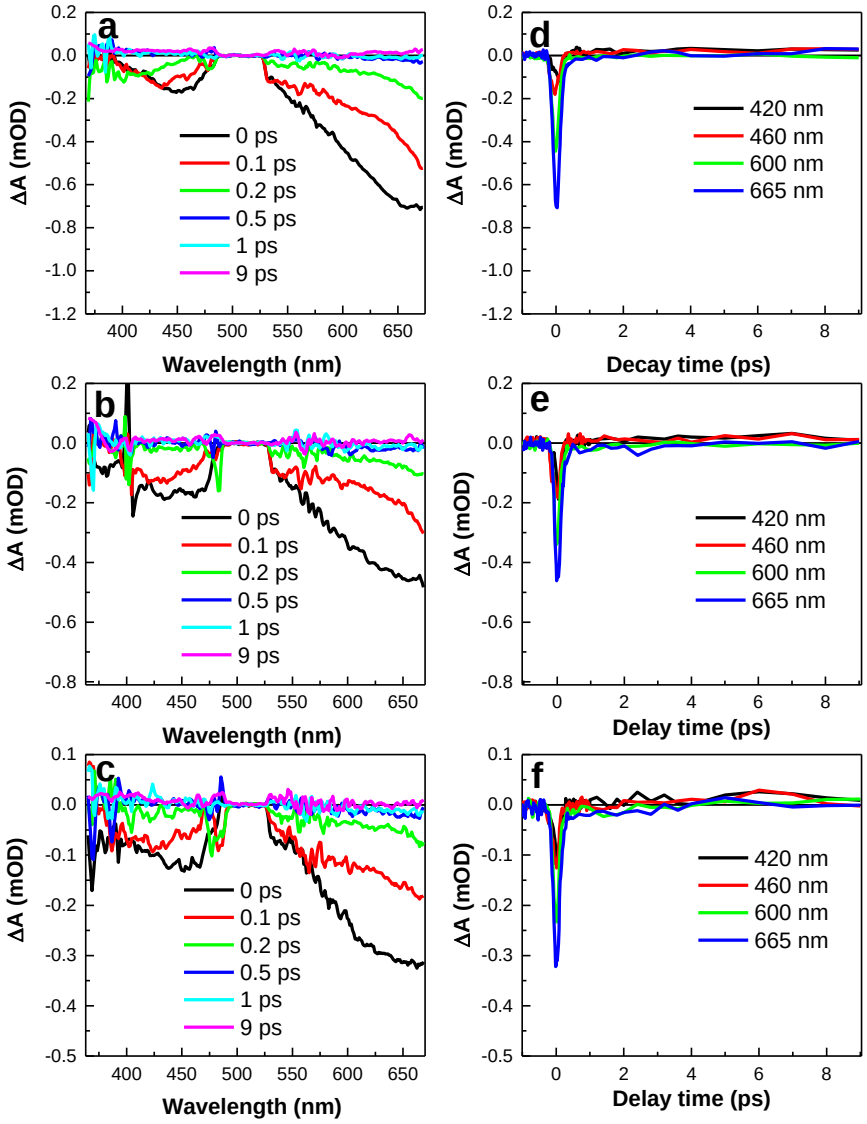

Figure 32. TAS spectra (**a**, **b**, **c**) and traces (**d**, **e**, **f**) of vertical graphene sheets prepared directly on fused silica (VGN 20 min). Graphene was excited at 350 (**a**, **d**), 400 (**b**, **e**) and 700 nm (**c**, **f**). The excitation intensity was 23 μJ/cm^2, 13 μJ/cm^2 and 48 μJ/cm^2. (TAS data in the spectral region 470–540 nm do not provide valuable physical meaning due to the probe beam quality in this region)

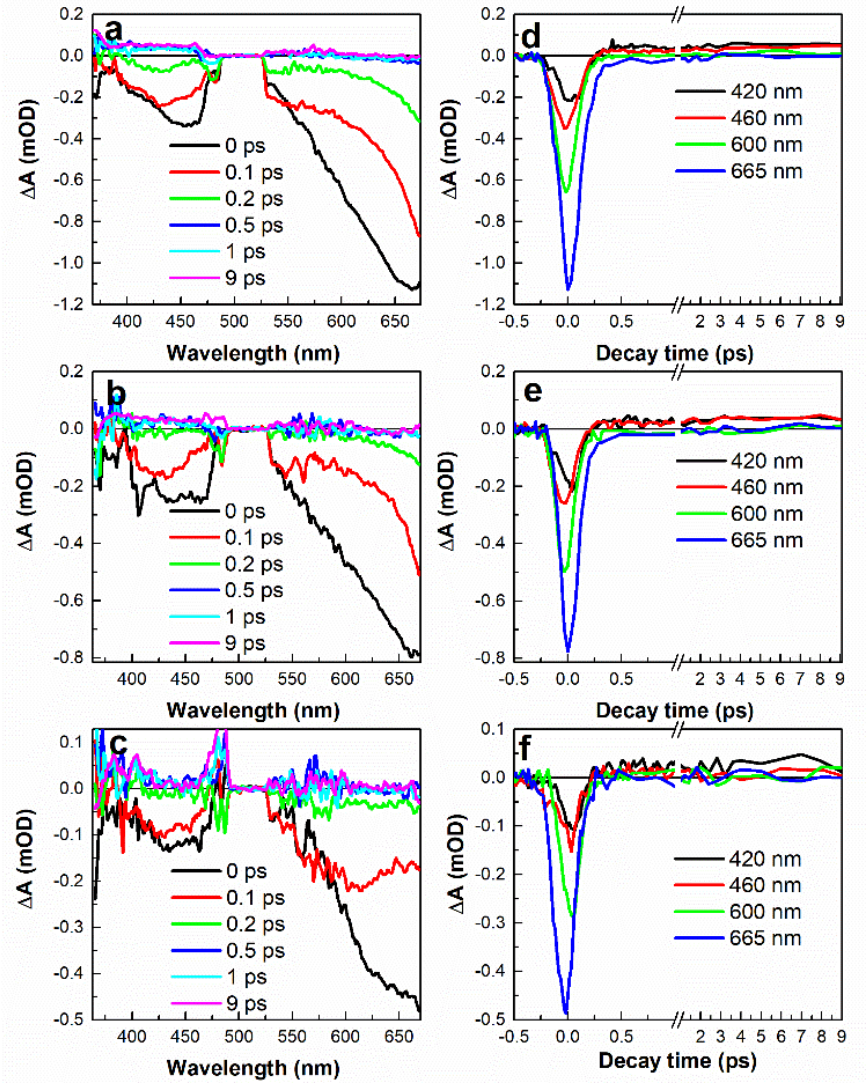

Figure 33. TAS spectra (**a**, **b**, **c**) and traces (**d**, **e**, **f**) of vertical graphene sheets prepared directly on fused silica (VGN 40 min). Graphene was excited at 350 (**a**, **d**), 400 (**b**, **e**) and 700 nm (**c**, **f**). The excitation intensity was 23 μJ/cm^2, 13 μJ/cm^2 and 48 μJ/cm^2. (TAS data in the spectral region 470–540 nm do not provide valuable physical meaning due to the probe beam quality in this region) [A2]

It is worth noting that, in the measured samples, the TAS relaxation for VGN 20 min and VGN 40 min possessing only one fast component takes place, and no meaningful sign of slower component was observed. Although there is evidence of the formation of a positive long lasting signal, it probably appears due to the defects in graphene that are introduced during direct fabrication by MW PECVD on fused silica. Unfortunately, the intensity of the positive signal is too low to be measured and analysed properly.

The decay times defined and given in **Table 7** can be attributed to the electron-phonon coupling process [37,108]. Apparently, phonon-phonon scattering is a highly inefficient process; therefore, it cannot be observed in the TAS relaxation traces of VGN samples, while the electron-electron scattering process is too fast for the used setup.

Table 7. Ultrafast relaxation decay times (τ) of vertical graphene associated with the electron-phonon scattering process in VGN 20 min and VGN 40 min samples [A2]

Wavelength (nm)	τ (ps)/350 nm	τ (ps)/400 nm	τ (ps)/700nm
VGN 20 min			
420	0.098±0.009	0.098±0.007	0.147±0.011
460	0.150±0.009	0.088±0.005	0.090±0.008
600	0.123±0.005	0.123±0.006	0.095±0.004
665	0.115±0.004	0.147±0.008	0.147±0.008
VGN 40 min			
420	0.149±0.010	0.104±0.006	0.093±0.009
460	0.150±0.008	0.119±0.006	0.082±0.006
600	0.117±0.005	0.105±0.005	0.098±0.006
665	0.139±0.005	0.119±0.005	0.101±0.004

It is known that relaxation at short wavelengths attributed to the electron-phonon coupling process should be faster than that at longer ones [181]. On the other hand, the analysis of defined relaxation times does not demonstrate any clear dependence on the wavelength used for the analysis of the samples VGN 20 min and VGN 40 min.

The TAS spectra of VGN 40 min recorded by using various excitation wavelengths of 350, 400 and 700 nm at a delay time of 0 ps were normalised to 1 according to the negative TAS value. No clear difference in the TAS spectra for the varying excitation wavelengths was observed for VGN 40 min (**Figure 30 b**), contrary to planar graphene (**Figure 30 a**).

One can find as well that the TAS spectra and traces presented in **Figure 32**, **Figure 33** look similar to the ones recorded for relatively high quality planar/pristine graphene as shown in [107,181,182].

The fast rise time in the TAS signal can be attributed to electron-electron scattering (not fitted), while the fast relaxation of VGN taking place during ~0.1 ps can be attributed to electron-phonon coupling (**Figure 32 d**, **e**, **f**, **Table 7**). This result is in good agreement with other outcomes provided in the literature [37,106,107,182–184] (**Table 8**).

One can see that the fast decay of the signal at 665 nm is fairly similar for the samples of graphene transferred onto fused silica and made by the direct MW PECVD method (VGN). This signal can be attributed to the relaxation of the excited state of graphene, and the negative signal appears because of the Pauli blocking principle. In the case of transferred graphene onto fused silica (planar graphene), the new signal 'rises'. This signal is assigned to the energy relaxation due to the additional energy levels that appear because of the defects in graphene. This long-

lasting signal could also mean energy (heat) transfer from graphene to the fused silica substrate because of the surface polar phonon scattering [105].

Table 8. Electron-phonon coupling decay times for various types of graphene registered in this research and by other researchers

Graphene type	**Excitation wavelength (nm)**	**Probe wavelength/energy**	**Decay times of electron-phonon coupling**	**Reference**
Planar graphene	350; 400; 700 nm	665 nm	153; 147; 180 fs	Table 6
VGN 40 min	350; 400; 700 nm	665 nm	139; 119; 101 fs	Table 7
1 layer	400 nm and 800 nm	260−640 nm (1.94−4.77 eV)	160 fs and 4 ps	[37]
8 layers	350 nm	440−590 nm (2.1 and 2.8 eV)	180 and 90 fs	[183]
1 layer	800 nm (1.55 eV)	475 nm (2.6 eV) 750 nm (1.65 eV)	70 and 230 fs 270 and 2030 fs	[182]
A few layers	350 nm 680 nm	618 nm (2 eV) 515 nm (2.4 eV) 618 nm (2 eV) 515 nm (2.4 eV)	177 fs 143 fs 153 fs 134 fs	[107]
1 layer	550 nm (2.25 eV)	850–1030 nm (1.2–1.45 eV) 1030–1765 nm (0.7–1.2 eV)	150–170 fs and >1000 fs	[184]
5 layers	1150 nm	1300 nm	260 and 2900 fs	[106]
15 layers	1150 nm	1300 nm	280 and 2600 fs	[106]
37 layers	1150 nm	1300 nm	240 and 2200 fs	[106]
39 layers	1150 nm	1300 nm	240 and 1900 fs	[106]

According to the measured steady-state fluorescence spectra of VGN 20 min, VGN 40 min and planar graphene, planar graphene shows at least a 10-time stronger signal than VGN 20 or 40 min (**Figure 29**). This indicates that planar graphene has more defects than VGN, which leads to more efficient bandgap formation [130]. In accordance with the data of fluorescence measurements, a previous claim can be supported that the positive TAS signal of planar graphene can be attributed to the energy transfer between the additional energy levels created by the defects. The fluorescence of graphene becomes more intense at shorter wavelengths, thus evidencing that there are more defects associated with the high energy levels in graphene (**Figure 29**). This explains the fact that the excitation at a different wavelength (350, 400, 700 nm) leads to a diverse effect on the relaxation dynamics

of the positive TAS signal (**Figure 31**, **Table 6**). It can also explain why there is only the positive TAS signal at shorter wavelengths in planar graphene (**Figure 28**) – this happens because of the higher density of the energy levels created by defects. According to the low fluorescence intensity, VGN 20 and 40 min have a lot less additional energy levels associated with defects in graphene. This explains the fact that the positive TAS signal was not observed in VGN 20 and 40 min (**Figure 32**, **Figure 33**). Finally, the results of fluorescence measurements are in good agreement with the TAS, XPS and steady-state absorption data.

Following the explanations suggested in [35,107], an attempt was made to present graphically the elementary processes taking place during relaxation in pristine graphene (**Figure 34**), and a rough scheme of the potential excited state relaxation (**Figure 35 a**, **b** and **c**, **d**) taking place in the defected planar graphene as well as vertical graphene sheets, with reference to the given results of the steady-state absorption, TAS and fluorescence measurements.

One should keep in mind that the number of layers varies in planar graphene and VGN samples over the surface area; moreover, these layers interact with each other (i.e., electron coupling between separate layers occurs) differently in a diverse type of samples; therefore, a simplified energy level diagram with one valence band (VB) and one conduction band (CB) was used that allowed to qualitatively explain the processes taking place during the TAS analysis. Accordingly, addition of the additional VB and CB energy levels (due to the presence of few-layer graphene) in the model [48,109,185–188] in principle does not change the explanation of the TAS data. For this reason, in the offered simple schemes of ultrafast processes in graphene, the use of more than one VB and CB curve was avoided merely in order not to make them excessively complicated yet still incomplete.

According to **Figure 34**, in pristine graphene, the distribution of hot electrons (grey circles) excited by pump pulse relaxes towards the Dirac (*K*) (shown in **Figure 34**) point by losing energy because of phonon emission. When half of the probe-pulse energy matches the maximum of the electron distribution, absorption is strongly suppressed by Pauli blocking, and the transition is bleached [35,107], which causes the negative TAS signal. During the TAS measurements, the femtosecond pump pulse excites carriers from the valence to the conduction band via dipole-allowed π–π^* transitions around the *K* and *K′* points of the band structure. The photo-excited carriers block the corresponding interband transitions and cause a decrease of absorption due to state filling, which results in the absorption decrease ΔA at early delay times [189].

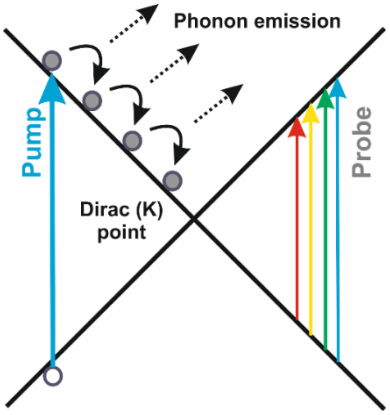

Figure 34. Scheme of ultrafast relaxation dynamics in pristine graphene [A2]

Figure 35 presents ultrafast processes taking place in two types of graphene featuring localised energy states: i.e., planar graphene with many defects (**Figure 35 a**, **b**), and VGN with some defects (**Figure 35 c**, **d**). The figure shows arrows that represent different wavelengths of 350, 400 and 700 nm which were used for the excitation and probe wavelengths that symbolise the white light used for differential absorption measurements of relaxation of the hot electrons in graphene samples. The relaxation of the excited state of pristine graphene appears because of the emission of optical phonons, such as the E_{2g}-mode near the zone centre (the *C*-point) and the A'_1-mode at the zone edge (the *K*-, *K'*-point) (these points correspond to **Figure 35 a**, **c** top dot lines) [190]. Because of the presence of the defects, the bandgap is formed in both cases of planar graphene and VGN 40 min graphene [130]. Although, regarding VGN 40 min, it should not be expressed so clearly (i.e., the value should be lower) as in the case of planar graphene (**Figure 35**). The simplified energy level diagram of graphene (**Figure 35 a**, **c**) is applied without taking into account the complexity of the energy levels typical for two-layer or multilayer graphene that could make the diagram excessively complex [48,185–188,191]. Planar graphene (**Figure 35 a**) features many defects and evidently has a high concentration of localised energy states leading to strong fluorescence. The high concentration of defects in planar graphene is shown as longer and denser lines in comparison to VGN 40 min which represents localised energy levels (**Figure 35 a**, **c**). The transient absorption data for this type of graphene show fast negative signal relaxation that turns into a positive long lasting signal (**Figure 35 b**). This can be associated with an energy transfer from planar graphene to the localised energy states that appeared due to defects. Evidently, a large part of the excited state relaxation dynamics of planar graphene happens because of the relaxation into localised energy states. The strong fluorescence of planar graphene from the localised energy levels supports this idea (**Figure 29**).

What concerns the vertical graphene nanosheets (**Figure 35 c**), despite the phonon emission, relaxation to the localised defects induced energy states also appears, which leads to fluorescence. One can suppose that the concentration of the defects is much lower as the fluorescence is much weaker than that in planar

graphene (**Figure 29**). As a result, the recorded TAS relaxation dynamics in VGN 40 min have only a negative fast relaxation component and no clear positive TAS signal. It should be noted that the TAS of VGN 40 min does not have a slower relaxation component (~2 ps) that is recorded for defect-free graphene [36], which signifies that VGN 40 min has more defects in comparison to pristine graphene.

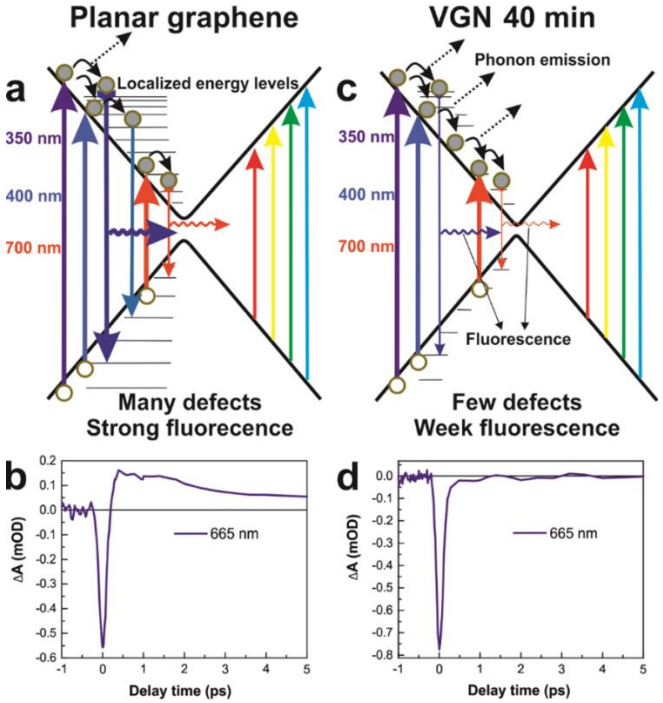

Figure 35. Simplified scheme of ultrafast processes and the TAS signal relaxation trace that represents them at the probe wavelength of 665 nm for planar graphene (**a**, **b**) and VGN 40 min (**c**, **d**). (The simplified energy level diagram of graphene (**Figure 8 a**, **c**) is applied without taking into account the complexity of energy levels typical for two-layer or multilayer graphene) [A2]

In conclusion of this Section 4.1., the complex analysis performed by SEM, AFM, XPS, Raman scattering spectroscopy, TAS and other methods has revealed that the properties of graphene layers formed by the microwave plasma-enhanced chemical vapour deposition on catalytic Cu foil and transferred onto fused silica (planar graphene) and directly deposited vertical graphene nanosheets onto fused silica are relatively different in terms of the morphology, structure, and defects.

It was determined that the main type of defects in vertical graphene nanosheets together with the nanographitic layer were the edges and boundaries, and the defects in planar graphene were mostly developed because of vacancies.

It was demonstrated that transient absorption spectroscopy is an efficient method to inspect the quality of both types of graphene, and that it can complement the Raman scattering spectroscopy method. It was shown that Raman scattering spectroscopy has some limitations in the analysis of the defects and the disorder of graphene in VGN films. The complex analysis of graphene layers, in parallel to the

TAS measurements, demonstrates that the TAS analysis of the excited state dynamics in graphene might lead to the creation of an effective methodology of the evaluation of the quality of graphene.

4.2. Investigation of the properties evolution with deposition time of vertical graphene nanosheets layers

In these studies, vertical graphene nanosheets of various heights and densities were grown onto fused silica substrates by the metal-catalyst-free microwave plasma-enhanced chemical vapour deposition technique at different growth durations from 20 min to 140 min to follow the evolution of VGN properties along with the deposition time. The feedstock of the working gases and the applied MW power was kept constant while focusing solely on the influence of the deposition duration. The growth kinetics of VGN was investigated by using a combination of methods aiming to evaluate the relation between the structure and quality of VGN. TAS, together with other classical techniques, was used for the investigation of carbonaceous nanostructures, including scanning electron microscopy, atomic force microscopy, and Raman scattering spectroscopy. Thus, a number of techniques were applied for the analysis. The majority of the results provided in this Section 4.2. were published in [A1].

4.2.1. Morphology analysis

The surface morphology of VGN films deposited at different plasma processing durations was investigated by using SEM and AFM. Typical SEM images are presented in **Figure 36**. A conspicuous alteration in surface morphology is observed depending on the deposition duration.

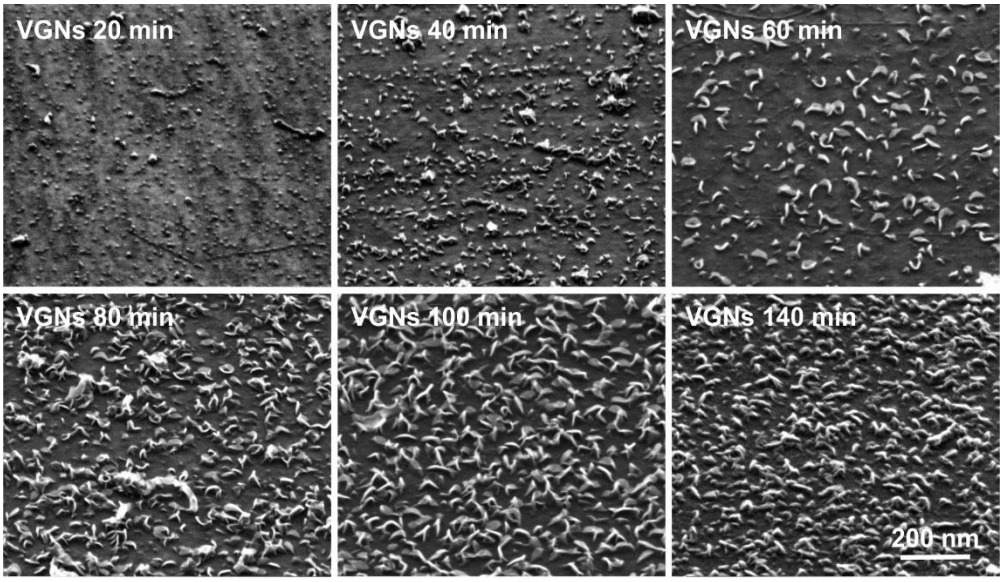

Figure 36. SEM micrographs of VGN deposited under the same pre-processing and deposition conditions (1.2 kW microwave power, CH_4/H_2 gas ratio of 1/3) with only varying deposition duration: 20–140 min. All samples were tilted by 45°, scale bar 200 nm [A1]

After 20 min of deposition (**Figure 36**), the film was composed of small nucleation islands of graphene sheets over the surface of the nanographitic (NG) layer. The lateral length and height of VGN enlarged with the increasing growth time up to 100 min is shown in **Figure 36**. A further increase in the deposition duration did not result in a more prosperous intercalated network of VGN, but, on the contrary, the nanosheets started to grow appreciably smaller (**Figure 36**, VGN 140 min). This shows that the mechanism of VGN formation on insulating fused silica substrates is fairly intricate and sensitive to the synthesis operating parameters and plasma stability [28], and it still needs to be understood. A detailed explanation is provided in Section 4.1.2.

As an outcome, a subsequent increase in the deposition duration consequently increases the density and the height/length of VGN until 100 min (**Figure 36**). Yet, even further deposition for 140 min unexpectedly resulted in less expressed VGN. This might have happened due to plasma instability and conditioned electric field alterations in the sample vicinity through plasma jumps or the ignition of new flashpoints, especially on the corners/edges of the specially used protective enclosure (a metal cover on the sample) [146]. The fluctuations of the confined operating conditions are more probable for long-term depositions [72]. Here, the limitation of the microwave plasma equipment is encountered since the required stability for the depositions can be maintained up to 100 min while applying the specific microwave power, CH_4/H_2 gas mixture proportion, and other operational parameters (see Section 2.1.). Afterwards, the synthesis progress becomes less predictable, and it may result in significant morphology changes.

The quantitative evaluation of the VGN upright dimensions was carried out from the AFM analysis of the 1 μm × 1 μm area presented in **Figure 37**. Unfortunately, owing to the insufficient tip sharpness and its interaction with the dense VGN network, it was not possible to properly characterise the 100 min sample, and it was thus excluded from the further AFM analysis The preliminary measurements indicated that the nanostructures were higher than 75 nm. The arithmetic average roughness (R_a) and the root mean square roughness (R_q) depicted in **Figure 37 f** increase from 28 nm up to 73 nm for the samples VGN 20–80 min along with the deposition duration, yet the level eventually falls to the value of 35 nm for the VGN of 140 min. The trend of the roughness dependence on the deposition durations is almost linear up to 80 min, whereas it sets back for the last sample. The VGN 140 min sample exhibits as dense nanosheets as these of VGN 80 min, and it also has a larger amount of vertical nanostructures than the VGN 60 min sample as can be seen in the SEM (**Figure 36)** and AFM 3D (**Figure 37 c**, **e)** images, although the estimated roughness parameters (R_a = 4.9 nm, R_q = 5.9 nm, an average height of roughness 35 nm) are closer to the ones of VGN 60 min (R_a = 3.9 nm, R_q = 5.2 nm, an average height of roughness 35 nm) (**Figure 37**, **c**, **e**, **f**).

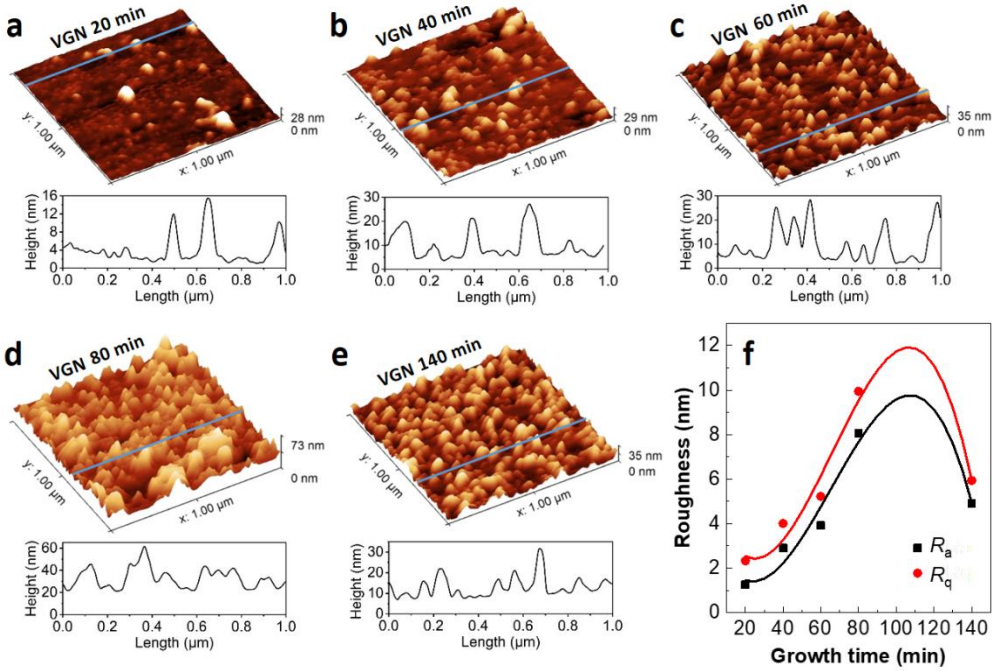

Figure 37. AFM 3D images and selected profiles (indicated by the line) of VGN 20–140 min sample surfaces (**a**–**e**), and the dependence of the calculated roughness parameters on the growth duration of these VGN: R_a – roughness arithmetic average, R_q – root mean square roughness (**f**) [A1]

4.2.2. Structural characterisation

Raman spectroscopy was used for the structural characterisation including the crystalline state, defects, and disorder of VGN films directly deposited onto fused silica substrates. The typical Raman spectra of VGN samples grown at different durations under the same technological operation conditions are depicted in **Figure 38 a**. One can see well-expressed G and 2D bands which are assigned to the graphitic structure. All Raman spectra comprise D, D′, D+D′ and D+D″ bands (**Figure 38 a**) which are attributed to the presence of defects and disorder due to a large quantity of grain boundaries, edges states, the bond stretching mode of sp^3 hybridised carbon atoms, point defects, aromatic rings, fullerene-like structures, ion-induced defects coming from a highly defective interfacial NG base layer [192]. As one can see, these bands are absent in commercial planar (pristine) graphene (**Figure 38 a**).

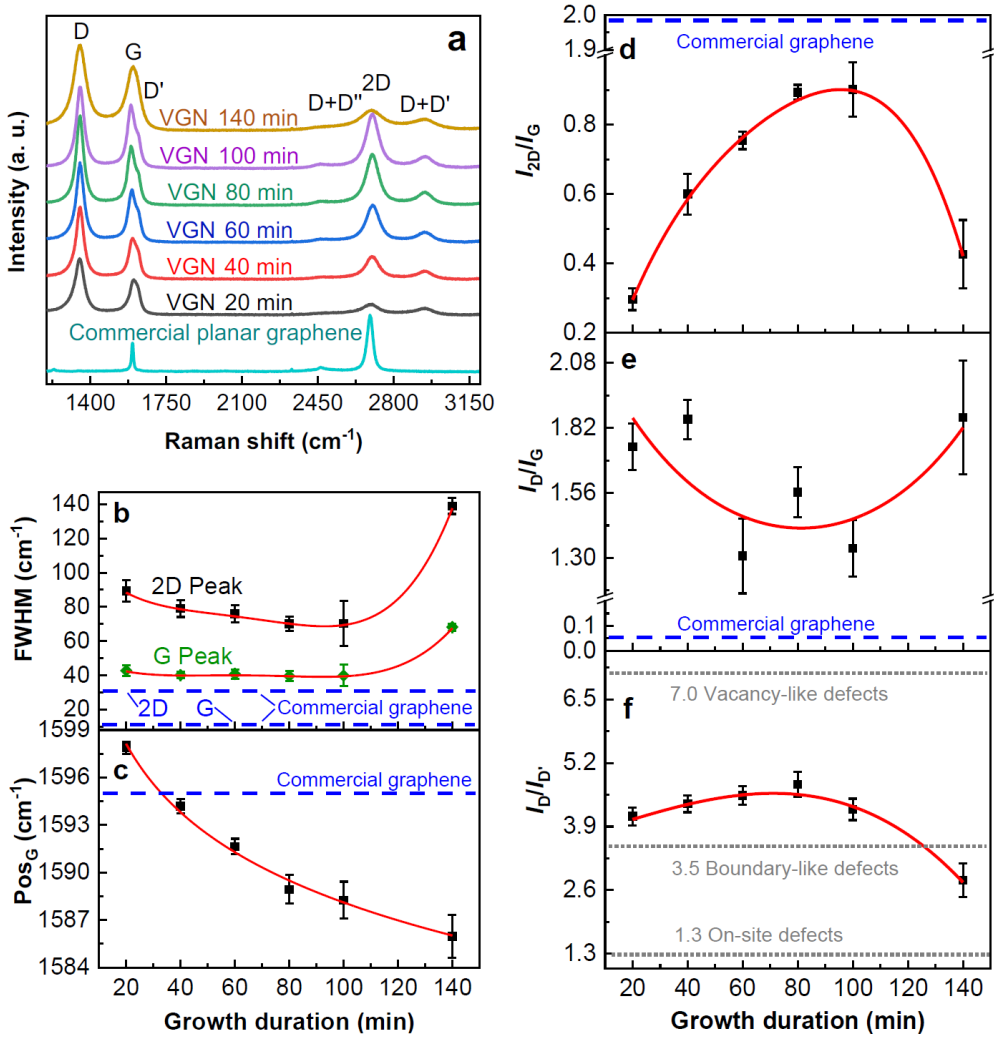

Figure 38. Raman scattering analysis. Raman scattering spectra of VGN deposited at 20–140 min and commercial graphene (**a**), FWHM (**b**), Pos_G (**c**), I_{2D}/I_G (**d**), I_D/I_G (**e**), $I_D/I_{D'}$ (**f**) dependencies on the growth duration [A1]

The fitting results of the characteristic bands are presented in **Table 9** and **Figure 38 b–e**, **Figure 39**. It should be noted that, along with the growth time, the intensities of the G and 2D peaks increase, the full widths at half maximum (FWHM) of the corresponding bands decrease (with slight fluctuations) (**Figure 38 b**), and the G and D′ peaks become more separate, which specifies a more ordered structure, except for the VGN sample grown for 140 min [53,156]. Besides, the G band positions (Pos_G) downshift from 1597.85 to 1585.96 cm^{-1} (**Figure 38 c**), and the intensity ratios I_{2D}/I_G increase (**Figure 38 d**) with the deposition time, thereby indicating the enhancement in crystallinity [53], yet, again, except for the longest grown sample. The VGN deposited at 140 min demonstrates a more defected, less developed crystalline structure.

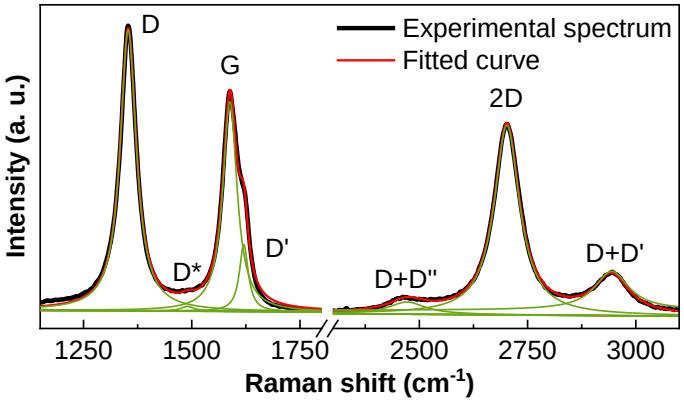

Figure 39. Typical Raman spectrum of VGN grown for 100 min onto fused silica substrate by microwave plasma-enhanced chemical vapour deposition (MW PECVD) and its deconvolution with a Lorentzian line shape

Table 9. Fitting results of characteristic peaks of Raman scattering spectra

Sample	VGN 20 min	VGN 40 min	VGN 60 min	VGN 80 min	VGN 100 min	VGN 140 min	Commercial planar graphene
Pos_D (cm^{-1})	1349.74	1352.10	1352.73	1351.89	1353.37	1351.88	1347.52
I_D (a. u.)	5869.22	7590.97	8272.93	9539.56	8748.38	8983.30	110.90
$FWHM_D$ (cm^{-1})	57.58	45.62	46.17	42.90	44.85	76.88	15.02
Pos_G (cm^{-1})	1597.85	1594.18	1591.64	1588.94	1588.25	1585.96	1595.03
I_G (a. u.)	3364.75	4094.78	5393.72	6104.86	6536.83	4825.51	3144.87
$FWHM_G$ (cm^{-1})	42.73	40.13	40.69	39.59	39.88	68.19	10.57
$Pos_{D'}$ (cm^{-1})	1619.62	1619.78	1621.42	1620.48	1620.22	1611.82	*1628.43*
$I_{D'}$ (a. u.)	1428.72	1739.24	1824.83	2002.29	2057.83	3206.61	*61.58*
$FWHM_{D'}$ (cm^{-1})	21.00	22.24	22.26	22.79	23.90	39.76	*6.93*
Pos_{2D}, cm^{-1}	2693.54	2701.02	2703.56	2701.86	2702.13	2697.04	2692.61
I_{2D} (a. u.)	998.88	2456.38	4072.05	5455.90	5895.34	2058.91	6238.68
$FWHM_{2D}$ (cm^{-1})	89.31	78.99	76.00	70.16	70.33	139.03	30.75
I_{2D}/I_G	0.30	0.60	0.75	0.89	0.90	0.43	1.98
I_D/I_G	1.74	1.85	1.31	1.56	1.34	1.86	0.04
$I_D/I_{D'}$	4.11	4.36	4.53	4.76	4.25	2.80	*1.80*

The Raman peak positions of the G and 2D bands of VGN samples are blue-shifted in comparison to commercial planar graphene (**Table 9**) and pristine graphene from reference [171]. This could be caused by the compressive strains of vertical graphene nanosheets and the nanographitic layer [146]. The blue shift of the commercial graphene Raman peaks can be attributed to the p-doping that appears because of PMMA used for its transfer onto fused silica substrate [193]. Concerning a direct comparison of VGN samples with commercial planar graphene, it becomes

somewhat complicated, whereas not all fitting parameters of the commercial graphene spectrum are reliable due to its high quality and, consequently, of the low intensity and the merger of the peaks (these parameters are marked in *Italic* in **Table 9**).

Furthermore, it is known that the intensity ratio I_D/I_G provides information about the number of defects in a disordered graphitic material [194]. The data presented in the graph of the I_D/I_G ratio dependence on the growth time more or less follow the trend of a parabola and varies in the range from 1.31 to 1.86 (**Figure 38 e**, **Table 9**), where the sample VGN 60 min features the lowest amount of defects (the minimum of the parabola), whereas the sample grown the longest (140 min) possesses the highest number of defects. What is more, it is clarified that the intensities of the D and D′ peaks also depend on the nature of the defects within the material [195]. According to classification presented in [164], the $I_D/I_{D'}$ ratio with the value of 7 corresponds to vacancy-like defects which are more common for planar graphene as was shown in previous studies [A2]. As displayed in the plot of $I_D/I_{D'}$ vs. the growth duration (**Figure 38 f**), the $I_D/I_{D'}$ ratio values of the VGN samples (**Table 9**) are located in the area close to the value of 3.5 which indicates the presence of boundary-like defects, and this is a peculiarity of vertical graphene films [53]. The estimated average distance between the nearest point defects (L_D) and the average crystallite size (L_a) [A2][48] vary within the ranges of 8.80–10.49 nm and 2.37–3.39 nm, respectively, for VGN samples (**Table 10**). These calculations were performed by using the method described in references [53,95,156,167–169,196]. It is also important to note that, starting from the VGN 100 min sample, $I_D/I_{D'}$ starts to drop down towards the zone describing the on-site defects characterised by $I_D/I_{D'}$ ~1.3. On-site defects are related to out-of-plane atoms bonded to carbon atoms in the graphene sheet (specifically, sp^3 hybridization) and appear in the form of dimers or clusters [164].

Table 10. Average distance between the nearest defects (L_D), and the average crystallite size (L_a) for VGN

Graphene	L_D **(nm)**	L_a **(nm)**
VGN 20 min	9.10±4.80	~2.53
VGN 40 min	8.83±4.65	~2.38
VGN 60 min	10.49±5.53	~3.39
VGN 80 min	9.61±5.07	~2.82
VGN 100 min	10.37±5.47	~3.28
VGN 140 min	8.80±4.64	~2.37

The optical microscope images (**Figure 40**) of all the VGN samples contain black dots of a varying size and density over the surfaces. High-resolution SEM micrographs of those dark spots (**Figure 41**) revealed the presence of nanofibers twisted into diverse ball-like aggregates and other 3D carbon nanostructures which could be attributed to the above mentioned on-site defects.

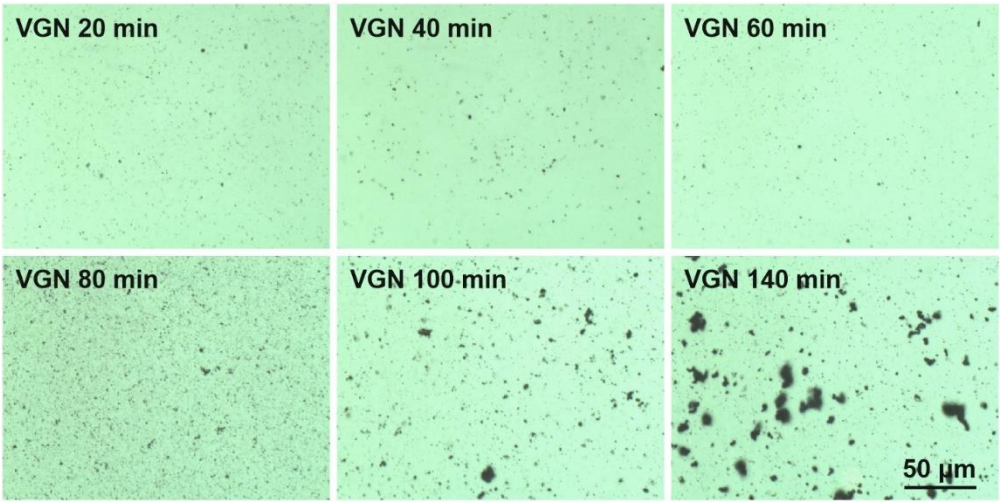

Figure 40. Optical microscope images of VGN samples deposited at 20–140 min (scale bar 50 µm)

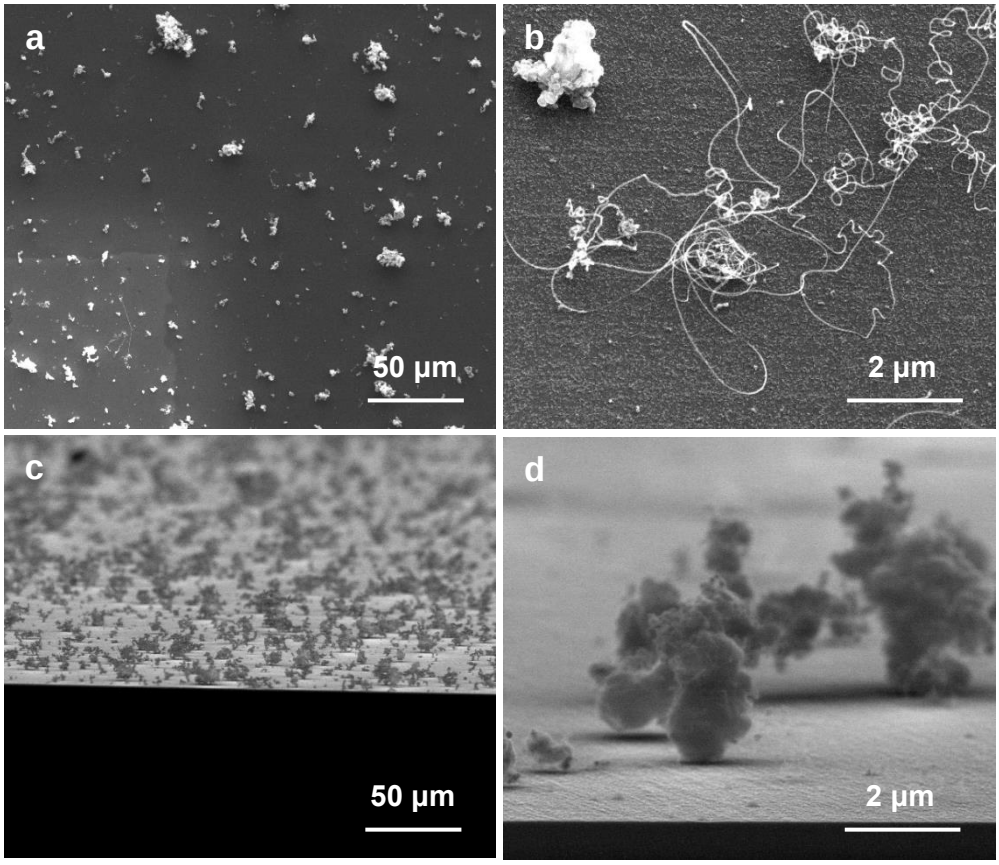

Figure 41. Low magnification SEM images of VGN 140 min; (**a**) and (**b**) tilted at 45º, (**c**) and (**d**) tilted at 90º

The explanation for this phenomenon lies in the deposition conditions – the amount of the H_2 component in the CH_4/H_2 gas mixture, as well as the thermal and electrical energy, were high enough [154] for the enhanced formation of other carbon deposits such as a-C, carbon nanotubes, carbon nanofibers, graphitic fragments, and the rugged columnar structures of a-C on top of the surface [197]. Such deposits could have been conditioned by the formation of high-mass ionic carbon clusters $C_nH_x^+$ ($n \geq 2$, $x = 1, 2, 3$) comprising the generation of low-mass ions from the reactions induced by energetic electrons and hydrogen ions or molecules, and the successive ionic chain polymerisation [72,154]. The VGN 60 min appears to possess the 'cleanest' surface, while VGN 140 min – the most 'contaminated' one, which is a good agreement with the Raman spectroscopy results (**Figure 38**).

4.2.3. Electrical properties

Electrical TLM measurement results support the observations in the morphology changes of the grown VGN samples which lead to different sheet resistances (R_S) as presented in **Figure 42**.

For the sample VGN 20 min, the R_S value is the highest, and it equals 7.20 kΩ/sq due to the structural defects and the disorder of the predominant lightly conductive NG base layer as discussed above. With the growth time increasing till 100 min, the sheet resistance gradually decreases down to 0.88 kΩ/sq, which indicates the growing network of high quality and particularly conductive few-layered VGN which starts to prevail over the relatively highly resistive NG film. The sample VGN 140 min does not follow this progressive tendency and shows a slightly elevated R_S value of 0.90 kΩ/sq because of a less developed vertically standing graphene net, as can be seen in the SEM micrographs (**Figure 36**) and in the AFM measurement scans (**Figure 37 e**). Such electrical investigation is particularly sensitive to the most conductive parts of these complex VGN layers (as the current flows along the shortest path) which are crystalline vertical graphene sheets and are not affected by the presence of 3D carbon structures which develop on the samples' surfaces as out-of-plane defects.

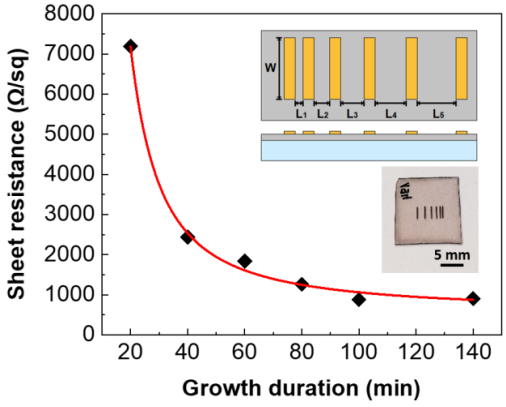

Figure 42. Sheet resistance dependence on the growth duration of VGN 20–140 min samples. The inset depicts the schematics and a photo of a typical sample with electrodes used in TLM measurements [A1]

4.2.4. Optical properties

The steady-state absorption spectra of VGN samples are shown in **Figure 43 a**. One can see that, for VGN samples grown for 20–100 min, the absorbance (optical density) increases with an increase of the processing duration. This can be explained by the growth of the effective thickness of vertical graphene nanosheets with a longer deposition time (**Figure 13**, **Figure 36**). Surprisingly, VGN 140 min does not show an increase in absorption at a wavelength of 270 nm and is even lower compared to VGN 100 min (**Figure 43 a**). Nevertheless, the integrated absorbance of VGN 140 min is larger than the one of VGN 100 min because VGN 140 min has larger absorption at the spectral area of ~320–600 nm. The relative increase of the absorbance of VGN 140 min in the long wavelength region is even more visible from the normalised absorption plot (**Figure 43 b**). This increase of absorbance at the ~320–600 nm wavelength range could mean the formation of new carbon derivatives [198,199].

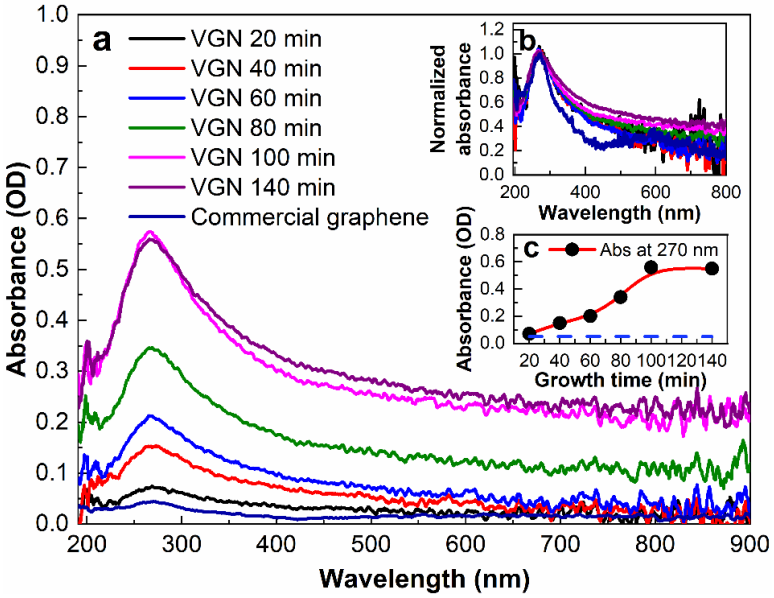

Figure 43. Steady-state absorption spectra of vertical graphene nanosheets (the fused silica extinction spectrum was subtracted (**a**); in the inset: the received absorption spectra were normalised (**b**)), and the steady-state absorption values at 270 nm of samples VGN 20–140 min and commercial planar graphene (the horizontal line) in the inset (**c**) [A1]

The Raman spectroscopy (**Figure 38**, **Table 9)** and morphology analysis (**Figure 40**, **Figure 41**) support the idea about an increase of carbon allotropes in the VGN 140 min sample in comparison to the other samples. It is known that the absorption peak at 270 nm corresponds to excitonic Fano resonance which reflects the interband transition at the M-point (the saddle-point) in the Brillouin zone of graphene; therefore, this peak can be associated directly with graphene absorption [10,37,180]. Thus, the VGN 140 min sample has less graphene (sp^2 bonded carbon atoms) than the VGN 100 min sample.

4.2.5. Nonlinear optical properties

The TAS measurements of VGN and commercial graphene were performed in order to investigate the correlation between the excited state relaxation dynamics and the defects of VGN samples (**Figure 44**). It should be noted that only a negative TAS signal was observed for all the samples (**Figure 44**). It is known that a negative TAS signal is typical for graphene [189] and it appears because of the Pauli blocking principle [184]. Commercial planar graphene TAS results confirm that VGN samples comprise sp^2 bonded carbon atoms (**Figure 45**).

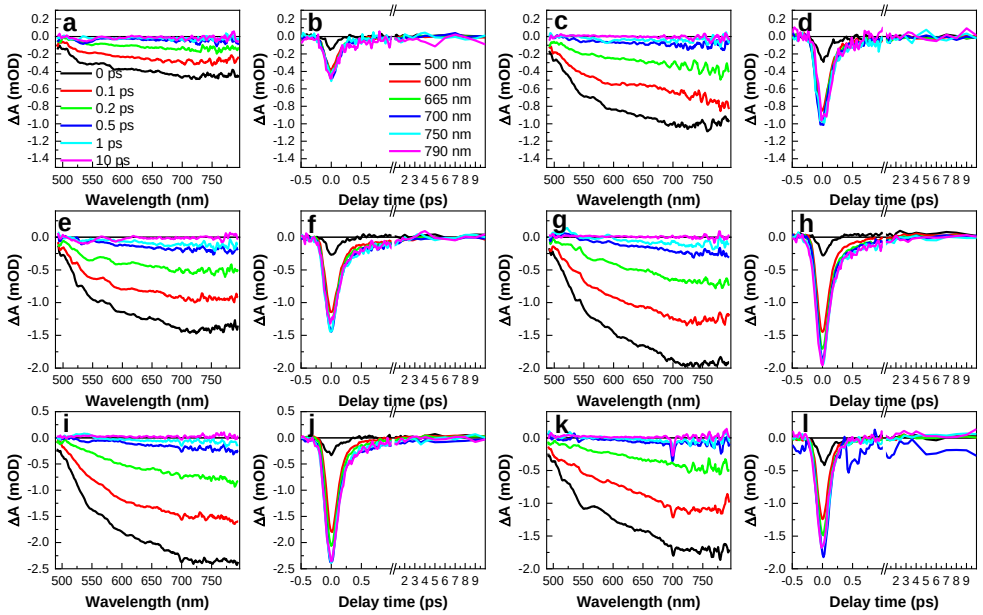

Figure 44. TAS spectra (**a**, **c**, **e**, **g**) and traces (**b**, **d**, **f**, **h**, **j**, **i**) measured for VGN deposited when using different durations: 20 (**a**, **b**), 40 (**c**, **d**), 60 (**e**, **f**), 80 (**g**, **h**), 100 (**i**, **j**) and 140 min (**k**, **l**)

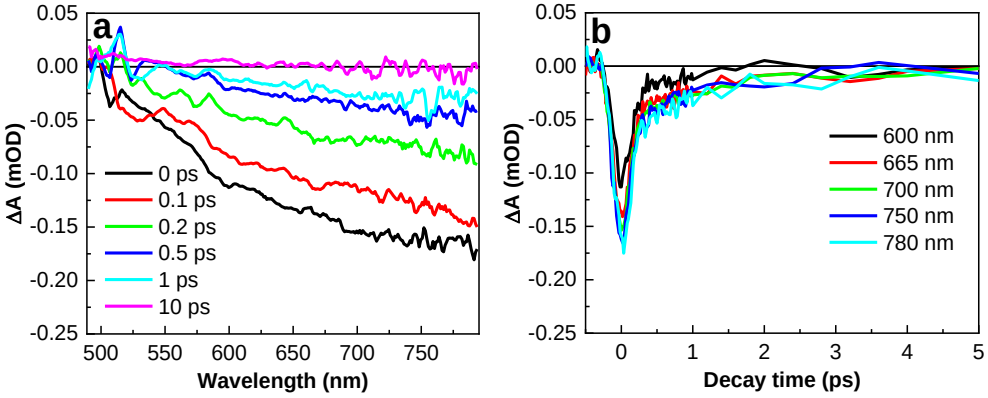

Figure 45. Transient absorption (pump-probe) spectra (**a**) and traces (**b**) of commercial planar graphene (pristine graphene) transferred onto fused silica

The TAS signal amplitude values were picked from the trace 750 nm (at the peak of the negative TAS spectra) at 0 ps and presented in **Figure 46**, where one can see that this value depends on the growth time. The graph depicts almost perfect linear TAS signal dependence on the VGN growth time except for the sample VGN 140 min, in which case the amplitude decreases dramatically. This dependence correlates with the steady-state absorption data presented in **Figure 43 c**, except that VGN 140 min TAS signal amplitude decreases more in comparison to the absorption spectrum. It should be noted that the dependence of the roughness of VGN measured with AFM on the growth time (**Figure 37 f**) exhibits some similarities to the variation of the steady-state absorption amplitude at 270 nm (**Figure 43 c**) and the amplitude of TAS traces 750 nm at 0 ps (**Figure 46**).

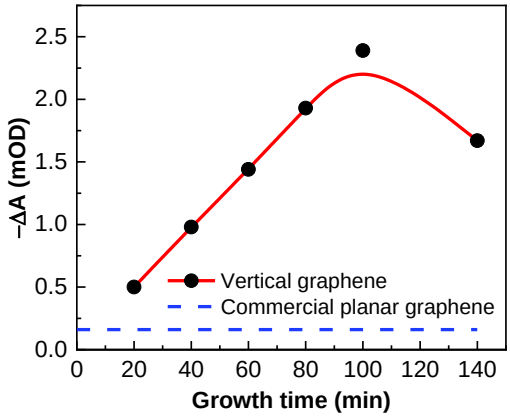

Figure 46. TAS signal amplitude at 750 nm; 0 ps delay line of VGN 20–140 min samples and commercial graphene

Excited state relaxation dynamics was extracted from the TAS traces depicted in **Figure 45** while fitting them by the two exponential decay functions:

$$I(t) = A_1 e^{-\frac{t}{\tau_1}} + A_2 e^{-\frac{t}{\tau_2}} + I_0; \qquad \text{(Eq. 7)}$$

where A_1; A_2 are the amplitudes, and τ_1; τ_2 are the decay time constants, while I_0 represents the TAS signal background [152].

The fitting results are summarised in **Table 11** and **Figure 47**. The differences in the relaxation dynamics of different VGN samples are highlighted in the semi-logarithmic plot of the normalised TAS signal traces depicted in **Figure 48.** From the analysis of the data presented in **Table 11** as well as **Figure 48**, one can conclude that the sample of VGN 140 min does not follow the general tendency similarly to what was expected from the morphology and Raman scattering spectroscopy analysis. Its integrated steady-state absorption is the largest, but the TAS signal is less intense than that of the samples VGN 100 min and VGN 80 min. It seems that VGN 140 min has less graphene in comparison to VGN 100 min and even VGN 80 min. According to the TAS results, it is most probable that VGN 140 min has a larger amount of other carbon derivatives. This explains the obtained largest integrated steady-state absorption of this sample.

Table 11. Decay times and amplitudes of VGN 20–140 min samples based on TAS data*

Sample (trace at 665 nm)	τ_1 (ps)	A_1	τ_2 (ps)	A_2	R^2
VGN 20 min	0.15±0.01	0.96±0.03	2.33±2.41	0.04±0.02	0.9748
VGN 40 min	0.16±0.01	0.95±0.02	4.82±3.27	0.05±0.01	0.9860
VGN 60 min	0.16±0.01	0.9±0.02	1.93±0.62	0.1±0.02	0.9913
VGN 80 min	0.16±0.01	0.94±0.02	1.71±1.22	0.06±0.02	0.9913
VGN 100 min	0.16±0.01	0.96±0.02	2.44±2.04	0.04±0.01	0.9898
VGN 140 min	0.13±0.01	0.98±0.02	4.55±11.93	0.02±0.02	0.9892
Commercial Graphene	0.14±0.01	0.79±0.03	2.28±0.58	0.21±0.02	0.9700

*$A_1 + A_2 = 1$

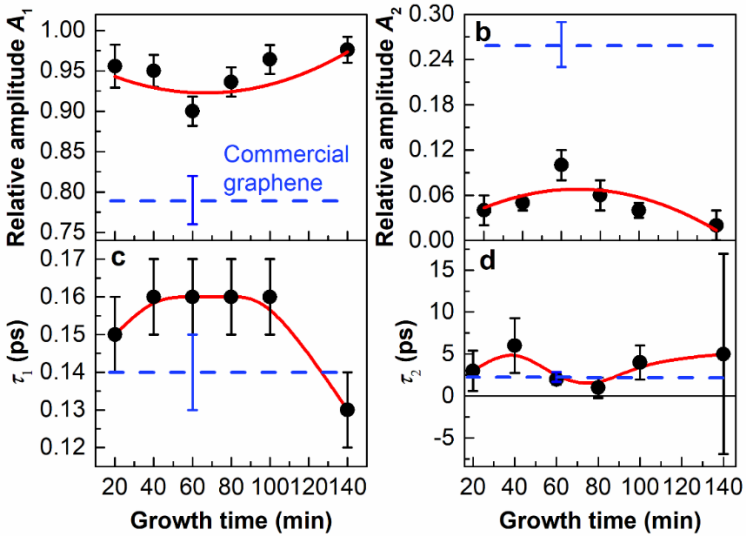

Figure 47. Decay amplitudes (**a**, **b**) and times (**c**, **d**) of VGN 20–140 min samples based on TAS data [A1]

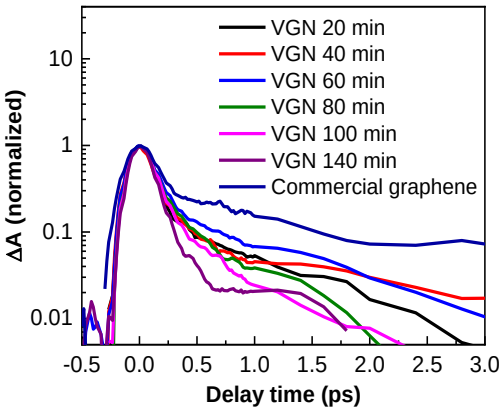

Figure 48. Normalised TAS traces at 665 nm of samples VGN 20–140 min

The decay times of pristine (commercial planar) graphene are shown in **Table 11**. Both TAS and Raman scattering analysis indicate that VGN 60 min has the best quality graphene based on the I_D/I_G and TAS signal decay data (**Figure 38 e**, **Table 9**, **Table 11**). For the quality of the VGN analysis, the most interesting parameter from **Table 11** is A_2. The values of A_2, which correspond to samples VGN 60 min and VGN 80 min, have the largest relative amplitudes of 0.1 and 0.06, respectively. Meanwhile, for other samples, these amplitudes are 0.05 or less. Keeping in mind that A_2 for the measured commercial graphene is 0.26, it can be suggested that the increase of A_2 for the samples of VGN 60 and 80 min is because of better quality graphene in these samples. That partly corresponds to the Raman measurement result (**Table 11**, **Table 9**). Most likely, the difference can be explained by the different laser beam spot diameters used for the TAS (500 μm) and Raman (4 μm) scattering spectroscopy measurements. In the previous research (see Section 4.1.7.) [A2], the TAS relaxation traces of VGN had no A_2 component, but, at the same time, VGN also showed a higher defect level in comparison to the ones analysed in the present Section 4.2.5.

Based on the proven research, the TAS relaxation signal of pristine graphene consists of two exponential decay components: the fast one ~150 fs, and the slower one at ~2 ps [36,75,184,189], which can even reach ~4 ps in some cases [37]. In the previous VGN TAS measurements, only the fast TAS signal decay time was found (see Section 4.1.7.) [A2], thus indicating a relatively low quality or major disorder of the graphene samples. In those cases, it was confirmed by the Raman scattering data (see Section 4.1.4.) [A2].

To conclude this Section 4.2., the synthesis of vertical graphene nanosheets employing MW PECVD at a constant power and fixed working gas (methane and hydrogen) ratio with varying growth durations from 20 min to 140 min yielded samples of continuous films of a nanographitic base layer and vertically standing graphene nanostructures of different development levels. According to the morphology analysis, the increase of the deposition duration results in the growth of the height of VGN up to some critical thickness (or deposition time) when, most probably, plasma instability and conditioned electric field alterations through plasma jumps or new flashpoints ignition take place deteriorating further the VGN growth in height.

Both steady-state and transient absorption spectra intensity amplitudes for the VGN samples increase linearly along with the growth duration up to some critical time when various other carbon allotropes start to be deposited thus illustrating that very long deposition times make the VGN formation unstable.

It has been shown that TAS signal decay times can provide information about the defects and the disorder of VGN films. The increase in the defects of VGN layers determines the decrease of the relative amplitude of the longer TAS signal relaxation component. The VGN transient absorption spectroscopy and Raman scattering spectroscopy spectra show similar tendencies in terms of disorder. The TAS data corresponds very well with the I_{2D}/I_G, I_D/I_G dependences on the growth time thus indicating that TAS can be used as an efficient tool for graphene quality evaluation.

4.3. Investigation of the electrochromic device with graphene electrode performance

4.3.1. Investigation of the graphene electrode structure and its optical properties

The formation of graphene layers by using the MW PECVD technique was examined by Raman scattering spectroscopy. In **Figure 49**, the Raman spectrum of graphene deposited on a double copper foil is presented. Three well expressed characteristic peaks are monitored in the spectrum: peak D at 1349 cm^{-1} (which is observed due to point defects), peak G at 1582 cm^{-1} (vibrations of carbon atoms connected by sp^2 bonds in the plane), and peak 2D at 2698 cm^{-1} (the second order of the D band). In order to determine how many graphene layers have been formed, the 2D peak was approximated by one Lorentzian peak, and a peak half-width of ~46 cm^{-1} was obtained. The determined I_{2D}/I_G ratio was equal to 1.05. Based on these results of Raman scattering spectroscopy, it can be stated that the graphene film consists of 2–3 layers. Few-layered graphene features higher conductivity than a monolayer, but at the same time it is very important to maintain high transparency of the film as well. Such graphene films were used to form electrodes for organic electrochromic devices.

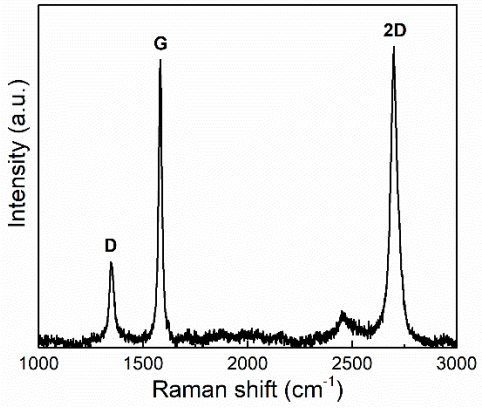

Figure 49. Raman scattering spectrum of graphene formed on a double copper foil

The Raman scattering spectrum of graphene transferred on a flexible PET substrate is shown in **Figure 50**. Due to the strong signal of PET, the graphene-specific peaks are of low intensity, some of them overlap with the PET peaks. Graphene Raman characteristic bands are indicated by dashed squares in the spectrum. The only peak that does not overlap is the 2D peak, which can be used to describe the quality of graphene transposition. Since it was registered for all the transferred graphene layers, it can be stated that the transfer was successful.

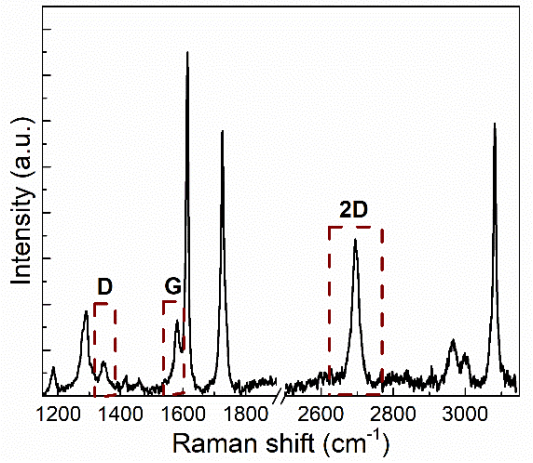

Figure 50. Raman scattering spectrum of a graphene layer transferred on the PET substrate

Conventional ITO electrodes are widely used for the formation of pellucid electrochromic devices not only because of their good electrical properties, but also due to their transparency. Graphene films distinguish themselves for their high transparency as well, which varies depending on how many layers have been formed. **Figure 51** represents the transmittance spectrum of the PET substrate and the change in its optical properties after graphene transfer. As it can be seen, the transmittance of the substrate decreases slightly with the graphene layer placed on top. In the visible range (400–600 nm), the transmittance of PET with a graphene film decreases by 4–7%, and, at longer wavelengths, the impact of the added graphene layer on the optical permeability of the substrate becomes even more insignificant.

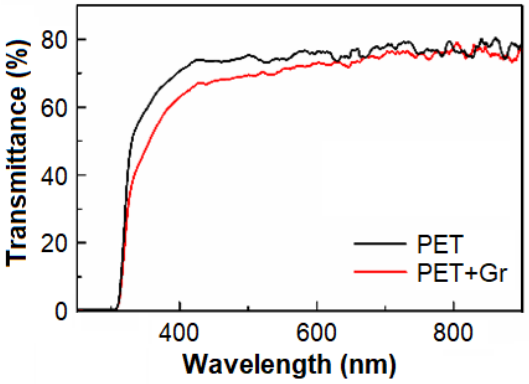

Figure 51. Optical transmittance spectra of PET substrate before and after graphene layer transfer

4.3.2. Graphene electrode electro-optical properties

Ultrafast excited state relaxation dynamics in graphene were investigated by employing transient absorption spectroscopy (**Figure 52**). The samples were excited with laser pulses of 350 nm, 20.8 μJ/cm^2, 200/3 kHz. The dynamics of the

amplitudes of these transient absorption signals over time can be used to describe the processes that take place in the excited state. The data received during these measurements indicate that ultrafast TAS relaxation traces consisted of two parts, the faster one (~1 ps) and the slower one (~100 ps). The first duration of decay can be attributed to electron cooling by thermal equilibration with the lattice, while the second one could be assigned to the cooling of the lattice. It is important to note that the fast process can be assigned to the formation of the charge transfer state. It was also observed that the TAS relaxation dynamics of graphene depend on the dielectric constant of the substrate. An increase of the dielectric constant of the substrate causes a decrease of the TAS relaxation time constant.

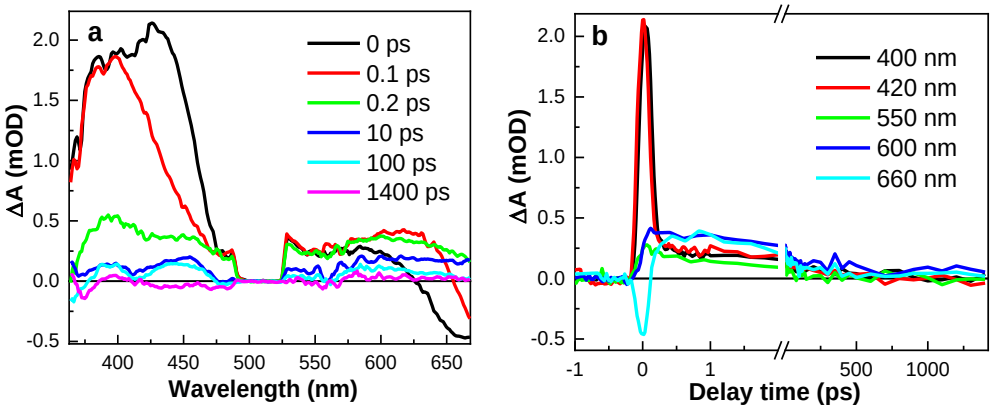

Figure 52. TAS spectra (**a**) and traces (**b**) of graphene on PET. Excitation 350 nm, 2 mW

4.3.3. Performance of electrochromic device

The PET with transferred graphene and ITO was used as one of the electrodes in an electrochromic device with Prussian blue as the active material. The influence of the graphene layer on the device performance was investigated.

The electrochemical reduction of PB induced by an external voltage (-3 V to the graphene/PET) yields colourless or bleached EC layers (**Figure 53 a**). The application of a reverse external field (3 V to graphene/PET) induces an oxidation process which generates mixed valence compounds and yields the blue colour of the EC layers (**Figure 53 b**). A longer application of 3 V external voltage yields the yellow colour of the EC layer (**Figure 53 c**).

Figure 53. Bleached state (-3 V) (**a**), blue state (3 V) (**b**), and yellow state (3 V) (**c**) of electrochromic device performance

The influence of the applied voltage on the transmittance of the system was tested. The recorded transmittance spectra of PB/Graphene/PET in all the stages are given in **Figure 54**. The optical transmittance varies within ~20 percentage points from the bleached state value: T_{700nm} = 32%, coloured: T_{700nm} = 10%, and intermediate yellow colour state: T_{700nm} = 17%. The typical bleaching and colouration times are 39 s and 20 s, respectively. These values were much higher compared to that of an EC device using the same PB EC film and the same electrolyte, but featuring an ITO electrode: bleaching – 3 s, colouration – 10 s. Such results were most likely conditioned by the 100-time higher sheet resistance of the graphene layers (~1200 Ω/sq) comparatively to ITO films (≤10 Ω/sq).

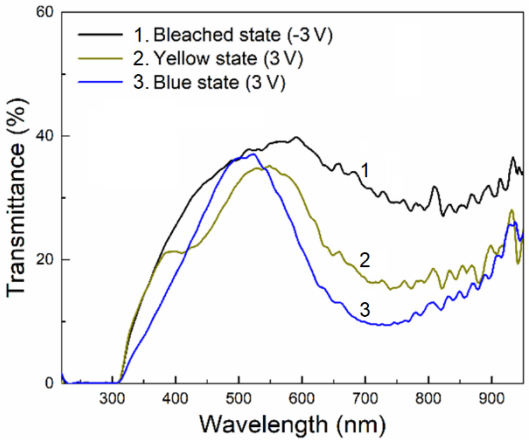

Figure 54. Transmittance variation of the PB/Graphene/PET system with the switch of voltage from -3 V to 3 V

In conclusion, such application-oriented experiments demonstrate the great potential of MW PECVD synthesised graphene layers to be integrated as conductive, chemically stable, transparent and flexible electrodes into organic devices. Further cases of application of planar graphene as an electrode material in organic solar cells are presented in the next chapter.

4.4. Investigation of organic solar cell performance

A number of graphene layers synthesised with the MW PECVD technique under identical conditions and transferred onto PET and fused silica substrates were investigated by Raman scattering spectroscopy. In **Figure 55 a**, the Raman spectrum of one of the graphene samples on fused silica confirms the graphitic structure (the characteristic G and 2D bands are well expressed) of a single layer (I_{2D}/I_G = ~3 in most of the area).

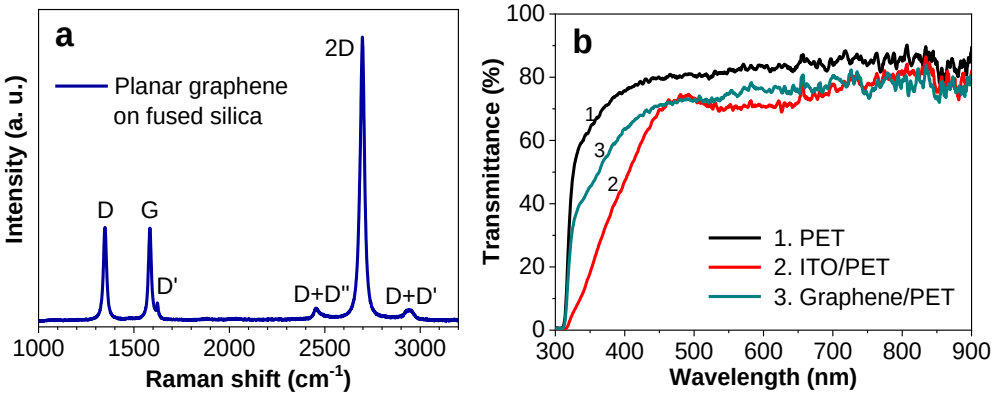

Figure 55. Raman scattering spectrum of planar graphene transferred onto a quartz substrate (**a**), transmittance spectra of PET foil, ITO on PET, graphene on PET (**b**)

The sheet resistance of graphene layers transferred onto a quartz substrate is about 1.2 kΩ/sq. This value is significantly higher than the sheet resistance of the commercially available ITO on PET, which is ≤10 Ω/sq. As seen in the Raman scattering spectra of one of the graphene films, there is a D peak indicating the presence of defects causing a decrease in conductivity. In **Figure 55 b**, the transmittance spectra of graphene and ITO layers on PET foils are provided. As it can be seen, the transmittance of graphene layers on PET is comparable to or slightly better than ITO on PET in the visible range. Graphene films are suitable for applications as transparent flexible electrodes, but their relatively high conductivity remains an issue.

The main characteristics describing the performance of OSC are the short circuit current density (J_{SC}), the open-circuit voltage (V_{OC}), the fill factor (FF) estimated from the measured volt-ampere (*J*-*V*) curves, and the power conversion efficiency PCE calculated according to the following Equation 8:

$$\mathrm{PCE} = \frac{P_{max}}{P_{in.}} = \frac{J_{SC} \cdot V_{OC} \cdot \mathrm{FF}}{P_{in.}} \qquad \text{(Eq. 8)}$$

These parameters of fabricated OSC with graphene electrodes (see Section 3.6.2.) are depicted in **Figure 56**. The highest values of all the characteristics (PCE, J_{SC}, V_{OC}, FF) were found for the OSC featuring the PET/Gr/MoO_3 (10 nm)/PCE12:ITIC/Bphene (20 nm)/Ag configuration. In the inverted version, the same configuration was described by one of the lowest values. In order to increase the conductivity of graphene electrodes, a thin silver layer of 3 nm was evaporated on the surface of graphene. Another way to improve the conductivity of graphene electrodes is to form a layer of spherical silver NP of 20 nm diameter on top of graphene. As it can be seen in **Figure 56**, the performance of OSC with these additional layers did not show significant improvement.

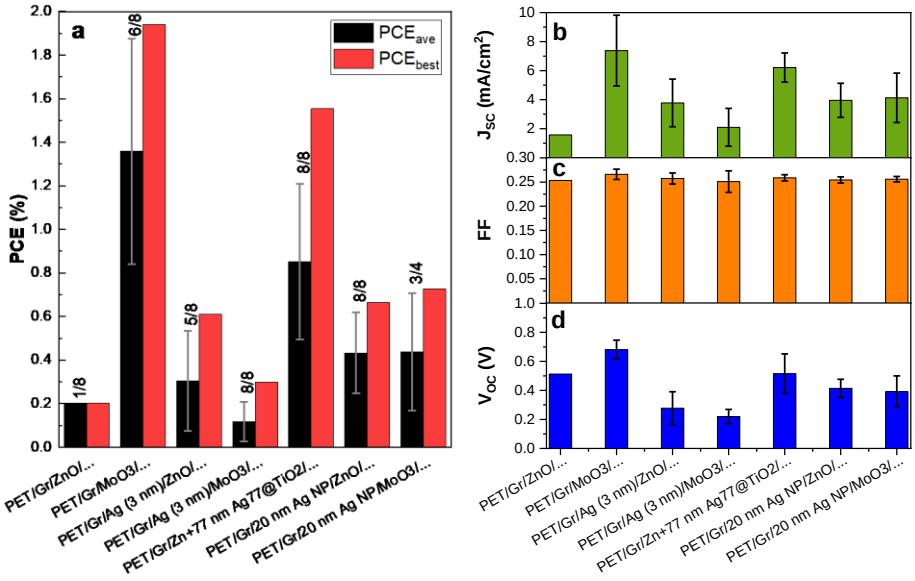

Figure 56. Diagrams of power conversion efficiency PCE (**a**), short circuit current density J_{SC} (**b**), fill factor FF (**c**), and open-circuit voltage V_{OC} (**d**) of OSC with graphene electrodes

Figure 27 represents the main volt-ampere characteristics and PCE of OSC with graphene and their analogous devices with ITO electrodes. Conventional OSC including ITO demonstrated notably better performance. The reference sample involving the ITO layer produced the highest PCE value of 10%, while the PCE of photovoltaic devices with a similar configuration based on the PCE12:ITIC active layer can reach >12% [200].

What is more, an additional layer of Ag NP on ITO in the device configuration Glass/ITO/20 nm Ag NP/MoO_3/PCE12:ITIC/Bphene (20 nm)/Ag resulted in the highest J_{SC} and V_{OC}.

What concerns the fill factor, it essentially shows the quality of solar cells. A greater factor implies a greater fraction of the theoretical power that can be produced. The FF of all OSC with graphene electrodes did not vary significantly, and it was close to the value of 0.25 (**Figure 27 c**). The devices with ITO yielded an FF greater than 0.62 (going up to 0.67), which is more than twice as much as the FF of OSC with graphene. The best FF (0.67) was obtained for the inverted configuration: Glass/ITO/ZnO+77 nm Ag@TiO_2 NP/PCE12:ITIC/MoO_3 (10 nm)/Ag, where cubic silver nanoparticles (NP) with TiO_2 shell (Ag@TiO_2) of 77 nm size were mixed with ZnO solution that was used for ETL formation so that to improve the charge carrier transport. Detailed analysis of the properties of the used Ag@TiO_2 NP is presented in [152].

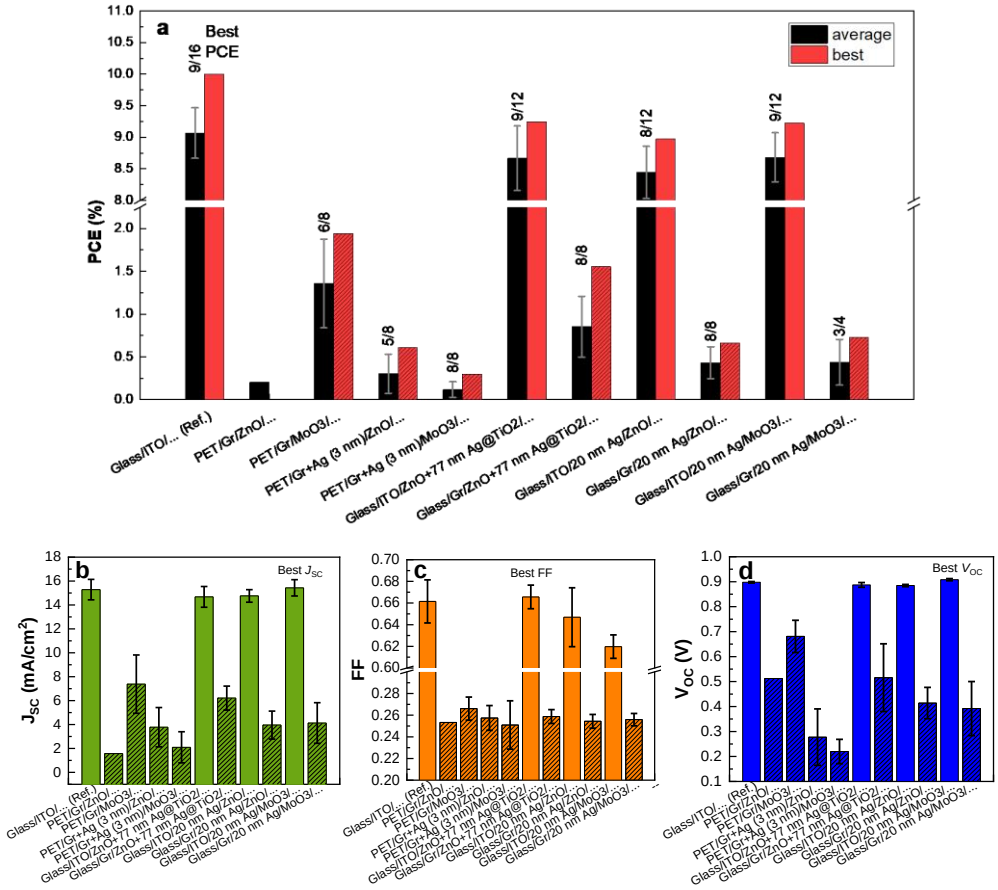

Figure 57. Diagrams of power conversion efficiency PCE (**a**), short circuit current density J_{SC} (**b**), fill factor FF (**c**), and open-circuit voltage V_{OC} (**d**) of OSC with graphene and ITO electrodes

In conclusion, organic photovoltaic devices with integrated transparent flexible graphene electrodes do not outperform the ones with the conventional ITO electrodes; however, graphene electrodes are promising for the flexible electrode configuration which is not possible with ITO [9,201,202].

V. CONCLUSIONS

1. The complex analysis performed by scanning electron microscopy, atomic force microscopy, X-ray photoelectron spectroscopy, Raman scattering spectroscopy, the transmission line model, transient absorption spectroscopy and other methods has revealed that the properties of graphene layers formed by the microwave plasma-enhanced chemical vapour deposition on catalytic copper foil and transferred onto fused silica (planar graphene) and directly deposited vertical graphene nanosheets onto fused silica are relatively different in terms of the morphology, structure, and defects. It has been determined that the main type of defects in vertical graphene nanosheets together with the nanographitic layer were edges and boundaries, whereas the defects in planar graphene were mostly present because of vacancies.

2. The synthesis of planar graphene on a catalyst by microwave plasma-enhanced chemical vapour deposition resulted in a continuous film composed of 1–3 layers with a sheet resistance of 1.2 kΩ/sq. It has experimentally been asserted that the wet-chemical transfer process onto foreign substrates (fused silica, poly(ethylene terephthalate)) can be successfully accomplished even without using the poly(methyl methacrylate) support and plasma pre-treatment, thus avoiding additional contamination.

3. The kinetics of the synthesis of vertical graphene nanosheet layers employing microwave plasma-enhanced chemical vapour deposition at a constant power and a fixed working gas (methane and hydrogen) ratio, but with a varying growth duration from 20 min to 140 min, was explored. It has been shown that such a deposition yielded samples of continuous films of a nanographitic base layer and vertically standing graphene nanostructures of various levels of development. On the grounds of morphology analysis, it has been determined that an increase of the deposition duration results in the growth of the height of vertical graphene nanosheets up to some critical thickness (or deposition time) when, most probably, plasma instability and conditioned electric field alterations take place, thus subsequently deteriorating further vertical graphene nanosheet growth in height.

4. Both steady-state and transient absorption spectra intensity amplitudes for the vertical graphene samples increase linearly along with the growth duration up to some critical time when other various carbon allotropes, such as out-of-plane defects, start to be deposited, thus illustrating that very long deposition times make vertical graphene nanosheet formation unstable.

5. It has been demonstrated that the decay times and the relative amplitude of the longer relaxation component of the transient absorption spectroscopy signal can provide information about the defects and disorder and serve as an efficient characterisation technique to analyse the quality of both types of graphene; therefore, it can complement the Raman scattering spectroscopy method which suffers from some limitations in the analysis of the defects of vertical graphene films. The transient absorption spectroscopy and Raman scattering spectroscopy spectra of vertical graphene nanosheet layers show similar tendencies in terms of defects. The transient absorption spectroscopy data corresponds very well with the

I_{2D}/I_G, I_D/I_G dependencies on the growth time, thus indicating that transient absorption spectroscopy can be used as an efficient tool for graphene quality evaluation.

6. The complex analysis of graphene layers, in parallel to the pump-probe spectroscopy measurements, demonstrates that transient absorption spectroscopy analysis of the excited state dynamics in graphene may potentially lead to the creation of an effective methodology of the fast and reliable evaluation of the quality of graphene. Unfortunately, an open question still remains how to describe the density and the type of disorder by the data of transient absorption spectroscopy in a quantifiable way. More studies on the influence of specific defects on the transient absorption signal are necessary in order to make this method more versatile for the quality assessment of various graphene films.

7. The application-oriented experiments demonstrate the great potential of microwave plasma-enhanced chemical vapour deposited graphene layers to be integrated as conductive, chemically stable, transparent and flexible electrodes into organic devices. An electrochromic device based on Persian blue as the active material and graphene electrodes showed bleaching and coloration durations 13 and 2 times longer than the values of an electrochromic device with indium tin oxide electrodes, respectively.

8. What concerns organic photovoltaics, the highest values of the main characteristics, specifically, a power conversion efficiency of 1.94%, and a fill factor of 0.27, were found for the organic solar cell with graphene having the PET/Gr/MoO_3/PCE12:ITIC/Bphene/Ag configuration, which is 5 times and more than twice less than the values of the solar cell with indium tin oxide (a power conversion efficiency of 10.00%, a fill factor of 0.66), respectively. Although organic solar cells with graphene electrodes did not surpass the ones with the widely used indium tin oxide electrodes, graphene layers offer abundant promise for the flexible electrode configuration, which is not possible with indium tin oxide.

ACKNOWLEDGEMENTS

The author wishes to express sincere gratitude to the supervisor prof. dr. habil. Sigitas Tamulevičius for the guidance, support and all the provided opportunities to improve as a researcher and a personality. The author is highly grateful to dr. Domantas Peckus and dr. Rimantas Gudaitis for the significant overall help while preparing this dissertation work.

The author would like to sincerely thank each and every colleague from the Institute of Materials Science of Kaunas University of Technology, Mads Clausen Institute of University of Southern Denmark, Prof. Julia Fedotova from the Institute for Nuclear Problems for the cooperative work, trainings, assistance, valuable discussions, motivation and, above all, friendship.

REFERENCES

1. L. LIN, H. PENG, Z. LIU, Synthesis challenges for graphene industry. *Nat. Mater.* 2019, Vol. 18, p. 520–529. DOI 10.1038/s41563-019-0341-4.
2. R. YE, J.M. TOUR, Graphene at Fifteen. *ACS Nano*. 2019, Vol. 13, p. 10872–10878. DOI 10.1021/acsnano.9b06778.
3. W. KONG, H. KUM, S.-H. BAE, J. SHIM, H. KIM, L. KONG, Y. MENG, K. WANG, C. KIM, J. KIM, Path towards Graphene Commercialization from Lab to Market. *Nat. Nanotechnol.* 2019, Vol. 14, p. 927–938. DOI 10.1038/s41565-019-0555-2.
4. A.G. OLABI, M.A. ABDELKAREEM, T. WILBERFORCE, E.T. SAYED, Application of Graphene in Energy Storage Device – A Review. *Renew. Sustain. Energy Rev.* 2021, Vol. 135, p. 110026. DOI 10.1016/j.rser.2020.110026.
5. X.J. LEE, B.Y.Z. HIEW, K.C. LAI, L.Y. LEE, S. GAN, S. THANGALAZHY-GOPAKUMAR, S. RIGBY, Review on graphene and its derivatives: Synthesis methods and potential industrial implementation. *J. Taiwan Inst. Chem. Eng.* 2019, Vol. 98, p. 163–180. DOI 10.1016/j.jtice.2018.10.028.
6. M.T. SAFIAN, K. UMAR, M.N.M. IBRAHIM, Synthesis and scalability of graphene and its derivatives: A journey towards sustainable and commercial material. *J. Clean. Prod.* 2021, Vol. 318, p. 128603. DOI 10.1016/j.jclepro.2021.128603.
7. L. CAI, G. YU, Fabrication Strategies of Twisted Bilayer Graphenes and Their Unique Properties. *Adv. Mater.* 2021, Vol. 33, p. 2004974. DOI 10.1002/adma.202004974.
8. J.T. HOPE, W. SUN, S. KEWALRAMANI, S. SAHA, P. LAKHE, S.A. SHAH, M.J. MASON, M.J. GREEN, R.A. HULE, Scalable Production of Graphene Nanoplatelets for Energy Storage. *ACS Appl. Nano Mater.* 2020, Vol. 3, p. 10303–10309. DOI 10.1021/acsanm.0c02209.
9. P. MANDAL, J. DEBBARMA, M. SAHA, A Review on the Emergence of Graphene in Photovoltaics Industry. *Biointerface Res. Appl. Chem.* 2021, Vol. 11, no. 6, p. 15009–15036. DOI 10.33263/BRIAC116.1500915036.
10. E. MALIC, A. KNORR, Graphene and Carbon Nanotubes. 2013, DOI 10.1002/9783527658749.
11. A.P. KAULING, A.T. SEEFELDT, D.P. PISONI, R.C. PRADEEP, R. BENTINI, R.V.B. OLIVEIRA, K.S. NOVOSELOV, A.H.C. NETO, The Worldwide Graphene Flake Production. *Adv. Mater.* 2018, Vol. 30, no. 44, p. 1803784 (1-6). DOI 10.1002/adma.201803784.
12. N. KUMAR, R. SALEHIYAN, V. CHAUKE, O.J. BOTLHOKO, K. SETSHEDI, M. SCRIBA, M. MASUKUME, S.S. RAY, Top-down synthesis of graphene: A comprehensive review. *FlatChem*. 2021, Vol. 27, p. 100224. DOI 10.1016/j.flatc.2021.100224.
13. Y. WU, S. WANG, K. KOMVOPOULOS, A review of graphene synthesis by indirect and direct deposition methods. *J. Mater. Res.* 2020, Vol. 35, no. 1, p. 76–89. DOI 10.1557/jmr.2019.377.

14. Y. YAN, F.Z. NASHATH, S. CHEN, S. MANICKAM, S.S. LIM, H. ZHAO, E. LESTER, T. WU, C.H. PANG, Synthesis of graphene: Potential carbon precursors and approaches. *Nanotechnol. Rev.* 2020, Vol. 9, p. 1284–1314. DOI 10.1515/ntrev-2020-0100.
15. O. BAYRAM, O. SIMSEK, Vertically oriented graphene nano-sheets grown by plasma enhanced chemical vapor deposition technique at low temperature. *Ceram. Int.* 2019, Vol. 45, no. 11, p. 13664–13670. DOI 10.1016/j.ceramint.2019.04.034.
16. J. WANG, Z. REN, Y. HOU, X. YAN, P. LIU, H. ZHANG, H. ZHANG, J. GUO, A review of graphene synthesis at low temperatures by CVD methods. *New Carbon Mater.* 2020, Vol. 35, no. 3, p. 193–208. DOI 10.1016/S1872-5805(20)60484-X.
17. J. KULCZYK-MALECKA, V.J. ISABELLA, M. BETBEDER, S.J. ROWLEY-, Z. GAO, P.J. KELLY, Low-temperature synthesis of vertically aligned graphene through microwave-assisted chemical vapour deposition. *Thin Solid Films*. 2021, Vol. 733, p. 138801. DOI 10.1016/j.tsf.2021.138801.
18. X. ZHANG, C. YAN, C. ZENG, T. SUN, Z. XING, W. SHI, Y. WANG, C. PANG, B. ZHANG, Epitaxial synthesis of graphene on 4H-SiC by microwave plasma chemical vapor deposition. *Mater. Res. Express*. 2020, Vol. 7, p. 116410. DOI 10.1088/2053-1591/abcb3a.
19. P. FORTUGNO, S. MUSIKHIN, X. SHI, H. WANG, H. WIGGERS, C. SCHULZ, Synthesis of freestanding few-layer graphene in microwave plasma: The role of oxygen. *Carbon N. Y.* 2022, Vol. 186, p. 560–573. DOI 10.1016/j.carbon.2021.10.047.
20. Y.-Z. HUANG, S.-C. TSENG, Y.-H. CHEN, H.-Y. TSAI, The mechanisms of carbon nano-flake balls growth by laser ablation and microwave plasma chemical vapor deposition. *Surf. Coat. Technol.* 2021, Vol. 425, p. 127668. DOI 10.1016/j.surfcoat.2021.127668.
21. J. SHAN, L. CUI, F. ZHOU, R. WANG, K. CUI, Y. ZHANG, Z. LIU, Ethanol-Precursor-Mediated Growth and Thermochromic Applications of Highly Conductive Vertically Oriented Graphene on Soda-Lime Glass. *ACS Appl. Mater. Interfaces*. 2020, Vol. 12, no. 10, p. 11972–11978. DOI 10.1021/acsami.9b23122.
22. X. ZHANG, Y. TANG, P. HE, Z. ZHANG, T. CHEN, Edge-rich vertical graphene nanosheets templating V2O5 for highly durable zinc ion battery. *Carbon N. Y.* 2021, Vol. 172, p. 207–213. DOI 10.1016/j.carbon.2020.10.034.
23. P. HE, S. CHEN, Vertically Oriented Graphene Nanosheets for Electrochemical Energy Storage. *ChemElectroChem*. 2021, Vol. 8, no. 5, p. 783–797. DOI 10.1002/celc.202001364.
24. J. SUN, T. RATTANASAWATESUN, P. TANG, Z. BI, S. PANDIT, L. LAM, C. WAS, M. ERLANDSSON, M. BOKAREWA, J. DONG, F. DING, F. XIONG, I. MIJAKOVIC, Insights into the Mechanism for Vertical Graphene Growth by Plasma-Enhanced Chemical Vapor Deposition. *ACS Appl. Mater. Interfaces*. 2022, Vol. 14, p. 7152–7160. DOI 10.1021/acsami.1c21640.
25. H. WANG, E. GAO, P. LIU, D. ZHOU, D. GENG, X. XUE, L. WANG, K. JIANG,

Z. XU, G. YU, Facile growth of vertically-aligned graphene nanosheets via thermal CVD: The experimental and theoretical investigations. *Carbon N. Y.* 2017, Vol. 121, p. 1–9. DOI 10.1016/j.carbon.2017.05.074.
26. P. JI, J. CHEN, T. HUANG, C. JIN, L. ZHUGE, X. WU, Fast preparation of vertical graphene nanosheets by helicon wave plasma chemical vapor deposition and its electrochemical performance. *Diam. Relat. Mater.* 2020, Vol. 108, p. 107958. DOI 10.1016/j.diamond.2020.107958.
27. Z. CHEN, Y. QI, X. CHEN, Y. ZHANG, Z. LIU, Direct CVD Growth of Graphene on Traditional Glass: Methods and Mechanisms. *Adv. Mater.* 2019, Vol. 31, p. 1803639. DOI 10.1002/adma.201803639.
28. S. XU, S. WANG, Z. CHEN, Y. SUN, Z. GAO, H. ZHANG, J. ZHANG, Electric-Field-Assisted Growth of Vertical Graphene Arrays and the Application in Thermal Interface Materials. *Adv. Funct. Mater.* 2020, Vol. 30, no. 34, p. 2003302 (1-7). DOI 10.1002/adfm.202003302.
29. C.A. CLIFFORD, E.H.M. FERREIRA, T. FUJIMOTO, J. HERRMANN, A.R.H. WALKER, D. KOLTSOV, C. PUNCKT, L. REN, G.J. SMALLWOOD, A.J. POLLARD, The importance of international standards for the graphene community. *Nat. Rev. Phys.* 2021, Vol. 3, p. 233–235. DOI 10.1038/s42254-021-00278-6.
30. A.C. FERRARI, Raman spectroscopy of graphene and graphite: Disorder, electron-phonon coupling, doping and nonadiabatic effects. *Solid State Commun.* 2007, Vol. 143, no. 1–2, p. 47–57. DOI 10.1016/j.ssc.2007.03.052.
31. L.M. MALARD, M.A. PIMENTA, G. DRESSELHAUS, M.S. DRESSELHAUS, Raman spectroscopy in graphene. *Phys. Rep.* 2009, Vol. 473, no. 5–6, p. 51–87. DOI 10.1016/j.physrep.2009.02.003.
32. D. PECKUS, T. TAMULEVIČIUS, Š. MEŠKINIS, A. TAMULEVIČIENĖ, A. VASILIAUSKAS, O. ULČINAS, V. GULBINAS, S. TAMULEVIČIUS, Linear and Nonlinear Absorption Properties of Diamond-Like Carbon Doped With Cu Nanoparticles. *Plasmonics*. 2016, Vol. 12, p. 47–58. DOI 10.1007/s11468-016-0227-0.
33. Š. MEŠKINIS, D. PECKUS, A. VASILIAUSKAS, A. ČIEGIS, R. GUDAITIS, T. TAMULEVIČIUS, I. YAREMCHUK, S. TAMULEVIČIUS, Photovoltaic Properties and Ultrafast Plasmon Relaxation Dynamics of Diamond-Like Carbon Nanocomposite Films with Embedded Ag Nanoparticles. *Nanoscale Res. Lett.* 2017, Vol. 12, p. 288. DOI 10.1186/s11671-017-2065-1.
34. R.W. NEWSON, J. DEAN, B. SCHMIDT, H.M. VAN DRIEL, Ultrafast carrier kinetics in exfoliated graphene and thin graphite films. *Opt. Express*. 2009, Vol. 17, no. 4, p. 2326. DOI 10.1364/OE.17.002326.
35. D. BRIDA, A. TOMADIN, C. MANZONI, Y.J. KIM, A. LOMBARDO, S. MILANA, R.R. NAIR, K.S. NOVOSELOV, A.C. FERRARI, G. CERULLO, M. POLINI, Ultrafast collinear scattering and carrier multiplication in graphene. *Nat. Commun.* 2013, Vol. 4, p. 1–9. DOI 10.1038/ncomms2987.
36. K.-C. HUANG, J. MCCALL, P. WANG, C.-S. LIAO, G. EAKINS, J.-X. CHENG, C. YANG, High-Speed Spectroscopic Transient Absorption Imaging of Defects in Graphene. *Nano Lett.* 2018, Vol. 18, no. 2, p. 1489–1497. DOI

10.1021/acs.nanolett.7b05283.
37. K. OUM, T. LENZER, M. SCHOLZ, D.Y. JUNG, O. SUL, B.J. CHO, J. LANGE, A. MULLER, Observation of Ultrafast Carrier Dynamics and Phonon Relaxation of Graphene from the Deep-Ultraviolet to the Visible Region. *J. Phys. Chem. C*. 2014, Vol. 118, no. 12, p. 6454−6461. DOI 10.1021/jp4072197.
38. R. MA, Y. ZHOU, H. BI, M. YANG, J. WANG, Q. LIU, F. HUANG, Multidimensional graphene structures and beyond: Unique properties, syntheses and applications. *Prog. Mater. Sci.* 2020, Vol. 113, p. 100665. DOI 10.1016/j.pmatsci.2020.100665.
39. G. YANG, L. LI, W.B. LEE, M.C. NG, Structure of graphene and its disorders: a review. *Sci. Technol. Adv. Mater.* 2018, Vol. 19, no. 1, p. 613–648. DOI 10.1080/14686996.2018.1494493.
40. K. DAVAMI, Y. JIANG, J. CORTES, C. LIN, M. SHAYGAN, K.T. TURNER, I. BARGATIN, Tuning the mechanical properties of vertical graphene sheets through atomic layer deposition. *Nanotechnology*. 2016, Vol. 27, p. 155701. DOI 10.1088/0957-4484/27/15/155701.
41. K. YU, P. WANG, G. LU, K. CHEN, Z. BO, J. CHEN, Patterning Vertically Oriented Graphene Sheets for Nanodevice Applications. *J. Phys. Chem. Lett.* 2011, Vol. 2, p. 537–542. DOI 10.1021/jz200087w.
42. J.-B. WU, M.-L. LIN, X. CONG, H.-N. LIU, P.-H. TAN, Raman spectroscopy of graphene-based materials and its applications in related devices. *Chem. Soc. Rev.* 2018, Vol. 47, no. 5, p. 1822–1873. DOI 10.1039/c6cs00915h.
43. M.J. ALLEN, V.C. TUNG, R.B. KANER, Honeycomb Carbon: A Review of Graphene. *Chem. Rev.* 2010, Vol. 110, p. 132–145.
44. M. AOKI, H. AMAWASHI, Dependence of band structures on stacking and field in layered graphene. *Solid State Commun.* 2007, Vol. 142, p. 123–127. DOI 10.1016/j.ssc.2007.02.013.
45. A. GARCÍA-RUIZ, J.J.P. THOMPSON, M. MUCHA-KRUCZY, V.I. FAL'KO, Electronic Raman Scattering in Twistronic Few-Layer Graphene. *Phys. Rev. Lett.* 2020, Vol. 125, p. 197401. DOI 10.1103/PhysRevLett.125.197401.
46. G.G. SAMSONIDZE, E.B. BARROS, R. SAITO, J. JIANG, G. DRESSELHAUS, M.S. DRESSELHAUS, Electron-phonon coupling mechanism in two-dimensional graphite and single-wall carbon nanotubes. *Phys. Rev. B.* 2007, Vol. 75, p. 155420. DOI 10.1103/PhysRevB.75.155420.
47. A.H.C. NETO, F. GUINEA, N.M.R. PERES, K.S. NOVOSELOV, A.K. GEIM, The electronic properties of graphene. *Rev. Mod. Phys.* 2009, Vol. 81, p. 109–162. DOI 10.1103/RevModPhys.81.109.
48. J. WU, M. LIN, X. CONG, H. LIU, P. TAN, Raman spectroscopy of graphene-based materials and its applications in related devices. *Chem. Soc. Rev.* 2018, Vol. 47, p. 1822–1873. DOI 10.1039/c6cs00915h.
49. M. LAZZERI, C. ATTACCALITE, L. WIRTZ, F. MAURI, Impact of the electron-electron correlation on phonon dispersion: Failure of LDA and GGA DFT functionals in graphene and graphite. *Phys. Rev. B.* 2008, Vol. 78, p. 081406(R). DOI 10.1103/PhysRevB.78.081406.
50. F.H.L. KOPPENS, T. MUELLER, P. AVOURIS, A.C. FERRARI, M.S. VITIELLO,

M. POLINI, Photodetectors based on graphene, other two-dimensional materials and hybrid systems. *Nat. Nanotechnol.* 2014, Vol. 9, no. 10, p. 780–793. DOI 10.1038/nnano.2014.215.
51. Y. MA, H. JANG, S.J. KIM, C. PANG, H. CHAE, Copper-Assisted Direct Growth of Vertical Graphene Nanosheets on Glass Substrates by Low-Temperature Plasma-Enhanced Chemical Vapour Deposition Process. *Nanoscale Res. Lett.* 2015, DOI 10.1186/s11671-015-1019-8.
52. S. ZHENG, G. ZHONG, X. WU, L.D. ARSI, J. ROBERTSON, Metal-catalyst-free growth of graphene on insulating substrates by ammonia-assisted microwave plasma-enhanced chemical vapor deposition. *RSC Adv.* 2017, Vol. 7, p. 33185–33193. DOI 10.1039/c7ra04162d.
53. S. GHOSH, K. GANESAN, S.R. POLAKI, T.R. RAVINDRAN, N.G. KRISHNA, M. KAMRUDDIN, A.K. TYAGI, Evolution and defect analysis of vertical graphene nanosheets. *J. Raman Spectrosc.* 2014, Vol. 45, no. 8, p. 642–649. DOI 10.1002/jrs.4530.
54. W. ZHENG, X. ZHAO, W. FU, Review of Vertical Graphene and its Applications. *ACS Appl. Mater. Interfaces*. 2021, Vol. 13, p. 9561–9579. DOI 10.1021/acsami.0c19188.
55. J. CHU, Y. HAN, Y. LI, P. JIA, H. CUI, S. DUAN, P. FENG, X. PENG, Study of the structural evolution and gas sensing properties of PECVD-synthesized graphene nanowalls. *J. Phys. D. Appl. Phys.* 2020, Vol. 53, p. 325101. DOI 10.1088/1361-6463/ab87be.
56. A. KAZEMZADEH, M.A. MESHKAT, H. KAZEMZADEH, M. MORADI, R. BAHRAMI, R. POURIAMANESH, Preparation of graphene nanolayers through surfactant-assisted pure shear milling method. *J. Compos. Compd.* 2019, Vol. 2, p. 22–26. DOI 10.29252/jcc.2.1.4.
57. O. JAŠEK, J. TOMAN, J. JURMANOVÁ, M. ŠNÍRER, V. KUDRLE, V. BURŠÍKOVÁ, Study of graphene layer growth on dielectric substrate in microwave plasma torch at atmospheric pressure. *Diam. Relat. Mater.* 2020, Vol. 105, p. 107798. DOI 10.1016/j.diamond.2020.107798.
58. X. GUO, Y. LI, Y. DING, Q. CHEN, J. LI, Direct patterned growth of intrinsic/doped vertical graphene nanosheets on stainless steel via heating solid precursor films for field emission application. *Mater. Des.* 2019, Vol. 162, p. 293–299. DOI 10.1016/j.matdes.2018.11.056.
59. P. CIOCHO, M. MARZEC, N. OLSZOWSKA, J. KO, Reversible graphitization of SiC: A route towards high-quality graphene on a minimally step bunched substrate. *Appl. Surf. Sci.* 2020, Vol. 528, p. 146917. DOI 10.1016/j.apsusc.2020.146917.
60. R. TAO, F. LI, X. LU, F. LIU, J. XU, D. KONG, C. ZHANG, X. TAN, S. MA, W. SHI, R. MO, Y. LU, High-Conductivity–Dispersibility Graphene Made by Catalytic Exfoliation of Graphite for Lithium-Ion Battery. *Adv. Funct. Mater.* 2021, Vol. 31, p. 2007630. DOI 10.1002/adfm.202007630.
61. S. KANIYANKANDY, S.N. ACHARY, S. RAWALEKAR, H.N. GHOSH, Ultrafast Relaxation Dynamics in Graphene Oxide: Evidence of Electron Trapping. *J. Phys. Chem. C.* 2011, Vol. 115, no. 39, p. 19110–19116. DOI

10.1021/jp206923q.
62. P. A GEORGE, J. STRAIT, J. DAWLATY, S. SHIVARAMAN, M. CHANDRASHEKHAR, F. RANA, M.G. SPENCER, Spectroscopy of the Carrier Relaxation Epitaxial Graphene. *Nano Lett.* 2008, Vol. 8, no. 12, p. 17–20. DOI 10.102/nl8019399.
63. Y. ZHANG, L. ZHANG, C. ZHOU, Review of Chemical Vapor Deposition of Graphene and Related Applications. *Acc. Chem. Res.* 2013, Vol. 46, no. 10, p. 2329–2339. DOI 10.1021/ar300203n.
64. L. SUN, G. YUAN, L. GAO, J. YANG, M. CHHOWALLA, M.H. GHARAHCHESHMEH, K.K. GLEASON, Y.S. CHOI, B.H. HONG, Z. LIU, Chemical vapour deposition. *Nat. Rev.* 2021, Vol. 1, p. 1–20. DOI 10.1038/s43586-020-00005-y.
65. J. SUN, Y. ZHANG, Z. LIU, Direct Chemical Vapor Deposition Growth of Graphene on Insulating Substrates. *ChemNanoMat*. 2016, Vol. 2, p. 9–18. DOI 10.1002/cnma.201500160.
66. L. LIN, B. DENG, J. SUN, H. PENG, Z. LIU, Bridging the Gap between Reality and Ideal in Chemical Vapor Deposition Growth of Graphene. *Chem. Rev.* 2018, Vol. 118, p. 9281–9343. DOI 10.1021/acs.chemrev.8b00325.
67. S. XU, L. ZHANG, B. WANG, R.S. RUOFF, Review Chemical vapor deposition of graphene on thin-metal films. *Cell Reports Phys. Sci.* 2021, Vol. 2, p. 100372. DOI 10.1016/j.xcrp.2021.100372.
68. Q. SHI, K. TOKARSKA, H.Q. TA, X. YANG, Y. LIU, S. ULLAH, L. LIU, B. TRZEBICKA, A. BACHMATIUK, J. SUN, L. FU, Z. LIU, M.H. RÜMMELI, Substrate Developments for the Chemical Vapor Deposition Synthesis of Graphene. *Adv. Mater. Interfaces*. 2020, Vol. 7, p. 1902024. DOI 10.1002/admi.201902024.
69. S. HUSSAIN, E. KOVACEVIC, J. BERNDT, N.M. SANTHOSH, C. PATTYN, A. DIAS, T. STRUNSKUS, M.-R. AMMAR, A. JAGODAR, M. GAILLARD, C. BOULMER-LEBORGNE, U. CVELBAR, Low-temperature low-power PECVD synthesis of vertically aligned graphene. *Nanotechnology*. 2020, Vol. 31, p. 395604. DOI 10.1088/1361-6528/ab9b4a.
70. K. YI, D. LIU, X. CHEN, J. YANG, D. WEI, Y. LIU, D. WEI, Plasma-Enhanced Chemical Vapor Deposition of Two-Dimensional Materials for Applications. *Acc. Chem. Res.* 2021, Vol. 54, p. 1011–1022. DOI 10.1021/acs.accounts.0c00757.
71. J. WANG, Z. REN, Y. HOU, X. YAN, P. LIU, H. ZHANG, H. ZHANG, J. GUO, A review of graphene synthesisatlow temperatures by CVD methods. *New Carbon Mater.* 2020, Vol. 35, no. 3, p. 193–208. DOI 10.1016/S1872-5805(20)60484-X.
72. Z. BO, Y. YANG, J. CHEN, K. YU, J. YAN, K. CEN, Plasma-enhanced chemical vapor deposition synthesis of vertically oriented graphene nanosheets. *Nanoscale*. 2013, Vol. 5, no. 12, p. 5180–5204. DOI 10.1039/c3nr33449j.
73. L. TAI, D. ZHU, X. LIU, T. YANG, L. WANG, R. WANG, S. JIANG, Z. CHEN, Z. XU, X. LI, Direct Growth of Graphene on Silicon by Metal-Free Chemical Vapor Deposition. *Nano-Micro Lett.* 2018, Vol. 10, no. 2, p. 1–9. DOI

10.1007/s40820-017-0173-1.
74. N. YEH, C. HSU, J. BAGLEY, W.-S. TSENG, Single-step growth of graphene and graphene-based nanostructures by plasma-enhanced chemical vapor deposition. *Nanotechnology*. 2019, Vol. 30, p. 162001. DOI 10.1088/1361-6528/aafdbf.
75. K.-C. LIN, M.-Y. LI, L.J. LI, D.C. LING, C.C. CHI, J.-C. CHEN, Ultrafast dynamics of hot electrons and phonons in chemical vapor deposited graphene. *J. Appl. Phys.* 2013, Vol. 113, no. 13, p. 133511. DOI 10.1063/1.4799377.
76. J.A. ANDRADE, J. FOLKSON, M. BOUKHICHA, A.J. CARR, M.D. EISAMAN, Bifacial Multilayer Graphene Float Transfer. *Adv. Funct. Mater.* 2020, Vol. 30, p. 2005103. DOI 10.1002/adfm.202005103.
77. N. HONG, D. KIREEV, Q. ZHAO, D. CHEN, D. AKINWANDE, W. LI, Roll-to-Roll Dry Transfer of Large-Scale Graphene. *Adv. Mater.* 2022, Vol. 34, p. 2106615. DOI 10.1002/adma.202106615.
78. L.-P. MA, S. DONG, H.-M. CHENG, W. REN, Breaking the Rate-Integrity Dilemma in Large-Area Bubbling Transfer of Graphene by Strain Engineering. *Adv. Funct. Mater.* 2021, Vol. 31, p. 2104228. DOI 10.1002/adfm.202104228.
79. N. SOIN, S. ROY, C.O. KANE, J.A.D. MCLAUGHLIN, T.H. LIM, C.J.D. HETHERINGTON, Exploring the fundamental effects of deposition time on the microstructure of graphene nanoflakes by Raman scattering and X-ray diffraction. *CrystEngComm*. 2011, Vol. 13, p. 312–318. DOI 10.1039/c0ce00285b.
80. V. KRIVCHENKO, P. SHEVNIN, A. PILEVSKY, A. EGOROV, N. SUETIN, V. SEN, S. EVLASHINA, A. RAKHIMOV, Influence of the growth temperature on structural and electron field emission properties of carbon nanowall/nanotube films synthesized by catalyst-free PECVD. *J. Mater. Chem. C*. 2012, Vol. 22, p. 16458. DOI 10.1039/c2jm32263c.
81. S. VIZIREANU, B. MITU, C.R. LUCULESCU, L.C. NISTOR, G. DINESCU, PECVD synthesis of 2D nanostructured carbon material. *Surf. Coat. Technol.* 2012, Vol. 211, p. 2–8. DOI 10.1016/j.surfcoat.2011.07.092.
82. H. ZHANG, S. WU, Z. LU, X. CHEN, Q. CHEN, P. GAO, T. YU, Z. PENG, J. YE, Efficient and controllable growth of vertically oriented graphene nanosheets by mesoplasma chemical vapor deposition. *Carbon N. Y.* 2019, Vol. 147, p. 341–347. DOI 10.1016/j.carbon.2019.01.042.
83. S. VIZIREANU, S.D. STOICA, C. LUCULESCU, L.C. NISTOR, B. MITU, G. DINESCU, Plasma techniques for nanostructured carbon materials synthesis. A case study: carbon nanowall growth by low pressure expanding RF plasma. *Plasma Sources Sci. Technol.* 2010, Vol. 19, p. 034016. DOI 10.1088/0963-0252/19/3/034016.
84. S.J. GOLDIE, S. BUSH, J.A. CUMMING, K.S. COLEMAN, A Statistical Approach to Raman Analysis of Graphene-Related Materials: Implications for Quality Control. *ACS Appl. Nano Mater.* 2020, Vol. 3, p. 11229–11239. DOI 10.1021/acsanm.0c02361.

85. E. CAZZANELLI, O. DE LUCA, D. VUONO, A. POLICICCHIO, M. CASTRIOTA, G. DESIDERIO, M. PENELOPE, D.S. ALFREDO, A. FASANELLA, T. RUGIERO, R. GIUSEPPE, Characterization of graphene grown on copper foil by chemical vapor deposition (CVD) at ambient pressure conditions. *J. Raman Spectrosc.* 2018, Vol. 49, p. 1006–1014. DOI 10.1002/jrs.5375.
86. B.-Y. JU, W.-S. YANG, Q. ZHANG, M. HUSSAIN, Z.-Y. XIU, J. QIAO, G.-H. WU, Research progress on the characterization and repair of graphene defects. *Int. J. Miner. Metall. Mater.* 2020, Vol. 27, p. 1179–1190. DOI 10.1007/s12613-020-2031-2.
87. D.L. SILVA, L.R.P. MACHADO, E.M. SOARES, D.R. MIQUITA, H. MIRANDA, C. RABELO, O.P. VILELA, A. JORIO, L. GUSTAVO, Raman spectroscopy analysis of number of layers in mass-produced graphene flakes. *Carbon N. Y.* 2020, Vol. 161, p. 181–189. DOI 10.1016/j.carbon.2020.01.050.
88. M.V.O. MOUTINHO, P. VENEZUELA, M.A. PIMENTA, Raman Spectroscopy of Twisted Bilayer Graphene. *J. Carbon Res. C.* 2021, Vol. 7, p. 10.
89. M.M. LUCCHESE, F. STAVALE, E.H.M. FERREIRA, C. VILANI, M.V.O. MOUTINHO, R.B. CAPAZ, C.A. ACHETE, A. JORIO, Quantifying ion-induced defects and Raman relaxation length in graphene. *Carbon N. Y.* 2010, Vol. 48, p. 1592–1597. DOI 10.1016/j.carbon.2009.12.057.
90. A. JORIO, L.G. CANÇADO, L.M. MALARD, Vibrations in Graphene, in: : pp. 71–89 DOI 10.1017/9781316681619.006.
91. H. WANG, J.H. STRAIT, P.A. GEORGE, S. SHIVARAMAN, V.B. SHIELDS, M. CHANDRASHEKHAR, J. HWANG, F. RANA, M.G. SPENCER, C.S. RUIZ-VARGAS, J. PARK, Ultrafast relaxation dynamics of hot optical phonons in graphene. *Appl. Phys. Lett.* 2010, Vol. 96, no. 8, DOI 10.1063/1.3291615.
92. A. ECKMANN, A. FELTEN, A. MISHCHENKO, L. BRITNELL, R. KRUPKE, K.S. NOVOSELOV, C. CASIRAGHI, Probing the Nature of Defects in Graphene by Raman Spectroscopy. *Nano Lett.* 2012, Vol. 12, no. 8, p. 3925−3930. DOI 10.1021/nl300901a.
93. A.C. FERRARI, J. ROBERTSON, Interpretation of Raman spectra of disordered and amorphous carbon. *Phys. Rev. B.* 2000, Vol. 61, p. 95–107. DOI 10.1103/physrevb.61.14095.
94. A. ECKMANN, A. FELTEN, A. MISHCHENKO, L. BRITNELL, R. KRUPKE, K.S. NOVOSELOV, C. CASIRAGHI, Probing the Nature of Defects in Graphene by Raman Spectroscopy. *Nano Lett.* 2012, Vol. 12, p. 3925−3930. DOI 10.1021/nl300901a.
95. L.G. CANÇADO, A. JORIO, E.H.M. FERREIRA, F. STAVALE, C.A. ACHETE, R.B. CAPAZ, M.V.O. MOUTINHO, A. LOMBARDO, T.S. KULMALA, A.C. FERRARI, Quantifying defects in graphene via Raman spectroscopy at different excitation energies. *Nano Lett.* 2011, Vol. 11, no. 8, p. 3190–3196. DOI 10.1021/nl201432g.
96. J.W. CHIOU, S.C. RAY, S.I. PENG, C.H. CHUANG, B.Y. WANG, H.M. TSAI, C.W. PAO, H. LIN, Y.C. SHAO, Y.F. WANG, S.C. CHEN, W.F. POND, Y.C. YEH, C.W. CHEN, L. CHEN, K. CHEN, M. TSAI, A. KUMAR, A. GANGULY, P. PAPAKONSTANTINOU, H. YAMANE, N. KOSUGI, T. REGIER, L. LIU, T.K.

SHAM, Nitrogen-Functionalized Graphene Nano fl akes (GNFs:N): Tunable Photoluminescence and Electronic Structures. *J. Phys. Chem. C*. 2012, Vol. 116, p. 16251−16258. DOI 10.1021/jp303465u.

97. T. MOLDT, A. ECKMANN, P. KLAR, S. V. MOROZOV, A.A. ZHUKOV, K.S. NOVOSELOV, C. CASIRAGHI, High-Yield Production and Transfer of Graphene Flakes Obtained by Anodic Bonding. *ACS Nano*. 2011, Vol. 5, no. 10, p. 7700–7706. DOI 10.1021/nn202293f.
98. K. FAN, J. FU, X. LIU, X. WANG, Dependence of the fluorination intercalation of graphene toward high-quality fluorinated graphene formation. *Chem. Sci.* 2019, Vol. 10, p. 5546–5555. DOI 10.1039/c9sc00975b.
99. J. KWAK, Y. JO, S. PARK, N.Y. KIM, S. KIM, H. SHIN, Z. LEE, S.Y. KIM, S. KWON, Oxidation behavior of graphene-coated copper at intrinsic graphene defects of different origins. *Nat. Commun.* 2017, Vol. 8, p. 1549. DOI 10.1038/s41467-017-01814-8.
100. A. FELTEN, A. ECKMANN, J. PIREAUX, R. KRUPKE, C. CASIRAGHI, Controlled modification of mono- and bilayer graphene in O2 , H2 and CF4 plasmas. *Nanotechnology*. 2013, Vol. 24, p. 355705. DOI 10.1088/0957-4484/24/35/355705.
101. P. VENEZUELA, M. LAZZERI, F. MAURI, Theory of double-resonant Raman spectra in graphene: Intensity and line shape of defect-induced and two-phonon bands. *Phys. Rev. B*. 2011, Vol. 84, p. 035433. DOI 10.1103/PhysRevB.84.035433.
102. H.A. HAFEZ, S. KOVALEV, K. TIELROOIJ, M. BONN, M. GENSCH, Terahertz Nonlinear Optics of Graphene: From Saturable Absorption to High-Harmonics Generation. *Adv. Opt. Mater*. 2019, p. 1900771. DOI 10.1002/adom.201900771.
103. M. CHERGUI, Ultrafast Structural Dynamics of Biological Systems, Elsevier Ltd., DOI 10.1016/B978-0-12-374920-8.00123-5.
104. S. WINNERL, M. MITTENDORFF, C.K. JACOB, H. SCHNEIDER, M. HELM, T. WINZER, A. KNORR, E. MALIC, Ultrafast Processes in Graphene: From Fundamental Manybody Interactions to Device Applications. *Ann. Phys.* 2017, Vol. 529, p. 1700022. DOI 10.1002/andp.201700022.
105. J.M. IGLESIAS, M.J. MARTÍN, E. PASCUAL, R. RENGEL, Substrate influence on the early relaxation stages of photoexcited carriers in monolayer graphene. *Appl. Surf. Sci.* 2017, Vol. 424, DOI 10.1016/j.apsusc.2017.02.114.
106. P.A. OBRAZTSOV, M.G. RYBIN, A. V. TYURNINA, S. V. GARNOV, E.D. OBRAZTSOVA, A.N. OBRAZTSOV, Y.P. SVIRKO, Broadband Light-Induced Absorbance Change in Multilayer Graphene. *Nano Lett.* 2011, p. 1540–1545. DOI 10.1021/nl104303c.
107. J. SHANG, T. YU, G.G. GURZADYAN, Femtosecond energy relaxation in suspended graphene: phonon-assisted spreading of quasiparticle distribution. *Appl. Phys. B Lasers Opt.* 2012, Vol. 107, no. 1, p. 131–136. DOI 10.1007/s00340-011-4853-0.
108. K.J. TIELROOIJ, L. PIATKOWSKI, M. MASSICOTTE, A. WOESSNER, Q. MA, Y.

LEE, K.S. MYHRO, C.N. LAU, P. JARILLO-HERRERO, N.F. VAN HULST, F.H.L. KOPPENS, Generation of photovoltage in graphene on a femtosecond timescale through efficient carrier heating. *Nat. Nanotechnol.* 2015, Vol. 10, no. 5, p. 437–443. DOI 10.1038/nnano.2015.54.

109. K.-J. YEE, J.-H. KIM, M.H. JUNG, B.H. HONG, K.-J. KONG, Ultrafast modulation of optical transitions in monolayer and multilayer graphene. *Carbon N. Y.* 2011, Vol. 49, no. 14, p. 4781–4785. DOI 10.1016/j.carbon.2011.06.088.
110. H. WANG, J.H. STRAIT, P.A. GEORGE, S. SHIVARAMAN, V.B. SHIELDS, M. CHANDRASHEKHAR, J. HWANG, F. RANA, M.G. SPENCER, C.S. RUIZ-VARGAS, J. PARK, H. WANG, J.H. STRAIT, P.A. GEORGE, S. SHIVARAMAN, V.B. SHIELDS, M. CHANDRASHEKHAR, J. HWANG, F. RANA, M.G. SPENCER, C.S. RUIZ-VARGAS, J. PARK, Ultrafast relaxation dynamics of hot optical phonons in graphene. *Appl. Phys. Lett.* 2010, Vol. 96, no. 8, p. 081917. DOI 10.1063/1.3291615.
111. K.J. TIELROOIJ, J.C.W. SONG, S.A. JENSEN, A. CENTENO, A. PESQUERA, A.Z. ELORZA, M. BONN, L.S. LEVITOV, F.H.L. KOPPENS, Photoexcitation cascade and multiple hot-carrier generation in graphene. *Nat. Phys.* 2013, Vol. 9, no. 4, p. 1–5. DOI 10.1038/nphys2564.
112. J. KUSUMA, R.G. BALAKRISHNA, S. PATIL, M.S. JYOTHI, H.R. CHANDAN, R. SHWETHARANI, Exploration of graphene oxide nanoribbons as excellent electron conducting network for third generation solar cells. *Sol. Energy Mater. Sol. Cells*. 2018, Vol. 183, p. 211–219. DOI 10.1016/j.solmat.2018.01.039.
113. L. LIU, K. ZHENG, Y. YAN, Z. CAI, S. LIN, X. HU, Graphene Aerogels Enhanced Phase Change Materials prepared by one-pot method with high thermal conductivity and large latent energy storage. *Sol. Energy Mater. Sol. Cells*. 2018, Vol. 185, p. 487–493. DOI 10.1016/j.solmat.2018.06.005.
114. S. SAADI, B. NAZARI, Recent developments and applications of nanocomposites in solar cells: a review. *J. Compos. Compd.* 2019, Vol. 2, p. 41–50. DOI 10.29252/jcc.1.1.7.
115. X. LI, J. YU, S. WAGEH, A.A. AL-GHAMDI, J. XIE, Graphene in Photocatalysis: A Review. *Small*. 2016, Vol. 12, no. 48, p. 6640–6696. DOI 10.1002/smll.201600382.
116. S. ESKANDARINEZHAD, R. KHOSRAVI, M. AMARZADEH, P. MONDAL, F.J.C.M. FILHO, Application of different nanocatalysts in industrial effluent treatment: A review. *J. Compos. Compd.* 2021, Vol. 3, p. 43–56. DOI 10.52547/jcc.3.1.5.
117. J. KUSUMA, R.G. BALAKRISHNA, S. PATIL, M.S. JYOTHI, H.R. CHANDAN, R. SHWETHARANI, Enhanced X-ray photon response in solution-synthesized CsPbBr3 nanoparticles wrapped by reduced graphene oxide. *Sol. Energy Mater. Sol. Cells*. 2018, Vol. 183, p. 211–219.
118. G. SOAVI, S.D. CONTE, C. MANZONI, D. VIOLA, A. NARITA, Y. HU, X. FENG, U. HOHENESTER, E. MOLINARI, D. PREZZI, K. MULLEN, G. CERULLO, Exciton–exciton annihilation and biexciton stimulated emission in graphene

nanoribbons. *Nat. Commun.* 2016, DOI 10.1038/ncomms11010.
119. A. DAS, S. PISANA, B. CHAKRABORTY, S. PISCANEC, S.K. SAHA, U. V. WAGHMARE, K.S. NOVOSELOV, H.R. KRISHNAMURTHY, A.K. GEIM, A.C. FERRARI, A.K. SOOD, Monitoring dopants by Raman scattering in an electrochemically top-gated graphene transistor. *Nat. Nanotechnol.* 2008, Vol. 3, no. 4, p. 210–215. DOI 10.1038/nnano.2008.67.
120. T. LI, L. LUO, M. HUPALO, J. ZHANG, M.C. TRINGIDES, J. SCHMALIAN, J. WANG, Femtosecond population inversion and stimulated emission of dense dirac fermions in graphene. *Phys. Rev. Lett.* 2012, Vol. 108, no. 16, p. 1–5. DOI 10.1103/PhysRevLett.108.167401.
121. S. PARUI, M. RIBEIRO, A. ATXABAL, R. LLOPIS, F. CASANOVA, L.E. HUESO, Graphene as an electrode for solution-processed electron-transporting organic transistors. *Nanoscale*. 2017, Vol. 9, no. 29, p. 10178–10185. DOI 10.1039/c7nr01007a.
122. S. ZHAO, L. RONDIN, G. DELPORT, C. VOISIN, U. BESER, Y. HU, X. FENG, K. MÜLLEN, A. NARITA, S. CAMPIDELLI, J.S. LAURET, Fluorescence from graphene nanoribbons of well-defined structure. *Carbon N. Y.* 2017, Vol. 119, p. 235–240. DOI 10.1016/j.carbon.2017.04.043.
123. G. ANAGNOSTOPOULOS, P.-N. PAPPAS, Z. LI, I.A. KINLOCH, R.J. YOUNG, K.S. NOVOSELOV, C.Y. LU, N. PUGNO, J. PARTHENIOS, C. GALIOTIS, K. PAPAGELIS, Mechanical Stability of Flexible Graphene-Based Displays. *ACS Appl. Mater. Interfaces*. 2016, Vol. 8, no. 34, p. 22605–22614. DOI 10.1021/acsami.6b05227.
124. S. TKACHEV, M. MONTEIRO, J. SANTOS, E. PLACIDI, M. BEN HASSINE, P. MARQUES, P. FERREIRA, P. ALPUIM, A. CAPASSO, Environmentally Friendly Graphene Inks for Touch Screen Sensors. *Adv. Funct. Mater.* 2021, Vol. 31, p. 2103287. DOI 10.1002/adfm.202103287.
125. E. ASADI, A.F. CHIMEH, A.H.V. TAHMORSATI, S. HOSSEINI, S. RAHIMI, B. SARKHOSH, L. BAZLI, R. BASHIRI, A review of clinical applications of graphene quantum dot-based composites. *J. Compos. Compd.* 2019, Vol. 2, p. 31–40. DOI 10.29252/jcc.1.1.6.
126. X. ZHANG, Q. JING, S. AO, G.F. SCHNEIDER, D. KIREEV, Z. ZHANG, W. FU, Ultrasensitive Field-Effect Biosensors Enabled by the Unique Electronic Properties of Graphene. *Small*. 2020, Vol. 16, p. 1902820. DOI 10.1002/smll.201902820.
127. S. PANDIT, K. GASKA, R. KÁDÁR, I. MIJAKOVIC, Graphene-Based Antimicrobial Biomedical Surfaces. *ChemPhysChem*. 2021, Vol. 22, p. 250–263. DOI 10.1002/cphc.202000769.
128. N.I. ZHELUDEV, Y.S. KIVSHAR, From metamaterials to metadevices. *Nat. Mater.* 2012, Vol. 11, no. 11, p. 917–924. DOI 10.1038/nmat3431.
129. M.W. GRAHAM, S.-F. SHI, Z. WANG, D.C. RALPH, J. PARK, P.L. MCEUEN, Transient Absorption and Photocurrent Microscopy Show That Hot Electron Supercollisions Describe the Rate-Limiting Relaxation Step in Graphene. *Nano Lett.* 2013, Vol. 13, no. 11, p. 5497–5502. DOI 10.1021/nl4030787.
130. G. YU, X. LIU, G. XING, S. CHEN, C.F. NG, X. WU, E.K.L. YEOW, W.S. LEW,

T.C. SUM, Spatially-Resolved Ultrafast Optical Spectroscopy of Polymer-Grafted Residues on CVD Graphene. *J. Phys. Chem. C*. 2014, Vol. 118, no. 1, p. 708–713. DOI 10.1021/jp406675r.

131. L. BROERS, L. MATHEY, Detecting light-induced Floquet band gaps of graphene via trARPES. *Phys. Rev. Res.* 2022, Vol. 4, p. 013057. DOI 10.1103/PhysRevResearch.4.013057.
132. H. LI, M.I.B. UTAMA, S. WANG, W. ZHAO, S. ZHAO, X. XIAO, Y. JIANG, L. JIANG, T. TANIGUCHI, K. WATANABE, A. WEBER-BARGIONI, A. ZETTL, F. WANG, Global Control of Stacking-Order Phase Transition by Doping and Electric Field in Few-Layer Graphene. *Nano Lett.* 2020, Vol. 20, p. 3106−3112. DOI 10.1021/acs.nanolett.9b05092.
133. H. GUO, R. ZHANG, H. LI, X. WANG, H. LU, K. QIAN, G. LI, L. HUANG, X. LIN, Y.-Y. ZHANG, H. DING, S. DU, S.T. PANTELIDES, H.-J. GAO, Sizable Band Gap in Epitaxial Bilayer Graphene Induced by Silicene Intercalation. *Nano Lett.* 2020, Vol. 20, p. 2674−2680. DOI 10.1021/acs.nanolett.0c00306.
134. P. ROZEL, D. RADZIUK, L. MIKHNAVETS, E. KHOKHLOV, V. SHIRIPOV, I. MATOLÍNOVÁ, V. MATOLÍN, A. BASAEV, N. KARGIN, V. LABUNOV, Properties of Nitrogen/Silicon Doped Vertically Oriented Graphene Produced by ICP CVD Roll-to-Roll Technology. *Coatings*. 2019, Vol. 9, no. 1, p. 60 (1-24). DOI 10.3390/coatings9010060.
135. Y. MU, M. HAN, J. LI, J. LIANG, J. YU, Growing vertical graphene sheets on natural graphite for fast charging lithium-ion batteries. *Carbon N. Y.* 2021, Vol. 173, p. 477–484. DOI 10.1016/j.carbon.2020.11.027.
136. L. WANG, W. ZHANG, S. SAMAVAT, D. DEGANELLO, K.S. TENG, Vertically Aligned Graphene Prepared by Photonic Annealing for Ultrasensitive Biosensors. *ACS Appl. Mater. Interfaces*. 2020, Vol. 12, p. 35328−35336. DOI 10.1021/acsami.0c08036.
137. S.A. EVLASHIN, Y.M. MAKSIMOV, P. V. DYAKONOV, A.A. PILEVSKY, K.I. MASLAKOV, Y.A. MANKELEVICH, E.N. VORONINA, S. V. VAVILOV, A.A. PAVLOV, E. V. ZENOVA, I.S. AKHATOV, N. V. SUETIN, N-Doped Carbon NanoWalls for Power Sources. *Sci. Rep.* 2019, Vol. 9, p. 6716. DOI 10.1038/s41598-019-43001-3.
138. J. HAN, Y. MA, M. WANG, L. LI, Z. TONG, L. XIAO, S. JIA, X. CHEN, Oxygen-Assisted Trimming Growth of Ultrahigh Vertical Graphene Films in a PECVD Process for Superior Energy Storage. *ACS Appl. Mater. Interfaces*. 2021, Vol. 13, p. 12400−12407. DOI 10.1021/acsami.1c00544.
139. C. DENG, L. LAN, P. HE, C. DING, B. CHEN, W. ZHENG, X. ZHAO, W. CHEN, X. ZHONG, M. LI, H. TAO, J. PENGA, Y. CAO, High-performance capacitive strain sensors with highly stretchable vertical graphene electrodes. *J. Mater. Chem. C*. 2020, Vol. 8, p. 5541–5546. DOI 10.1039/d0tc00491j.
140. C. DENG, P. GAO, L. LAN, P. HE, X. ZHAO, W. ZHENG, Ultrasensitive and Highly Stretchable Multifunctional Strain Sensors with Timbre-Recognition Ability Based on Vertical Graphene. *Adv. Funct. Mater.* 2019, Vol. 29, p. 1907151. DOI 10.1002/adfm.201907151.
141. J. SCREMIN, I.V.J. DOS SANTOS, J.P. HUGHES, A.G.-M. FERRARI, E.

VALDERRAMA, W. ZHENG, X. ZHONG, X. ZHAO, E.J.R. SARTORI, R.D. CRAPNELL, S.J. ROWLEY-NEALE, C.E. BANKS, Platinum nanoparticle decorated vertically aligned graphene screen-printed electrodes: electrochemical characterisation and exploration towards the hydrogen evolution reaction. *Nanoscale*. 2020, Vol. 12, p. 18214–18224. DOI 10.1039/d0nr04336b.

142. J. LI, Z. LIU, Q. GUO, S. YANG, A. XU, Z. WANG, G. WANG, Y. WANG, D. CHEN, G. DING, Controllable growth of vertically oriented graphene for high sensitivity gas detection. *J. Mater. Chem. C*. 2019, Vol. 7, no. 20, p. 5995–6003. DOI 10.1039/c9tc01246j.
143. Š. MEŠKINIS, R. GUDAITIS, A. VASILIAUSKAS, S. TAMULEVIČIUS, G. NIAURA, Multiwavelength Raman Scattering Spectroscopy Study of Graphene Synthesized on Si(100) and SiO2 by Microwave Plasma-Enhanced Chemical Vapor Deposition. *Phys. Status Solidi - Rapid Res. Lett.* 2019, Vol. 1900462, no. 100, p. 3–7. DOI 10.1002/pssr.201900462.
144. IPALAS, CYRANNUS - Innovative plasma systems gmbh. (n.d.). www.cyrannus.com.
145. L. TAO, J. LEE, M. HOLT, H. CHOU, S.J. MCDONNELL, D.A. FERRER, M.G. BABENCO, R.M. WALLACE, S.K. BANERJEE, R.S. RUOFF, D. AKINWANDE, Uniform Wafer-Scale Chemical Vapor Deposition of Graphene on Evaporated Cu (111) Film with Quality Comparable to Exfoliated Monolayer. *J. Phys. Chem. C*. 2012, Vol. 116, p. 24068–24074. DOI 10.1021/jp3068848.
146. R. GUDAITIS, A. LAZAUSKAS, Š. JANKAUSKAS, Š. MEŠKINIS, Catalyst-Less and Transfer-Less Synthesis of Graphene on Si(100) Using Direct Microwave Plasma Enhanced Chemical Vapor Deposition and Protective Enclosures. *Materials (Basel)*. 2020, Vol. 13, no. 24, p. 5630. DOI 10.3390/ma13245630.
147. Graphenea Monolayer Graphene film on Quartz. (n.d.). https://www.graphenea.com/collections/buy-graphene-films/products/monolayer-graphene-on-quartz-4-wafer.
148. X. YANG, M. YAN, Removing contaminants from transferred CVD graphene. *Nano Res.* 2020, Vol. 13, no. 3, p. 599–610. DOI 10.1007/s12274-020-2671-6.
149. B. ZHUANG, S. LI, S. LI, J. YIN, Ways to eliminate PMMA residues on graphene dd superclean graphene. *Carbon N. Y.* 2021, Vol. 173, p. 609–636. DOI 10.1016/j.carbon.2020.11.047.
150. S. PENG, Z. JIN, P. MA, D. ZHANG, J. SHI, J. NIU, X. WANG, S. WANG, M. LI, X. LIU, T. YE, Y. ZHANG, Z. CHEN, G. YU, The sheet resistance of graphene under contact and its effect on the derived specific contact resistivity. *Carbon N. Y.* 2015, Vol. 82, p. 500–505. DOI 10.1016/j.carbon.2014.11.001.
151. D. PECKUS, H. RONG, L. STANKEVIČIUS, M. JUODĖNAS, S. TAMULEVIČIUS, T. TAMULEVIČIUS, J. HENZIE, Hot Electron Emission Can Lead to Damping of Optomechanical Modes in Core−Shell Ag@TiO2 Nanocubes. *J. Phys. Chem. C*. 2017, Vol. 121, p. 24159–24167. DOI 10.1021/acs.jpcc.7b06667.

152. D. PECKUS, H. RONG, L. STANKEVIČIUS, M. JUODĖNAS, S. TAMULEVIČIUS, T. TAMULEVIČIUS, J. HENZIE, Hot Electron Emission Can Lead to Damping of Optomechanical Modes in Core-Shell Ag@TiO2 Nanocubes. *J. Phys. Chem. C*. 2017, Vol. 121, no. 43, p. 24159–24167. DOI 10.1021/acs.jpcc.7b06667.
153. C. OPHUS, A. SHEKHAWAT, H. RASOOL, A. ZETTL, Large-scale experimental and theoretical study of graphene grain boundary structures. *Phys. Rev. B - Condens. Matter Mater. Phys.* 2015, Vol. 92, no. 20, p. 205402. DOI 10.1103/PhysRevB.92.205402.
154. N.M. SANTHOSH, G. FILIPIČ, E. TATAROVA, O. BARANOV, H. KONDO, M. SEKINE, M. HORI, K. (KEN) OSTRIKOV, U. CVELBAR, Oriented Carbon Nanostructures by Plasma Processing: Recent Advances and Future Challenges. *Micromachines*. 2018, Vol. 9, no. 11, p. 565. DOI 10.3390/mi9110565.
155. M.Y. ZHU, R.A. OUTLAW, M. BAGGE-HANSEN, H.J. CHEN, D.M. MANOS, Enhanced field emission of vertically oriented carbon nanosheets synthesized by C2H2/H2 plasma enhanced CVD. *Carbon N. Y.* 2011, Vol. 49, no. 7, p. 2526–2531. DOI 10.1016/j.carbon.2011.02.024.
156. S. GHOSH, K. GANESAN, S.R. POLAKI, T. MATHEWS, S. DHARA, M. KAMRUDDIN, A.K. TYAGI, Influence of substrate on nucleation and growth of vertical graphene nanosheets. *Appl. Surf. Sci.* 2015, Vol. 349, p. 576–581. DOI 10.1016/j.apsusc.2015.05.038.
157. J. ZHAO, M. SHAYGAN, J. ECKERT, M. MEYYAPPAN, M.H. RUMMELI, A Growth Mechanism for Free-Standing Vertical Graphene. *Nano Lett.* 2014, Vol. 14, p. 3064–3071. DOI 10.1021/nl501039c.
158. Y. QI, B. DENG, X. GUO, S. CHEN, J. GAO, T. LI, Z. DOU, H. CI, J. SUN, Z. CHEN, R. WANG, L. CUI, X. CHEN, K. CHEN, H. WANG, S. WANG, P. GAO, M.H. RUMMELI, H. PENG, Y. ZHANG, Z. LIU, Switching Vertical to Horizontal Graphene Growth Using Faraday Cage-Assisted PECVD Approach for High-Performance Transparent Heating Device. *Adv. Mater.* 2018, Vol. 30, no. 8, p. 1704839 (1-9). DOI 10.1002/adma.201704839.
159. A. MARINOIU, M. RACEANU, M. ANDRULEVICIUS, A. TAMULEVICIENE, T. TAMULEVICIUS, S. NICA, D. BALA, M. VARLAM, Low-cost preparation method of well dispersed gold nanoparticles on reduced graphene oxide and electrocatalytic stability in PEM fuel cell. *Arab. J. Chem.* 2020, Vol. 13, p. 3585–3600. DOI 10.1016/j.arabjc.2018.12.009.
160. I. V. KOMISSAROV, N.G. KOVALCHUK, V.A. LABUNOV, K. V. GIREL, O. V. KOROLIK, M.S. TIVANOV, A. LAZAUSKAS, M. ANDRULEVIČIUS, T. TAMULEVIČIUS, V. GRIGALIŪNAS, Š. MEŠKINIS, S. TAMULEVIČIUS, S.L. PRISCHEPA, Nitrogen-doped twisted graphene grown on copper by atmospheric pressure CVD from a decane precursor. *Beilstein J. Nanotechnol.* 2017, Vol. 8, p. 145–158. DOI 10.3762/bjnano.8.15.
161. L. PEDRAZZETTI, L. NOBILI, L. MAGAGNIN, R. BERNASCONI, A. LUCOTTI, P. SOLTANI, A. MEZZI, S. KAČIULIS, Growth and characterization of ultrathin carbon films on electrodeposited Cu and Ni. *Surf. Interface Anal.* 2017, p. 1–

7. DOI 10.1002/sia.6281.
162. R. Lv, Q. Li, A.R. Botello-Méndez, T. Hayashi, B. Wang, A. Berkdemir, Q. Hao, A.L. Eléas, R. Cruz-Silva, H.R. Gutiérrez, Y.A. Kim, H. Muramatsu, J. Zhu, M. Endo, H. Terrones, J.C. Charlier, M. Pan, M. Terrones, Nitrogen-doped graphene: Beyond single substitution and enhanced molecular sensing. *Sci. Rep.* 2012, Vol. 2, p. 1–8. DOI 10.1038/srep00586.
163. I.A. Verzhbitskiy, M. De Corato, A. Ruini, E. Molinari, A. Narita, Y. Hu, M.G. Schwab, M. Bruna, D. Yoon, S. Milana, X. Feng, K. Mullen, A.C. Ferrari, C. Casiraghi, D. Prezzi, Raman Fingerprints of Atomically Precise Graphene Nanoribbons. *Nano Lett.* 2016, Vol. 16, p. 3442–3447. DOI 10.1021/acs.nanolett.5b04183.
164. A. Eckmann, A. Felten, A. Mishchenko, L. Britnell, R. Krupke, K.S. Novoselov, C. Casiraghi, Probing the Nature of Defects in Graphene by Raman Spectroscopy. *Nano Lett.* 2012, Vol. 12, p. 3925–3930. DOI 10.1021/nl300901a.
165. I. Childres, L.A. Jauregui, W. Park, H. Cao, Y.P. Chen, Raman spectroscopy of graphene and related materials. *New Dev. Phot. Mater. Res.* 2013,.
166. F. Banhart, J. Kotakoski, A. V. Krasheninnikov, Structural defects in graphene. *ACS Nano*. 2011, Vol. 5, no. 1, p. 26–41. DOI 10.1021/nn102598m.
167. R. Sharma, N. Chadha, P. Saini, Determination of defect density, crystallite size and number of graphene layers in graphene analogues using X-ray diffraction and Raman spectroscopy. *Indian J. Pure Appl. Phys.* 2017, Vol. 55, no. September, p. 625–629.
168. A.C. Ferrari, D.M. Basko, Raman spectroscopy as a versatile tool for studying the properties of graphene. *Nat. Nanotechnol.* 2013, Vol. 8, no. 4, p. 235–246. DOI 10.1038/nnano.2013.46.
169. F. Tuinstra, J.L. Koenig, Raman Spectrum of Graphite. *J. Chem. Phys.* 1970, Vol. 53, p. 1126–1130. DOI 10.1063/1.1674108.
170. G. Bepete, D. Voiry, M. Chhowalla, Z. Chiguvare, N.J. Coville, Incorporation of small BN domains in graphene during CVD using methane, boric acid and nitrogen gas. *Nanoscale*. 2013, Vol. 5, no. 14, p. 6552–6557. DOI 10.1039/c3nr01699d.
171. J. Hong, M.K. Park, E.J. Lee, D. Lee, D.S. Hwang, S. Ryu, Origin of new broad raman D and G Peaks in annealed graphene. *Sci. Rep.* 2013, Vol. 3, p. 1–5. DOI 10.1038/srep02700.
172. D.G. Papageorgiou, I.A. Kinloch, R.J. Young, Mechanical properties of graphene and graphene-based nanocomposites. *Prog. Mater. Sci.* 2017, Vol. 90, p. 75–127. DOI 10.1016/j.pmatsci.2017.07.004.
173. H. Mi, Z. Ma, James P. Blanchard, Raman Spectroscopy for Monitoring Strain on Graphene and Oxidation Corrosion on Nuclear Claddings, in: Khan Maaz (Ed.), Raman Spectrosc. Appl., IntechOpen, : pp. 123–142 DOI 10.5772/57353.

174. S. HUH, J. PARK, K.S. KIM, B.H. HONG, S. BIN KIM, Selective n-Type Doping of Graphene by Photo-patterned Gold Nanoparticles. *ACS Nano*. 2011, Vol. 5, no. 5, p. 3639–3644.
175. X. ZHENG, W. CHEN, G. WANG, Y. YU, S. QIN, J. FANG, F. WANG, X. ZHANG, The Raman redshift of graphene impacted by gold nanoparticles. *AIP Adv.* 2015, no. January, p. 057133. DOI 10.1063/1.4921316.
176. G.M. BHALERAO, M.K. SINGH, H. GHOSH, Optical redshift in the Raman scattering spectra of Fe-doped multiwalled carbon nanotubes : Experiment and theory. *Phys. Rev. B.* 2012, Vol. 86, p. 125419. DOI 10.1103/PhysRevB.86.125419.
177. M.W. IQBAL, M.Z. IQBAL, M.F. KHAN, X. JIN, Modification of the structural and electrical properties of graphene layers by Pt adsorbates. *Sci. Technol. Adv. Mater.* 2014, Vol. 15, p. 055002. DOI 10.1088/1468-6996/15/5/055002.
178. O. FRANK, J. VEJPRAVOVA, V. HOLY, L. KAVAN, M. KALBAC, Interaction between graphene and copper substrate: The role of lattice orientation. *Carbon N. Y.* 2014, Vol. 68, p. 440–451. DOI 10.1016/j.carbon.2013.11.020.
179. A. REINA, X. JIA, J. HO, D. NEZICH, H. SON, V. BULOVIC, M.S. DRESSELHAUS, J. KONG, Large Area, Few-Layer Graphene Films on Arbitrary Substrates by Chemical Vapor Deposition. *Nano Lett.* 2009, Vol. 9, no. 1, p. 30–35. DOI 10.1021/nl801827v.
180. D.-H. CHAE, T. UTIKAL, S. WEISENBURGER, H. GIESSEN, K. V. KLITZING, M. LIPPITZ, J. SMET, Excitonic Fano Resonance in Free-Standing Graphene. *Nano Lett.* 2011, Vol. 11, no. 3, p. 1379–1382. DOI 10.1021/nl200040q.
181. J. SHANG, Z. LUO, C. CONG, J. LIN, T. YU, G.G. GURZADYAN, Femtosecond UV-pump/visible-probe measurements of carrier dynamics in stacked graphene films. *Appl. Phys. Lett.* 2010, Vol. 97, p. 163103. DOI 10.1063/1.3504704.
182. T. KOYAMA, K. MIZUTANI, H. AGO, H. KISHIDA, Two-Step Excitation Triggered by One-Photon Absorption on Linear Dispersion in Monolayer Graphene. *J. Phys. Chem. C.* 2016, Vol. 120, no. 20, p. 11225–11229. DOI 10.1021/acs.jpcc.6b01490.
183. J. SHANG, Z. LUO, C. CONG, J. LIN, T. YU, G.G. GURZADYAN, Femtosecond UV-pump/visible-probe measurements of carrier dynamics in stacked graphene films. *Appl. Phys. Lett.* 2010, Vol. 97, no. 16, p. 95–98. DOI 10.1063/1.3504704.
184. D. BRIDA, A. TOMADIN, C. MANZONI, Y.J. KIM, A. LOMBARDO, S. MILANA, R.R. NAIR, K.S. NOVOSELOV, A.C. FERRARI, G. CERULLO, M. POLINI, Ultrafast collinear scattering and carrier multiplication in graphene. *Nat. Commun.* 2013, Vol. 4, p. 1–9. DOI 10.1038/ncomms2987.
185. L.I. JOHANSSON, R. ARMIENTO, J. AVILA, C. XIA, S. LORCY, I.A. ABRIKOSOV, M.C. ASENSIO, C. VIROJANADARA, Multiple p-bands and Bernal stacking of multilayer graphene on C-face SiC, revealed by nano-Angle Resolved Photoemission. *Sci. Rep.* 2014, Vol. 4, p. 1–6. DOI 10.1038/srep04157.
186. K.F. MAK, M.Y. SFEIR, J.A. MISEWICH, T.F. HEINZA, The evolution of

electronic structure in few-layer graphene revealed by optical spectroscopy. *Proc. Natl. Acad. Sci. U. S. A.* 2010, Vol. 107, no. 34, p. 14999–15004. DOI 10.1073/pnas.1004595107.

187. H. MIN, A.H. MACDONALD, Electronic structure of multilayer graphene. *Prog. Theor. Phys. Suppl.* 2008, Vol. 176, p. 227–252. DOI 10.1143/PTPS.176.227.
188. R. YAGI, T. HIRAHARA, R. EBISUOKA, T. NAKASUGA, S. TAJIMA, K. WATANABE, T. TANIGUCHI, Low-energy band structure and even-odd layer number effect in AB-stacked multilayer graphene. *Sci. Rep.* 2018, Vol. 8, no. 1, p. 1–7. DOI 10.1038/s41598-018-31291-y.
189. M. BREUSING, S. KUEHN, T. WINZER, E. MALIĆ, F. MILDE, N. SEVERIN, J.P. RABE, C. ROPERS, A. KNORR, T. ELSAESSER, Ultrafast nonequilibrium carrier dynamics in a single graphene layer. *Phys. Rev. B - Condens. Matter Mater. Phys.* 2011, Vol. 83, no. 15, p. 1–4. DOI 10.1103/PhysRevB.83.153410.
190. F. RANA, P.A. GEORGE, J.H. STRAIT, J. DAWLATY, S. SHIVARAMAN, M. CHANDRASHEKHAR, M.G. SPENCER, Carrier recombination and generation rates for intravalley and intervalley phonon scattering in graphene. *Phys. Rev. B.* 2009, Vol. 79, no. 11, p. 115447. DOI 10.1103/PhysRevB.79.115447.
191. K.J. YEE, J.H. KIM, M.H. JUNG, B.H. HONG, K.J. KONG, Ultrafast modulation of optical transitions in monolayer and multilayer graphene. *Carbon N. Y.* 2011, Vol. 49, no. 14, p. 4781–4785. DOI 10.1016/j.carbon.2011.06.088.
192. S. ZHU, H. ZHANG, J. WANG, B. ZHAO, D. WAN, Research on the defect types transformation induced by growth temperature of vertical graphene nanosheets. *J. Alloys Compd.* 2019, Vol. 781, p. 1048–1053. DOI 10.1016/j.jallcom.2018.12.075.
193. P. CHIU, Y.-C. LIN, C.-C. LU, C.-H. YEH, C. JIN, K. SUENAGA, P. CHIU, Y.-C. LIN, C.-C. LU, C.-H. YEH, C. JIN, K. SUENAGA, P. CHIU, Graphene Annealing: How Clean Can It Be? *Nano Lett.* 2012, Vol. 12, no. 1, p. 414–419. DOI 10.1021/nl203733r.
194. S.R. POLAKI, G. SAHOO, P. ANEES, N.G. KRISHNA, M. KAMRUDDIN, S. DHARA, Engineering the edge-terminations and defect-density to enhance the electrochemical capacitance performance of vertical graphene nanosheets. *Appl. Surf. Sci.* 2021, Vol. 545, p. 149045. DOI 10.1016/j.apsusc.2021.149045.
195. J. JIANG, R. PACHTER, F. MEHMOOD, A.E. ISLAM, B. MARUYAMA, J.J. BOECKL, A Raman spectroscopy signature for characterizing defective single-layer graphene: Defect-induced I(D)/I(D') intensity ratio by theoretical analysis. *Carbon N. Y.* 2015, Vol. 90, p. 53–62. DOI 10.1016/j.carbon.2015.03.049.
196. A. KAUSHAL, S.K. DHAWAN, V. SINGH, Determination of crystallite size, number of graphene layers and defect density of graphene oxide (GO) and reduced graphene oxide (RGO). *AIP Conf. Proc.* 2019, Vol. 2115, no. July, p. 1–5. DOI 10.1063/1.5112945.
197. S. ALANCHERRY, M.V. JACOB, K. PRASAD, J. JOSEPH, O. BAZAKA, R.

NEUPANE, O.K. VARGHESE, O. BARANOV, S. XU, I. LEVCHENKO, K. BAZAKA, Tuning and fine morphology control of natural resource-derived vertical graphene. *Carbon N. Y.* 2020, Vol. 159, p. 668–685. DOI 10.1016/j.carbon.2019.10.060.

198. T.E. SARASWATI, U.H. SETIAWAN, M.R. IHSAN, I. ISNAENI, Y. HERBANI, The Study of the Optical Properties of C60 Fullerene in Different Organic Solvents. *Open Chem.* 2020, Vol. 17, no. 1, p. 1198–1212. DOI 10.1515/chem-2019-0117.
199. A. ROCH, L. STEPIEN, T. ROCH, I. DANI, C. LEYENS, O. JOST, A. LESON, Optical absorption spectroscopy and properties of single walled carbon nanotubes at high temperature. *Synth. Met.* 2014, Vol. 197, p. 182–187. DOI 10.1016/j.synthmet.2014.09.016.
200. Y. HUANG, D.L. ELDER, A.L. KWIRAM, S.A. JENEKHE, A.K.Y. JEN, L.R. DALTON, C.K. LUSCOMBE, Organic Semiconductors at the University of Washington: Advancements in Materials Design and Synthesis and toward Industrial Scale Production. *Adv. Mater.* 2019, p. 1904239 (1-23). DOI 10.1002/adma.201904239.
201. J. DU, D. ZHANG, X. WANG, H. JIN, W. ZHANG, B. TONG, Y. LIU, P.L. BURN, H.-M. CHENG, W. REN, Extremely efficient flexible organic solar cells with a graphene transparent anode: Dependence on number of layers and doping of graphene. *Carbon N. Y.* 2021, Vol. 171, p. 350–358. DOI 10.1016/j.carbon.2020.08.038.
202. S. MARAGKAKI, K. SAVVA, E. STRATAKIS, Advanced Photonic Processes for Photovoltaic, Energy Storage, and Environmental Systems. *Adv. Sustain. Syst.* 2021, Vol. 5, p. 2000237. DOI 10.1002/adsu.202000237.

CURRICULUM VITAE

Name, surname: Erika Rajackaitė
Email: erika.rajackaite@ktu.lt

Education:
Studies at Kaunas University of Technology
2008–2012 Bachelor's degree in Physics
2012–2014 Master's degree in Physics

Professional experience:
Participation in research projects at the Institute of Materials Science of Kaunas University of Technology
2013–2014 Project laboratory assistant
2017–2017 Project engineer
2017–2022 Project junior researcher
2018 – currently Engineer

Areas of scientific interest:
Thin film technologies, graphene synthesis, Raman scattering spectroscopy, pump-probe spectroscopy

LIST OF PUBLICATIONS, CONFERENCES AND INTERNSHIPS

Publications related to the dissertation

A1. Erika Rajackaitė, Domantas Peckus, Rimantas Gudaitis, Tomas Tamulevičius, Šarūnas Meškinis, Sigitas Tamulevičius. The Evolution of Properties with Deposition Time of Vertical Graphene Nanosheets Produced by Microwave Plasma Enhanced Chemical Vapour Deposition. *Surfaces and Interfaces* Vol 27, 101529, 2021. DOI: 10.1016/j.surfin.2021.101529. [IF: 4.837 (2020) Q1].

A2. Erika Rajackaitė, Domantas Peckus, Rimantas Gudaitis, Mindaugas Andrulevičius, Tomas Tamulevičius, Dmytro Volyniuk, Šarūnas Meškinis, Sigitas Tamulevičius. Transient absorption spectroscopy as a promising optical tool for measure of quality of graphene layers deposited by microwave plasma. *Surface and Coatings Technology*, Vol. 395, 125887, 2020. DOI: 10.1016/j.surfcoat.2020.125887. [IF: 4.158 (2020) Q1].

A3. Maximenko A. A., Rajackaitė E., Meškinis Š., Tamulevičius T., Tamulevičius S., Kharchanka A.A., Fedotov A.K., Fedotova Ju.A. Electrical transport properties of a carbon nanostructure obtained by plasma-enhanced chemical vapor deposition during thermal cycling. *Journal of the Belarusian State University. Physics*. 2020. Vol. 3, 89–96. In Russian. DOI: 10.33581/2520-2243-2020-3-89-96.

Other publications

1. Domantas Peckus, Šarūnas Meškinis, Andrius Vasiliauskas, Erika Rajackaitė, Mindaugas Andrulevičius, Vitoldas Kopustinskas, Sigitas Tamulevičius. Structure and optical properties of diamond like carbon films containing aluminium and alumina. *Applied Surface Science*, Vol. 529, 147040, 2020. DOI: 10.1016/j.apsusc.2020.147040. [IF: 6.707 (2020) Q1].
2. Domantas Peckus, Joel Henzie, Tomas Tamulevičius, Mindaugas Andrulevičius, Algirdas Lazauskas, Erika Rajackaitė, Šarūnas Meškinis, Sigitas Tamulevičius. Ultrafast relaxation dynamics of aluminum nanoparticles in solution. *Physica E: Low-dimensional Systems and Nanostructures*, Vol. 117, 113795, spec. iss., 2020. DOI: 10.1016/j.physe.2019.113795. [IF: 3.382 (2020) Q1].

Conference contributions related to the dissertation (presented by the author)

1. Erika Rajackaitė, Domantas Peckus, Rimantas Gudaitis, Tomas Tamulevičius, Šarūnas Meškinis, Sigitas Tamulevičius. Influence of the Deposition Duration on the Properties of Vertical Graphene Nanosheets Synthesized by Microwave Plasma Enhanced Chemical Vapour Deposition Technique. 4th International Conference "Nanotechnology and Innovation in the Baltic Sea Region 2021", virtual conference, 4–6 August, 2021.
2. Erika Rajackaitė, Rimantas Gudaitis, Domantas Peckus, Tomas Tamulevičius, Šarūnas Meškinis, Sigitas Tamulevičius. Low-Temperature Synthesis of Vertically Aligned Graphene Nanosheets on Glass Substrate. 22nd International Conference-School "Advanced materials and technologies 2020", Palanga, Lithuania, 24–28 September, 2020.
3. Erika Rajackaitė, Domantas Peckus, Rimantas Gudaitis, Mindaugas Andrulevičius, Tomas Tamulevičius, Šarūnas Meškinis, Sigitas Tamulevičius. Quality Studies of Vertical Graphene Nanosheets Using Transient Absorption Spectroscopy. 43rd National Physics Conference of Lithuania, Vilnius, Lithuania, 03–05 October, 2019.
4. Erika Rajackaitė, Domantas Peckus, Rimantas Gudaitis, Tomas Tamulevičius, Mindaugas Andrulevičius, Šarūnas Meškinis, Sigitas Tamulevičius. The Control of Quality of Graphene Layers Based on Their Ultrafast Relaxation Properties. 21st International Conference-School "Advanced materials and technologies 2019", Palanga, Lithuania, 19–23 August, 2019.
5. Erika Rajackaitė, Domantas Peckus, Rimas Gudaitis, Tomas Tamulevičius, Mindaugas Andrulevičius, Šarūnas Meškinis, Sigitas Tamulevičius. Excited state relaxation dynamics as a measure of quality of graphene layers deposited by plasma based techniques. European Materials Research Society (E-MRS) 2019 Spring Meeting Nice, France, 27–31 May, 2019.
6. Erika Rajackaitė, Domantas Peckus, Rimantas Gudaitis, Mindaugas Andrulevičius, Tomas Tamulevičius, Šarūnas Meškinis, Sigitas Tamulevičius. Transient absorption spectroscopy as a promising tool for defects characterization of graphene layers. 62nd international conference for students

of physics and natural sciences “Open readings 2019”, Vilnius, Lithuania, 19–22 March, 2019.

7. Erika Rajackaitė, Domantas Peckus, Asta Tamulevičienė, Tomas Tamulevičius, Rimantas Gudaitis, Šarūnas Meškinis, Sigitas Tamulevičius. Preparation method influence on morphology and ultrafast optical properties of graphene layers. 16th International conference “Apropos 16: Advanced properties and processes in optoelectronics materials and systems”, Vilnius, Lithuania, 10–12 October, 2018.
8. Erika Rajackaitė, Domantas Peckus, Asta Tamulevičienė, Tomas Tamulevičius, Rimas Gudaitis, Šarūnas Meškinis, Sigitas Tamulevičius. Dynamic optical properties of graphene layers with different preparation and morphology. 11th International conference on photo-excited processes and applications – ICPEPA 11, Vilnius, Lithuania, 10–14 September, 2018.
9. Erika Rajackaitė, Domantas Peckus, Rimas Gudaitis, Šarūnas Meškinis, Sigitas Tamulevičius. Synthesis and Analysis of Ultrafast Excited State Dynamics of Graphene Mono and Polylayers. 20th International Conference-School “Advanced materials and technologies 2018”, Palanga, Lithuania, 27–31 August, 2018.
10. Asta Tamulevičienė, Erika Rajackaitė, Domantas Peckus, Rimas Gudaitis, Tomas Tamulevičius, Sigitas Tamulevičius. Investigation of Graphene Influence on the Performance of Electrochromic Devices. European Materials Research Society (E-MRS) 2018 Spring Meeting, Strasbourg, France, 18–22 June, 2018.
11. Erika Rajackaitė, Domantas Peckus, Asta Tamulevičienė, Tomas Tamulevičius, Rimas Gudaitis, Šarūnas Meškinis, Sigitas Tamulevičius. Ultrafast Excited State Relaxation Dynamics of Mono and Multilayer Graphene. 61st International conference for students of physics and natural sciences “Open readings 2018”, Vilnius, Lithuania, 20–23 March, 2018.
12. Erika Rajackaitė, Rimantas Gudaitis, Sigitas Tamulevičius. Synthesis and investigation of the properties of graphene layers. 42nd National Physics Conference of Lithuania, Vilnius, Lithuania, 04–06 October, 2017.
13. Erika Rajackaitė, Rimantas Gudaitis, Sigitas Tamulevičius. Formation and Characterization of Graphene Films on Copper Substrates. 19th International Conference-School “Advanced materials and technologies 2017”, Palanga, Lithuania, 27–31 August, 2017.
14. Erika Rajackaitė, Rimantas Gudaitis, Sigitas Tamulevičius. Synthesis of Graphene by Microwave Plasma Enhanced Chemical Vapor Deposition. International Conference “Nanotechnology and Innovation in the Baltic Sea Region”, Kaunas, Lithuania, 14–16 June, 2017.
15. Erika Rajackaitė, Rimantas Gudaitis, Sigitas Tamulevičius. Characterization of Graphene Films Grown on Different Copper Substrates. Physics and Chemistry of Advanced Materials (PCAM) in collaboration with ITN Thinface Workshop in Kraków Poland: “Advanced topics in physics and materials engineering”, 18–19 May, 2017.

Conference contributions related to the dissertation (presented by the co-authors)

1. Domantas Peckus, Joel Henzie, Tomas Tamulevičius, Mindaugas Andrulevičius, Algirdas Lazauskas, Erika Rajackaitė, Šarūnas Meškinis, Sigitas Tamulevičius. Properties of Ultrafast Relaxation Dynamics of Plasmonic Aluminum Nanoparticles. 21st International Conference-School "Advanced materials and technologies 2019", Palanga, Lithuania, 19–23 August, 2019.
2. Valentinas Andrulis, Erika Rajackaitė, Tomas Matulaitis, Asta Dabulienė, Audrius Bučinskas, Dalius Gudeika, Asta Tamulevičienė. Investigation of bipolar small organic molecules as active material in electrochromic devices. 61st International conference for students of physics and natural sciences "Open readings 2018", Vilnius, Lithuania, 20–23 March, 2018.
3. Asta Tamulevičienė, Rimantas Gudaitis, Erika Rajackaitė, Šarūnas Meškinis, Sigitas Tamulevičius. Graphene monolayers for flexible electrochromic devices. 42nd National Physics Conference of Lithuania, Vilnius, Lithuania, 04–06 October, 2017.
4. Domantas Peckus, Sigitas Tamulevičius, Joel Henzie, Tomas Tamulevičius, Lukas Stankevičius, Mindaugas Juodėnas, Aušrinė Jurkevičiūtė, Erika Rajackaitė, Rimantas Gudaitis, Šarūnas Meškinis, Brigita Abrakevičienė, Hongpan Rong. Ultrafast dynamics of coherent oscillations of highly monodispersed plasmonic Ag nanocubes and their assemblies. European Materials Research Society (E-MRS) 2017 Spring Meeting, Strasbourg, France, 22–26 May, 2017.

Internships and summer schools abroad

1. 3-month International *Erasmus+* internship at the Mads Causen Institute of the University of Southern Denmark "Application of graphene layers in organic solar cells" under the PCAM program, Sønderborg, Denmark, 2nd September–5th December, 2019.
2. Physics and Chemistry of Advanced Materials (PCAM) in collaboration with ITN Thinface Workshop *Advanced topics in physics and materials engineering*, Kraków, Poland, 18–19 May, 2017.

SL344. 2022-06-17, 14,25 leidyb. apsk. l. Tiražas 14 egz. Užsakymas 109.
Išleido Kauno technologijos universitetas, K. Donelaičio g. 73, 44249 Kaunas
Spausdino leidyklos „Technologija“ spaustuvė, Studentų g. 54, 51424 Kaunas